

SACLANTCEN REPORT  
serial no: SM-342

SACLANT UNDERSEA RESEARCH CENTRE  
LIBRARY COPY # 3

**SACLANT UNDERSEA  
RESEARCH CENTRE  
REPORT**



**NUMERICAL SIMULATION OF THE EFFECTS  
OF BATHYMETRY ON UNDERWATER  
SOUND PROPAGATION USING  
THREE-DIMENSIONAL PARABOLIC MODELS**

*F.B. Sturm, J.A. Fawcett*

March 1998

The SACLANT Undersea Research Centre provides the Supreme Allied Commander Atlantic (SACLANT) with scientific and technical assistance under the terms of its NATO charter, which entered into force on 1 February 1963. Without prejudice to this main task – and under the policy direction of SACLANT – the Centre also renders scientific and technical assistance to the individual NATO nations.

---

This document is approved for public release.  
Distribution is unlimited

---

SACLANT Undersea Research Centre  
Viale San Bartolomeo 400  
19138 San Bartolomeo (SP), Italy

tel: +39-0187-540.111  
fax: +39-0187-524.600

e-mail: [library@saclantc.nato.int](mailto:library@saclantc.nato.int)

**NORTH ATLANTIC TREATY ORGANIZATION**

SACLANTCEN SM-342

**Numerical simulation of the effects of  
bathymetry on underwater sound  
propagation using three-dimensional  
parabolic models**

**Frédéric B. Sturm and John A. Fawcett**

The content of this document pertains to work performed under Project 042-4 of the SACLANTCEN Programme of Work. The document has been approved for release by The Director, SACLANTCEN.



Jan L. Spoelstra  
Director

intentionally blank page

SACLANTCEN SM-342

**Numerical simulation of the effects of bathymetry on underwater sound propagation using three-dimensional parabolic models**

Frédéric B. Sturm and John A. Fawcett

**Executive Summary:** In shallow water, range-dependent bathymetry can have a significant effect on the propagation of sound. In some cases, not only the range-dependence of the bathymetry but also the angular variation of the bathymetry affects the propagation of the acoustic energy. For example, acoustic energy will tend to refract as it propagates upslope. Thus for some surveillance or localization applications it is important to understand the full three-dimensional effects of propagation over a varying bathymetry.

In this report two different three-dimensional parabolic equation (PE) methods are presented. These methods are used to show the importance of three-dimensional effects for some examples and different frequencies and the results from the two methods are compared with each other in order to show that the two very different PE approaches give similar results.

The methods of this report provide an accurate and relatively efficient means of computing three-dimensional propagation loss. In the future it is hoped that the accuracy and efficiency of the methods can be even further improved.

intentionally blank page

SACLANTCEN SM-342

**Numerical simulation of the effects of bathymetry on underwater sound propagation using three-dimensional parabolic models**

Frédéric B. Sturm and John A. Fawcett

**Abstract:** Two different three-dimensional parabolic equation (PE) methods are presented. These methods are used to show the importance of three-dimensional effects for some examples and different frequencies and the results from the two methods are compared with each other in order to show that the two very different PE approaches give similar results.

The methods of this report provide an accurate and relatively efficient means of computing three-dimensional propagation loss which will form the basis of future improvements.

**Keywords:** Parabolic equation – propagation

## Contents

1. Introduction .....	1
2. Mathematical background.....	2
2.1. <i>Mathematical modelling based on the reduced wave equation</i> .....	2
2.2. <i>Paraxial approximation of the boundary value problem based on the Helmholtz equation</i> .....	3
2.3. <i>Other three-dimensional parabolic models including wide angle capabilities in depth</i> .....	6
2.4. <i>The TRIPARADIM model</i> .....	8
3. Numerical simulation of a three-dimensional wedge-shaped waveguide .....	9
3.1. <i>Description of the problem</i> .....	9
3.2. <i>Modal initialization</i> .....	11
3.3. <i>Non-attenuating halfspace bottom</i> .....	14
3.4. <i>Attenuating halfspace bottom</i> .....	24
4. Numerical simulations of a three-dimensional rough boundary waveguide.....	44
4.1. <i>Description of the problem</i> .....	44
4.2. <i>Numerical simulation</i> .....	45
5. Summary .....	56
References .....	57
Appendix A.....	58

# 1

## Introduction

---

Standard two-dimensional Parabolic Equation (PE) methods assume that the oceanic environment is azimuthally symmetric about the zero-range coordinate and then compute, by a marching algorithm, the acoustic wavefield in the range/depth plane. In order to model an environment where the sound speed and/or bathymetry changes with respect to azimuth, one can compute the wavefield along various azimuths, utilizing the two-dimensional PE with the environment appropriate for that azimuth. This type of modelling is called N X 2D modelling and makes the assumption that the coupling of energy from one azimuth to another can be disregarded. This approximation is often accurate; however, there are many examples of oceanic waveguides where the horizontal refraction of energy is significant in some areas and the N X 2D approximation does not model propagation correctly.

Three-dimensional PE codes have been developed in order to model the azimuthal coupling of energy, (e.g. [1] - [7]) and these have been used to compute propagation in a number of three-dimensional environments. However, there has been little comparison and benchmarking of these codes. In this report we will utilize two different three-dimensional PE codes [1], [3] which have different solution approaches. Using both methods, we will compute wavefields for some examples of three-dimensionally varying bathymetry. For some of these examples, the N X 2D solution will also be presented for comparison. In the numerical examples it will be seen that the two different three-dimensional PE methods yield similar wavefields thus giving confidence in these solutions (at least within the approximation of both methods). These examples could also serve as benchmark cases for other numerical codes and indicate when three-dimensional effects are important and when the N X 2D method should suffice.

## 2

## Mathematical background

*2.1 Mathematical modelling based on the reduced wave equation*

We consider a time-harmonic point source emitting at frequency  $f$  (the wavelength of the source is denoted  $\lambda$ ). Removing the time-varying component  $\exp(-i\omega t)$  where  $\omega$  is the circular frequency,  $\omega = 2\pi f$ , the space-varying pressure field  $P$  satisfies the three-dimensional reduced wave equation [8]

$$\rho \nabla \cdot (\rho^{-1} \vec{\nabla} P) + k_\alpha^2 P = -4\pi P_0 \delta(X - X_s) \quad (2.1)$$

written in cartesian coordinates  $X = (X_1, X_2, X_3)$ . The density  $\rho$  depends on the vector  $X$ . The position vector  $X_s = (0, 0, z_s)$  denotes the source location,  $4\pi P_0$  the source strength and  $k_\alpha$  the complex wavenumber, *i.e.*,  $k_\alpha = k + i\eta\alpha k$ , where  $k = \omega/c$ ,  $c = c(X)$  is the space-varying sound speed,  $\alpha = \alpha(X)$  is the attenuation expressed in decibels per wavelength, and  $\eta = 1/40\pi \log_{10} e$ , with  $\eta\alpha \ll 1$ .

We consider a multi-layered waveguide consisting of one water layer with density  $\rho_0$ , attenuation  $\alpha_0$ , sound speed  $c_0$ , and  $Q$  homogeneous fluid sediment layers with density  $\rho_q$ ,  $1 \leq q \leq Q$ , attenuation  $\alpha_q$ ,  $1 \leq q \leq Q$ , and sound speed  $c_q$ ,  $1 \leq q \leq Q$ . We denote by  $\Sigma_q$ ,  $1 \leq q \leq Q$ , the interface between medium  $q-1$  and medium  $q$ . The interface  $\Sigma_1$  corresponds to the sea-floor, *i.e.*, to the interface between the water column (medium 0) and the first sediment layer (medium 1). No cylindrical symmetry is assumed with respect to the waveguide geometry. Hence, the different interfaces  $\Sigma_q$ ,  $1 \leq q \leq Q$ , are allowed to have space-varying geometries.

The pressure  $P$  is assumed to satisfy a pressure-release boundary condition,  $P=0$ , at the ocean surface, denoted  $\Sigma_0$ , an outgoing radiation condition at infinity, and the perfectly rigid bottom condition

$$\vec{\nabla} P \cdot \vec{\eta} = 0 \quad (2.2)$$

at the lower boundary denoted  $\Sigma_{\max}$  where  $\vec{\eta}$  denotes a normal direction vector at  $\Sigma_{\max}$ . Because of the discontinuities of the density, attenuation and sound speed terms at  $\Sigma_q$ ,  $1 \leq q \leq Q$ , the pressure  $P$  is also assumed to satisfy the transmission conditions at  $\Sigma_q$ ,  $1 \leq q \leq Q$ , *i.e.*, continuity of the pressure  $P_{q-1} = P_q$  and continuity of the normal component of the particle velocity (normal derivative condition)

$$\frac{1}{\rho_{q-1}} \vec{\nabla} P_{q-1} \cdot \vec{\eta}_q = \frac{1}{\rho_q} \vec{\nabla} P_q \cdot \vec{\eta}_q \quad (2.3)$$

SACLANTCEN SM-342

where  $\bar{\eta}_q$  denotes a normal direction vector at  $\Sigma_q$ ,  $1 \leq q \leq Q$ .

## 2.2 Paraxial approximation of the boundary value problem based on the Helmholtz equation

### Description of the waveguide geometry in cylindrical coordinates

We now work in cylindrical coordinates, with  $z$  being the depth below the horizontal ocean surface,  $\theta$  being the azimuth angle and  $r$  being the horizontal range, related to the cartesian coordinates by :  $X_1 = r \cos \theta$ ,  $X_2 = r \sin \theta$ ,  $X_3 = z$ . We denote by  $z_{\max}(r, \theta)$  and by  $z_q(r, \theta)$ ,  $1 \leq q \leq Q$ , the parametrization of, respectively, the rigid bottom  $\Sigma_{\max}$  and the sediment interfaces  $\Sigma_q$ ,  $1 \leq q \leq Q$ . The horizontal range  $r$  varies from  $r_0$  to  $R$ , the azimuth angle  $\theta$  from 0 to  $2\pi$  and the depth  $z$  from 0 to  $z_{\max}(r, \theta)$  (cf. Fig. 2.1). We assume for  $r_0 \leq r \leq R$ ,  $0 \leq \theta < 2\pi$ , that we have  $0 < z_1(r, \theta) < \dots < z_Q(r, \theta) < z_{\max}(r, \theta)$ .

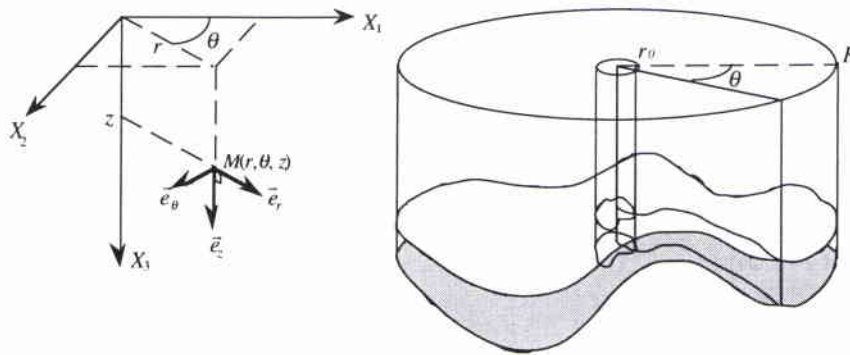


**Figure 2.1** three-dimensional irregular geometry of the physical waveguide for  $r_0 \leq r \leq R$ ,  $0 \leq \theta < 2\pi$ ,  $0 \leq z \leq z_{\max}(r, \theta)$ . Only two layers are represented : the water column which corresponds to  $0 \leq z \leq z_1(r, \theta)$  and one layer of fluid sediment which corresponds to  $z_1(r, \theta) \leq z \leq z_{\max}(r, \theta)$ . The sediment interface (sea-floor) of parametrization  $z = z_1(r, \theta)$  is shown in light grey and the rigid bottom of parametrization  $z = z_{\max}(r, \theta)$  is shown in dark grey.

### Derivation of a linear parabolic equation which includes density variations

For the derivation of parabolic equations (PE), we introduce a reference sound speed  $c_{ref}$  and a reference real-valued wave number  $k_{ref} = \omega/c_{ref}$ . As we are mainly interested in the outgoing component of the propagating wavefield, we factor the pressure  $P$  as

$$P(r, \theta, z) = H_0^{(1)}(k_{ref} r) v(r, \theta, z)$$

where  $H_0^{(1)}$  denotes the zero-order Hankel function of the first kind. This factorization takes into account the natural cylindrical spreading of the pressure field. Assuming

weak dependence of the medium characteristics with respect to the range and assuming that the backscattering energy may be disregarded, Eq. (2.1), rewritten in cylindrical coordinates, can be factored and then leads far from the source (*i.e.*,  $k_{ref}r \gg 1$ ) to the following expression for the outgoing solution

$$\frac{\partial v}{\partial r} = ik_{ref} \left( \sqrt{\mathbf{I} + \mathbf{X}_\rho + \mathbf{Y}_\rho} - \mathbf{I} \right) v \quad (2.4)$$

where operators  $\mathbf{X}_\rho$  and  $\mathbf{Y}_\rho$  are defined by ( $\mathbf{I}$  denotes the identity)

$$\mathbf{X}_\rho = (n_\alpha^2(r, \theta, z) - 1)\mathbf{I} + \frac{\rho}{k_{ref}^2} \frac{\partial}{\partial z} \left( \frac{1}{\rho} \frac{\partial}{\partial z} \right) \quad (2.5)$$

$$\mathbf{Y}_\rho = \frac{\rho}{k_{ref}^2 r^2} \frac{\partial}{\partial \theta} \left( \frac{1}{\rho} \frac{\partial}{\partial \theta} \right) \quad (2.6)$$

The operator  $\mathbf{X}_\rho$  takes into account, from left to right in Eq. (2.6), the refraction term (including attenuation) and the vertical diffraction term (including the depth-dependence of the density). The operator  $\mathbf{Y}_\rho$  defined by Eq. (2.6) handles the azimuthal crossing diffraction term (including the azimuthal-dependence of the density). Using Taylor series expansion, we write

$$\sqrt{\mathbf{I} + \mathbf{X}_\rho + \mathbf{Y}_\rho} = \mathbf{I} + \frac{1}{2}(\mathbf{X}_\rho + \mathbf{Y}_\rho) + O(\mathbf{X}_\rho^2, \mathbf{X}_\rho \mathbf{Y}_\rho, \mathbf{Y}_\rho^2) \quad (2.7)$$

Inserting Eq. (2.7) in Eq. (2.4) and under the assumption of a slow varying medium and of narrow angles of propagation with respect to the horizontal, we can neglect the term  $O(\mathbf{X}_\rho^2, \mathbf{X}_\rho \mathbf{Y}_\rho, \mathbf{Y}_\rho^2)$ , leading to the following parabolic equation

$$\frac{\partial v}{\partial r} = \frac{ik_{ref}}{2} (n_\alpha^2(r, \theta, z) - 1)v + \frac{i\rho}{2k_{ref}} \left( \frac{\partial}{\partial z} \left( \frac{1}{\rho} \frac{\partial v}{\partial z} \right) + \frac{1}{r^2} \frac{\partial}{\partial \theta} \left( \frac{1}{\rho} \frac{\partial v}{\partial \theta} \right) \right) \quad (2.8)$$

which reduces, assuming no variation of the density to

$$\frac{\partial v}{\partial r} = \frac{ik_{ref}}{2} (n_\alpha^2(r, \theta, z) - 1)v + \frac{i}{2k_{ref}} \left( \frac{\partial^2 v}{\partial z^2} + \frac{1}{r^2} \frac{\partial^2 v}{\partial \theta^2} \right).$$

The three-dimensional PE given by Eq. (2.8) has narrow angle capabilities both in depth and azimuth, *i.e.*, it can handle properly waves propagating within an angle with respect to the horizontal less than  $\pm 15-20^\circ$ , leading to increasing phase errors for wider angles. The three-dimensional code TRIPARADIM written by Sturm [1] is based on Eq. (2.8).

SACLANTCEN SM-342

**Parabolized boundary conditions consistent with the linear paraxial approximation**

The envelope  $v$  is assumed to satisfy  $v=0$  at  $\Sigma_0$ , a  $2\pi$ -periodicity condition in azimuth  $v(r,0,z)=v(r,2\pi,z)$ , an initial condition  $v(r_0,\theta,z)=v^0(\theta,z)$  at  $r=r_0$  a parabolized bottom condition

$$\left(\frac{\partial v}{\partial z} - ik_{ref} \frac{\partial z_{max}}{\partial r} v - \frac{1}{r^2} \frac{\partial z_{max}}{\partial \theta} \frac{\partial v}{\partial \theta}\right)(r, \theta, z_{max}) = 0 \quad (2.9)$$

at  $\Sigma_{max}$ , consistent transmission conditions at  $\Sigma_q$ ,  $1 \leq q \leq Q$ , *i.e.*, continuity condition

$$v_{q-1}(r, \theta, z_q) = v_q(r, \theta, z_q) \quad (2.10a)$$

and a parabolized condition

$$\frac{1}{\rho_{q-1}} \frac{\partial v_{q-1}}{\partial T_q}(r, \theta, z_q) = \frac{1}{\rho_q} \frac{\partial v_q}{\partial T_q}(r, \theta, z_q), \quad (2.10b)$$

where the parabolized normal derivative operators  $\partial/\partial T_q$ ,  $1 \leq q \leq Q$ , are defined by

$$\frac{\partial}{\partial T_q} = \frac{\partial}{\partial z} - ik_{ref} \frac{\partial z_q}{\partial r} \mathbf{I} - \frac{1}{r^2} \frac{\partial z_q}{\partial \theta} \frac{\partial}{\partial \theta}.$$

Equation (2.9) is a three-dimensional generalization of the bi-dimensional parabolized bottom condition proposed by Abrahamsson and Kreiss [10]. The parabolized conditions given by Eqs. (2.9) and (2.10) are derived considering, on the range-component of the normal derivative present in Eqs. (2.2) and (2.3), the following horizontal plane wave impedance condition

$$\frac{\partial P}{\partial r} = ik_{ref} P \quad (2.11)$$

which has been implicitly used as an underlying approximation in the derivation of Eq. (2.8), *i.e.*, in the linear parabolic approximation of the Helmholtz equation [11] and leads to the stability condition

$$\frac{d}{dr} \int_0^{2\pi} \int_0^{z_{max}(r,\theta)} |v(r, \theta, z)|^2 \frac{d\theta dz}{\rho} \leq 0. \quad (2.12)$$

Eq. (2.12) can be established by multiplying Eq. (2.8) by  $\bar{v}/\rho$  where  $\bar{v}$  denotes the complex conjugate of  $v$ , integrating by parts using Eqs. (2.9) and (2.10) and taking the real part. The stability condition of Eq. (2.12) ensures existence and uniqueness of a solution to the parabolized model. It generalizes to a three-dimensional range-and-azimuth dependent waveguide, the stability condition derived by Dougalis and Kampanis [13] for a 2D range-independent waveguide. Using the physical conditions, *i.e.*, Eqs. (2.2) and (2.3), which are mathematically correct conditions for the reduced wave equation based model, would lead to an ill-posed boundary value problem.

Equation (2.12) holds as an equality if the attenuation term  $\alpha=0$ . The parabolized model is hence energy-conserving. The TRIPARADIM code includes these parabolized three-dimensional conditions.

### 2.3 Other three-dimensional parabolic models including wide angle capabilities in depth

One elegant way to approximate the square-root operator present in Eq. (2.4) (which is obviously numerically hard to solve directly) and to obtain three-dimensional PE with wider angle capabilities is to use Padé series in depth [12], [13], which, assuming  $|Y_\rho P| \ll |X_\rho P|$ , can be written as

$$\sqrt{I + X_\rho + Y_\rho} = I + \sum_{j=1}^{n_p} \left( \frac{a_{j,n_p} X_\rho}{I + b_{j,n_p} X_\rho} \right) + \frac{1}{2} Y_\rho + O(X_\rho^{2n_p+1}, X_\rho Y_\rho, Y_\rho^2) \quad (2.13)$$

with the Padé coefficients given for  $1 \leq j \leq n_p$  by

$$a_{j,n_p} = (2/(2n_p + 1)) \sin^2(j\pi/(2n_p + 1)) \quad \text{and} \quad b_{j,n_p} = \cos^2(j\pi/(2n_p + 1))$$

where  $n_p$  is the number of terms in the expansion. This expansion allows effectively for wide angle propagation in depth, the angular limitation depending on the number of Padé terms included in the truncated series, but for narrow angle in azimuth. Considering only one term from the sum in Eq. (2.13) and including the resulting quadratic approximation, (i.e., the term  $O(X_\rho^3, X_\rho Y_\rho, Y_\rho^2)$  is disregarded) in Eq. (2.4) gives

$$\frac{\partial v}{\partial r} = ik_{ref} \left( \frac{X_\rho/2}{I + X_\rho/4} + \frac{1}{2} Y_\rho \right) v \quad (2.14)$$

which corresponds to a Claerbout wide angle PE in depth (limitation angle  $\pm 35-40^\circ$ ) [14] and a Tappert narrow angle PE in azimuth (limitation angle  $\pm 15-20^\circ$ ). Several three-dimensional parabolic models are based on the expansion used in Eq. (2.13), e.g., [3], [5].

For all these three-dimensional PE based methods, the bottom slopes (both in range and azimuth) are handled using stair-step approximations. The bottom geometry  $\Sigma_{\max}$  and the different sediment interfaces  $\Sigma_q$ ,  $1 \leq q \leq Q$ , are hence assumed to be locally horizontal. In the two models developed by Collins and Chin-Bing [5] and Fawcett [3], the density term is assumed to depend only on  $z$ . The second transmission condition given by Eq. (2.3) on  $\Sigma_q$ ,  $1 \leq q \leq Q$ , is accordingly replaced by the horizontal condition

$$\frac{1}{\rho_{q-1}} \frac{\partial v_{q-1}}{\partial z}(r, \theta, z_q) = \frac{1}{\rho_q} \frac{\partial v_q}{\partial z}(r, \theta, z_q) \quad (2.15)$$

SACLANTCEN SM-342

When attempting to take sloping bottoms into account without assuming any stair-step approximation, one should use appropriate parabolized bottom and interface conditions consistent with the wide angle (in depth) parabolic equation (see reference [16] for more details in the bidimensional case).

The models [3], [5] consider a pressure-release boundary condition at the horizontal bottom  $\Sigma_{\max}$  and use artificial attenuation in the medium to negate the effects of this boundary. Equation (2.14) can now be solved using a splitting method, which requires numerical solutions for each of the following equations

$$\left(1 + \frac{(n_\alpha^2 - 1)}{4} + \frac{\rho}{4k_{ref}^2} \frac{\partial}{\partial z} \left( \frac{1}{\rho} \frac{\partial}{\partial z} \right)\right) \frac{\partial v}{\partial r} = \frac{ik_{ref}}{2} (n_\alpha^2 - 1)v + \frac{i\rho}{2k_{ref}} \frac{\partial}{\partial z} \left( \frac{1}{\rho} \frac{\partial v}{\partial z} \right) \quad (2.16a)$$

$$\frac{\partial v}{\partial r} = \frac{i}{2k_{ref}r^2} \frac{\partial^2 v}{\partial \theta^2} \quad (2.16b)$$

We focus on the three-dimensional model FAWPE developed by Fawcett in which Eq. (2.16a) is solved using a finite difference discretization technique (in depth) and a Crank-Nicolson range stepping procedure. Using central finite differences to approximate second order partial derivatives present in Eq. (2.16a) and considering  $N$  discrete points in depth and  $M$  discrete points in the azimuthal direction, leads to  $M$  tri-diagonal linear systems of order  $N$  at each step in range, that can be solved using a fast and robust Gaussian elimination method. Equation (2.16b) is solved using an FFT technique, *i.e.*, by computing

$$v(r + \Delta r, \theta, z) = F_\theta^{-1} \left( \exp \left( -\frac{im^2 \Delta r}{2k_{ref}r(r + \Delta r)} \right) F_\theta(v(r, \theta, z)) \right)$$

where  $\Delta r$  denotes the range increment,  $F_\theta$  denotes the Fourier transform with respect to  $\theta$  ( $m$  denotes the azimuthal wave number), and  $F_\theta^{-1}$  is its inverse transform. In sections 3 and 4, we will present numerical simulations using the two three-dimensional codes FAWPE and TRIPARADIM. In order to make some comparisons, we replace Eq. (2.16a) by

$$\frac{\partial v}{\partial r} = \frac{ik_{ref}}{2} (n_\alpha^2(r, \theta, z) - 1)v + \frac{i\rho}{2k_{ref}} \frac{\partial}{\partial z} \left( \frac{1}{\rho} \frac{\partial v}{\partial z} \right)$$

in order to make FAWPE narrow angle in depth (as in TRIPARADIM). The only difference in the two models is the way of treating the interfaces (which are locally horizontal in FAWPE due to the stair-step approximation) and the rigid bottom. We outline in the following section how TRIPARADIM adapts its discretization to the space-varying geometry of the waveguide and hence, accurately models three-dimensional sloping bottoms.

#### 2.4. *The TRIPARADIM model*

As discussed above, three-dimensional PE models typically approximate the interface as locally horizontal stair steps. In fact, in some codes such as FAWPE the interface conditions are not imposed explicitly but are only implicitly handled with the change of sound speed and density in the finite difference discretization.

The code TRIPARADIM treats the interface scattering very accurately. First the depth coordinate is transformed so that the water/sediment interface becomes flat (any additional sediment interfaces are assumed to have the same functional form as this interface and hence are also mapped into flat interfaces). This coordinate transformation introduces new terms into the Helmholtz equation. The interface conditions Eq. (2.10a) are incorporated into a Finite Element discretization.

It is not possible to split the resulting operator into a depth and azimuthal operator as in other approaches. Instead, a large system of equations in depth and azimuth results. This system is sparse, and by preconditioning, it is possible to solve the system of equations in an efficient manner. The mathematical and numerical details of this code are presented in Annex A.

In our numerical computations we compare the results obtained by a three-dimensional PE code [3] which uses a standard splitting approach and by TRIPARADIM which takes quite a different approach to the problem and handles the interface boundary conditions very accurately.

## Numerical simulation of a three-dimensional wedge-shaped waveguide

---

### 3.1 Description of the problem

#### Description of the three-dimensional varying waveguide

We consider the penetrable wedge-shaped problem originally proposed as an ASA benchmark in 1987 and extensively used to analyze accuracy and efficiency of various two dimensional ocean acoustics models [15] and later extended to a three-dimensional benchmark case by Fawcett in 1993 [3]. It consists of an isovelocity water layer of density  $\rho_0 = 1 \text{ g/cm}^3$  and sound speed  $c_0 = 1500 \text{ m/s}$ , overlying a homogeneous halfspace sediment layer of density  $\rho_1 = 1.5 \text{ g/cm}^3$  and sound speed  $c_1 = 1700 \text{ m/s}$ , which leads to a critical grazing angle  $\vartheta_c = \arccos(c_0/c_1)$  approximately equal to  $28^\circ$ . No shear energy is assumed in the sediment layer. The discontinuity present at the interface  $\Sigma_1$  between the water column and the fluid sediment layer is given in cylindrical coordinates by the following three-dimensional surface parametrization

$$z_1(r, \theta) = H \left( 1 - \frac{r \cos \theta}{4000} \right) \quad (3.1)$$

where  $H = 200 \text{ m}$ . Equation (3.1) gives rise to a non-horizontal plane geometry interface. A CW point source of frequency  $f$  is placed at cartesian position vector  $X_s = (0, 0, z_s)$  which corresponds in cylindrical coordinates to range  $r=0$  and depth  $z = z_s$  (we recall that  $X_1 = r \cos \theta$ ,  $X_2 = r \sin \theta$ ,  $X_3 = z$ ). Upslope and downslope propagations are handled, respectively, for  $\theta$  varying from  $-90^\circ$  to  $90^\circ$  and for  $\theta$  varying from  $90^\circ$  to  $270^\circ$  (cf. Fig. 3.1) with a maximum slope of  $2.86^\circ$  in the geometry corresponding to  $\theta=0^\circ$  (upslope) and  $\theta=180^\circ$  (downslope) and no slope for  $\theta=90^\circ$  and  $\theta=270^\circ$ .

Let us denote by  $\eta = (\eta_r, \eta_\theta, \eta_z)^T$  a normal direction vector to the interface  $\Sigma_1$  defined by Eq. (3.1). The basic point of  $N \times 2D$  modelling is that for each azimuth, cylindrical symmetry of the problem is assumed and hence no bathymetry variation in the crossing (azimuthal) direction is taken into account, thus the azimuthal component  $\eta_\theta$  is forced to be zero. This is untrue for the specific three-dimensional wedge-shaped waveguide we presently consider for which the azimuthal component  $\eta_\theta \propto \sin \theta$  and hence presents a strong azimuthal dependence. We focus on the particular azimuthal angle  $\theta=90^\circ$  for which the component  $\eta_\theta$  reaches its maximum and for which we expect larger three-dimensional effects. Note that for  $\theta=90^\circ$  or for  $\theta=180^\circ$  the  $N \times 2D$  cylindrical symmetry assumption is locally valid and hence we expect no horizontal refraction of propagating sound for these angles.



layers. The first sediment layer assumes attenuation or no attenuation depending of the problem we are interested in, whereas the second one, referred to as an artificial absorbing layer, assumes an increasing attenuation until  $z = z_{\max}$ .

The way of handling these two sediment layers differs between TRIPARADIM and FAWPE (cf. Fig. 3.3). Due to the use of mapping which maps the physical waveguide unto a cylinder-like mapped computation domain in the TRIPARADIM three-dimensional modelling, the various sediment interfaces are required to have the multiple functional form (homothetical) that they all map into flat interfaces in the mapped computation domain. The parametrizations of the interface  $\Sigma_2$  and of the rigid bottom  $\Sigma_{\max}$  are now assumed to be non-constant in range and azimuth, i.e.,  $z = z_2(r, \theta)$  and  $z = z_{\max}(r, \theta)$ . This assumption is not required by the FAWPE code, the interface  $\Sigma_2$  and the pressure-released bottom  $\Sigma_{\max}$  being both horizontal.

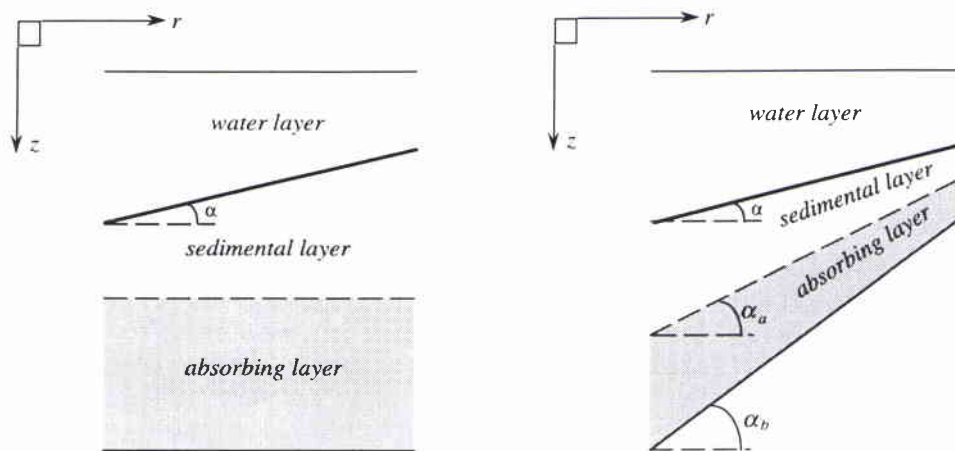


**Figure 3.3** Two-dimensional sediment and artificial absorbing layers geometries of the wedge-shaped waveguide corresponding to  $\theta=0^\circ$  (vertical slice): different ways of describing the halfspace bottom. On the left side, the artificial interface (dashed line) and the perfect reflective lower boundary are assumed to be horizontal in the FAWPE model. On the right side, these two interfaces are assumed to be homothetical in the TRIPARADIM model. Note that for both models, the water/bottom interface (bold line) is exactly the same.

All the TL vs. range curves presented in this section correspond to the fixed azimuth angle  $\theta=90^\circ$  and to the fixed receiver depth  $z=36$  m. All the vertical and horizontal TL contour plots will also correspond, respectively, to  $\theta=90^\circ$  and  $z=36$  m. Note that in the various horizontal slices, a section has been covered in order to hide the part of the TL field which is inside the sediment layer.

### 3.2 Modal initialization

A point source emitting at different low frequencies (5 Hz, 15 Hz, 25 Hz) will be considered. In order to understand modal dependence of horizontal refraction of

energy in the three-dimensional wedge-shaped bathymetry, we will expand the initial field in a modal sum for each frequency. We now turn to the derivation of a modal source. We consider the Pekeris-like waveguide shown in Fig. 3.4, consisting of an isovelocity water layer of density  $\rho_0$  and sound speed  $c_0$ , over an isovelocity halfspace sediment layer of density  $\rho_1$  and sound speed  $c_1$ . The sediment interface depth  $H$  is constant. The attenuation term is assumed to be zero in the two (fluid) layers.

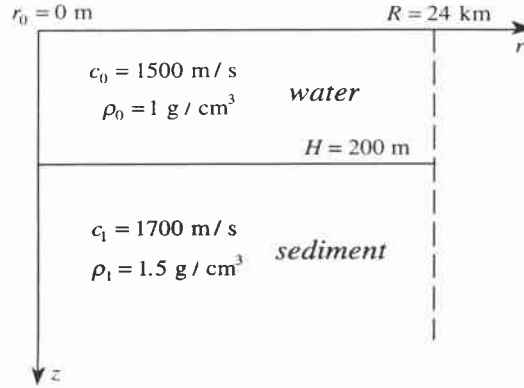


**Figure 3.4** Two-dimensional Pekeris-like waveguide geometry corresponding to the particular azimuthal angle  $\theta=90^\circ$  of the three-dimensional wedge-shaped waveguide shown in Fig. 3.1

A mode-shaped function  $\psi(z)$  is defined as the solution of the eigenvalue problem involving the following modal equation

$$\psi_q''(z) + (\omega^2/c_q^2 - k_r^2) \psi_q(z) = 0 \quad 0 \leq q \leq 1 \quad (3.2)$$

where  $\omega = 2\pi f$  denotes the circular frequency of the source, where  $k_r^2$  denotes a specified eigenvalue of the problem and where the eigenfunction  $\psi(z)$  is denoted  $\psi(z) = \psi_0(z)$  for  $0 \leq z \leq H$  and  $\psi(z) = \psi_1(z)$  for  $z > H$ , and is assumed to satisfy a Dirichlet condition at  $z=0$ , i.e.,  $\psi_0(0)=0$ , a vanishing condition at  $z \rightarrow +\infty$ , the interface conditions at  $z=H$ , i.e.,  $\psi_0(H) = \psi_1(H)$  and  $\psi_0'(H)/\rho_0 = \psi_1'(H)/\rho_1$ . We are mainly interested in long range propagation. Therefore, we neglect the continuous spectrum of the previous eigenvalue problem and focus only on the *discrete* propagating modes which can be written in the following analytical form

$$\hat{\psi}_m(z) = \begin{cases} \sin(k_{z,m} z) & \text{for } 0 \leq z \leq H \\ \sin(k_{z,m} H) \exp(-\gamma_m(z-H)) & \text{for } z > H \end{cases} \quad (3.3)$$

where  $k_{z,m}$  designates the vertical wavenumber defined by  $k_{z,m} = (\omega^2/c_0^2 - k_{r,m}^2)^{1/2}$  and  $k_{r,m}$  designates the horizontal wavenumber satisfying  $\omega/c_1 < k_{r,m} < \omega/c_0$  and is a solution of the characteristic equation.

$$\tan\left(\sqrt{\omega^2/c_0^2 - k_{r,m}^2} H\right) = -\frac{\rho_1 \sqrt{\omega^2/c_0^2 - k_{r,m}^2}}{\rho_0 \sqrt{k_{r,m}^2 - \omega^2/c_1^2}} \quad (3.4)$$

The positive number  $\gamma_m$  is defined by  $\gamma_m = (k_{r,m}^2 - \omega^2/c_1^2)^{1/2}$ . We introduce the modal phase velocity  $c_{r,m}$  defined by  $c_{r,m} = \omega/k_{r,m}$  which satisfies  $c_0 < c_{r,m} < c_1$ . To each mode  $\hat{\psi}_m(z)$  defined by Eq. (3.3) corresponds an up and downgoing plane wave with a vertical angle of propagation  $\vartheta_m = \arctan(k_{z,m}/k_{r,m})$  less than the critical angle  $\vartheta_c$ . We denote by  $m_p(f)$  the frequency-dependent number of propagating modes. We present in Table 1 the horizontal wavenumber  $k_{r,m}$ , the vertical wavenumber  $k_{z,m}$ , the phase velocity  $c_{r,m}$  and the grazing angle  $\vartheta_m$  corresponding to each propagating mode  $m$ ,  $1 \leq m \leq m_p$  for the different frequencies. These values have been obtained using the SACLANTCEN SNAP numerical code [18]. They correspond to the specific values  $\rho_0 = 1 \text{ g/cm}^3$ ,  $c_0 = 1500 \text{ m/s}$ ,  $\rho_1 = 1.5 \text{ g/cm}^3$ ,  $c_1 = 1700 \text{ m/s}$ , and  $H = 200 \text{ m}$  used in the above subsection. We are also interested in generating a point-source-like starting field, which can be processed by using modal expansion. Because only long-range propagation is considered, we limit the modal sum to include just the discrete modal spectrum, which means we limit the angular spectrum at the source to a halfwidth of  $\vartheta_c = \arccos(c_0/c_1)$ . The normalized starting field at  $r = 0$  takes simply the form

$$\psi(z) = \frac{\sqrt{2\pi}}{\rho_0} \sum_{m=1}^{m_p} \frac{\Psi_m(z_s) \Psi_m(z)}{\sqrt{k_{r,m}}} \quad (3.5)$$

where the normalized modes  $\psi_m(z)$ ,  $1 \leq m \leq m_p(f)$ , write  $\psi_m(z) = \eta_m \hat{\psi}_m(z)$ , where  $\hat{\psi}_m(z)$ ,  $1 \leq m \leq m_p(f)$ , are given by Eq. (3.3). The normalization constants  $\eta_m$  given by

$$\eta_m = \left( \frac{1}{\rho_0} \left( \frac{H}{2} - \frac{\sin(2k_{z,m}z)}{4k_{z,m}} \right) + \frac{\sin^2(k_{z,m}z)}{2\rho_1\gamma_m} \right)^{-\frac{1}{2}} \quad (3.6)$$

are introduced so as to have, for  $1 \leq m \leq m_p(f)$ , the following normalization condition

$$\int_0^{+\infty} \frac{\Psi_m^2(z)}{\rho} dz = 1.$$

**Table 1** Modal information for frequencies used in wedge example

5 Hz				
mode $m$	$k_{r,m}$ (rad/m)	$k_{z,m}$ (rad/m)	$c_{r,m}$ (m/s)	$\vartheta_m$ (deg)
1	0.0188375	0.0091540	1667.73	25.91
15 Hz				
mode $m$	$k_{r,m}$ (rad/m)	$k_{z,m}$ (rad/m)	$c_{r,m}$ (m/s)	$\vartheta_m$ (deg)
1	0.0615501	0.0126263	1531.24	11.59
2	0.0574504	0.0254419	1640.51	23.88
25 Hz				
mode $m$	$k_{r,m}$ (rad/m)	$k_{z,m}$ (rad/m)	$c_{r,m}$ (m/s)	$\vartheta_m$ (deg)
1	0.1038243	0.0136652	1512.94	7.498
2	0.1010523	0.0274711	1554.44	15.20
3	0.0962252	0.0413150	1632.42	23.23

### 3.3 Non-attenuating halfspace bottom

We now consider the wedge-shaped waveguide of Subsection 3.1 including the same geoacoustics characteristics and the parametrization given by Eq. (3.1) of the interface  $\Sigma_1$  between the water and the bottom, *i.e.*,  $z = z_1(r, \theta)$ . We assume *no attenuation* in both the water column and the halfspace bottom. We investigate separately the propagation of each discrete mode present in the point source emission (frequency 25 Hz,  $m_p(25) = 3$ ) located at range  $r = 0$ , the water/bottom interface depth being  $H = 200$  m at this range. We initialize each azimuth by the same unnormalized mode. The source-field is thus omnidirectional.

#### Expected 3D and $N \times 2D$ propagating fields

The bathymetry of the waveguide at the azimuthal angle  $\theta = 90^\circ$  (as well as at  $\theta = 270^\circ$  due to the symmetry in the geometry about the  $X_1$  axis) corresponds to the Pekeris-like waveguide presented in Subsection 3.2. Assuming local cylindrical symmetry of the problem, the energy propagating in the  $\theta = 90^\circ$  direction is trapped in the water column without any loss other than the natural cylindrical spreading (*i.e.*, no energy is radiated in the bottom). We thus expect to have TL vs. range behavior  $\propto 10 \log_{10} r$  for arbitrary receiver depth and for  $\theta = 90^\circ$ .

For azimuth angles different from  $\theta=90^\circ$  and  $\theta=270^\circ$ , mode conversion and cutoff phenomena will appear during upslope propagation, *i.e.*, steepening of the ray-mode angle leading to supercritical incidence and hence radiating energy in the bottom at a certain range referred as *mode-cutoff range*. These effects have been previously analyzed [17]. Mode conversion will also appear during the downslope propagation.

Using a full 3D model, the acoustic propagation problem corresponding to a specific azimuth can not be processed separately from other azimuthal angles. Though the bathymetry at  $\theta=90^\circ$  (or  $\theta=270^\circ$ ) is identical to the Pekeris-like one, the three-dimensional propagation field is expected to be different to the one obtained using a  $N \times 2D$  model, due both to the non-neglectable azimuthal component in the interface condition (as discussed in subsection 3.1) and to the azimuthal coupling term present in the three-dimensional parabolic equation. Due to the increasing grazing angle  $\vartheta_m$  with respect to the mode number  $m$ , we expect to have the strongest three-dimensional effects for higher order modes.

### Numerical simulations

We compute the three-dimensional fields corresponding to the propagation of each mode  $m$ ,  $1 \leq m \leq 3$  for range varying from 0 to  $R=24$  km, using the full three-dimensional model TRIPARADIM. In order to decrease the phase error inherent to parabolic models, we use the modal phase velocity for the reference sound speed.

The homothetical artificial interface (*i.e.* the start of the artificial attenuation) and perfectly rigid bottom are placed, respectively, at  $z_1 = 780$  m and  $z_{\max} = 1040$  m at  $r=0$ , leading to an absorbing layer width of 260 m at this range. Due to memory storage limitations, the TRIPARADIM code can not handle for this case wider absorbing layers.

We show in Figs. 3.5, 3.6, 3.7 (lower plots) color-scaled TL plots (horizontal slices at constant depth  $z = 36$  m) corresponding, respectively, to mode 1, mode 2 and mode 3. We also display in Figs. 3.5, 3.6, 3.7 (upper plots) the corresponding TL horizontal slice plots reconstructed using  $N \times 2D$  computation.

We can clearly observe, by comparing the  $N \times 2D$  and three-dimensional plots, the effects of the 3D varying bathymetry on the different modal propagations. The horizontal refraction of the energy is accurately handled by the three-dimensional computation and is in good qualitative agreement with the prediction of the adiabatic modal ray theory [3]. The energy is refracted back down the slope. As discussed above, computation using a  $N \times 2D$  model can not predict such effects: a modal-ray traveling in the vertical plane  $\theta=90^\circ$  is conserved during all the propagation, assuming only  $TL \propto 10 \log_{10} r$  due to natural cylindrical spreading. Three-dimensional computations still contain this natural decay in the energy but also contain effects that can not be predicted by  $N \times 2D$  computations.

The horizontal refraction effect is more pronounced for higher modes than for lower modes. This modal horizontal refraction dependence is due to the steeper grazing angles corresponding to the higher modes, leading to a shadow zone region starting at approximately 11 km in the  $X_2$  axis ( $\theta=90^\circ$ ), for mode 3 ( $\vartheta_3 \approx 23.23^\circ$ ) and at 18 km for mode 2 ( $\vartheta_2 \approx 15.20^\circ$ ) for the same vertical plane. We refer to this first particular three-dimensional effect as *three-dimensional mode shadowing*.

For mode 1 ( $\vartheta_1 \approx 7.49^\circ$ ) the horizontal refraction of the energy is more gradual. No shadow zone is observed for ranges less than the maximum range  $R = 24$  km for  $\theta = 90^\circ$ . We notice however that the horizontal refraction effect is present for adjacent azimuthal angles (though weaker than for mode 2 or mode 3).

We observe also in the lower plot of Fig. 3.5 at azimuth angles adjacent to  $\theta = 90^\circ$  a fringe pattern corresponding to interference effects between the different arrivals of the same initial mode. We refer to this second particular three-dimensional effect as *three-dimensional mode self-interference*. This last three-dimensional effect is also present for the other two modes (mode 2 and mode 3) as it can be seen in the lower plots of Figs. 3.6 and 3.7 near the thin caustic present at the front of the modal energy.

SACLANTCEN SM-342

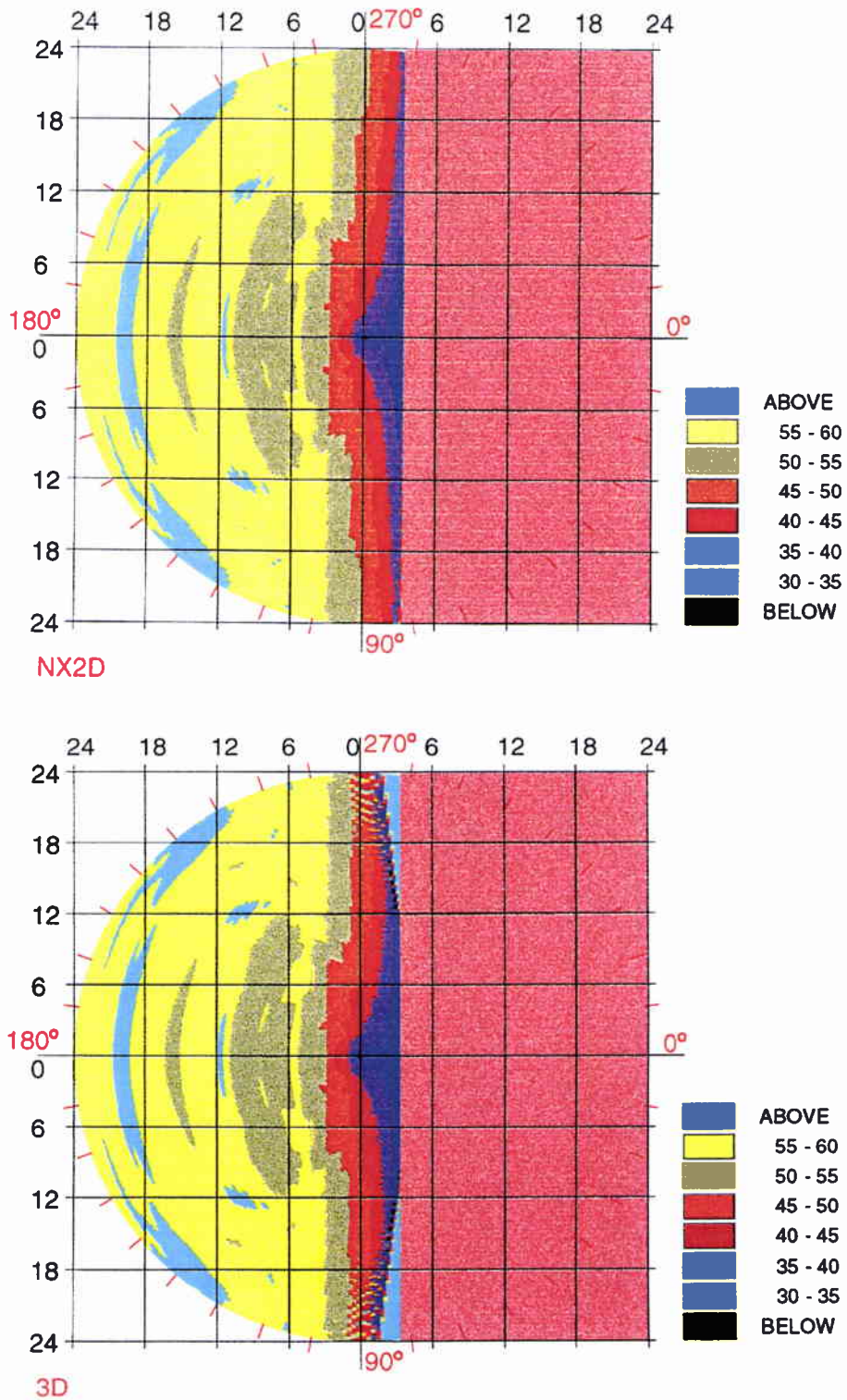


**Figure 3.5** Mode 1 - frequency 25 Hz, horizontal slices at constant depth  $z = 36$  m of the TL fields obtained using  $N \times 2D$  (upper figure) / three-dimensional (bottom figure) computations

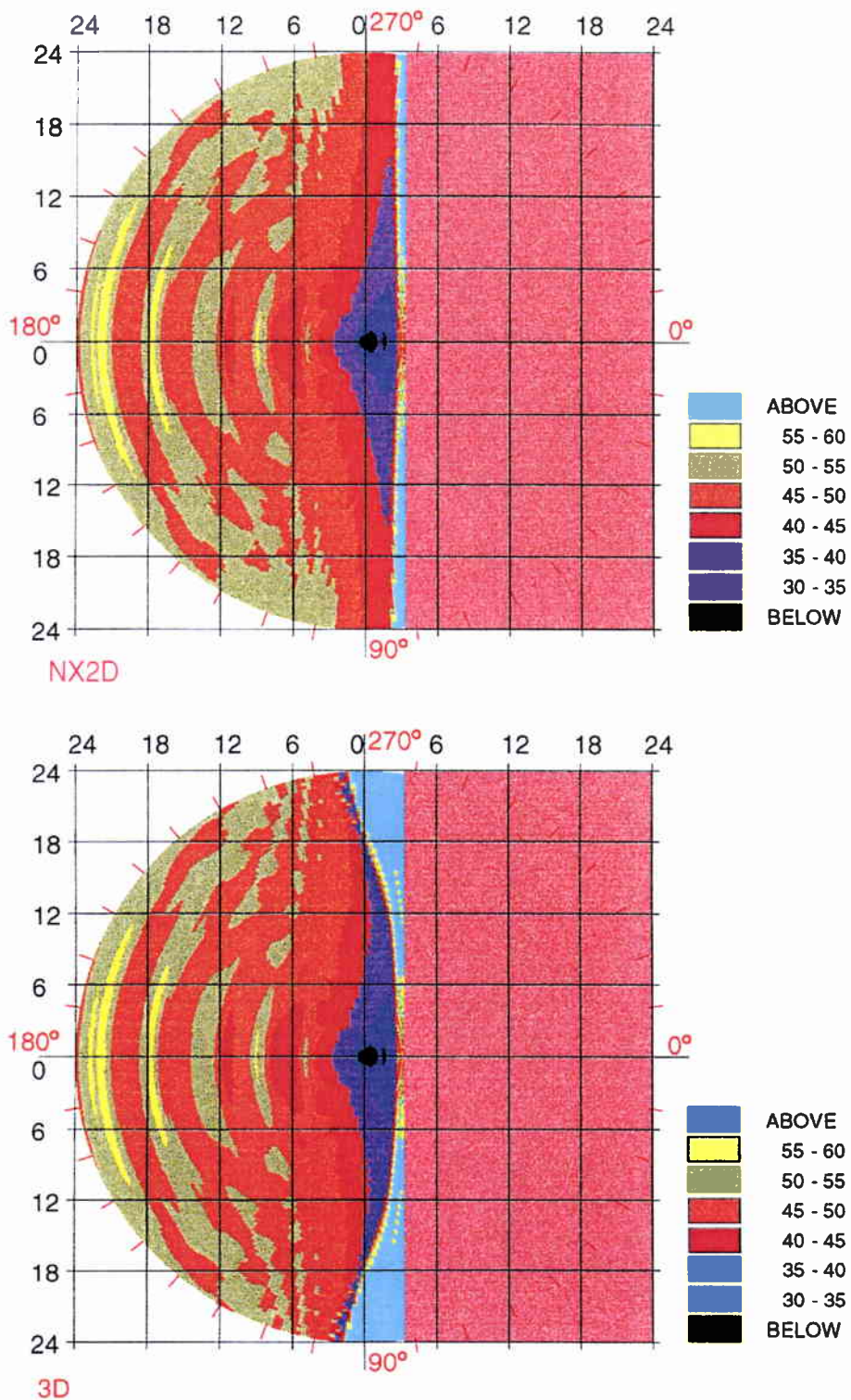


**Figure 3.6** Mode 2 - frequency 25 Hz, horizontal slices at constant depth  $z = 36$  m of the TL fields obtained using  $N \times 2D$  (upper figure) / three-dimensional (bottom figure) computations

SACLANTCEN SM-342

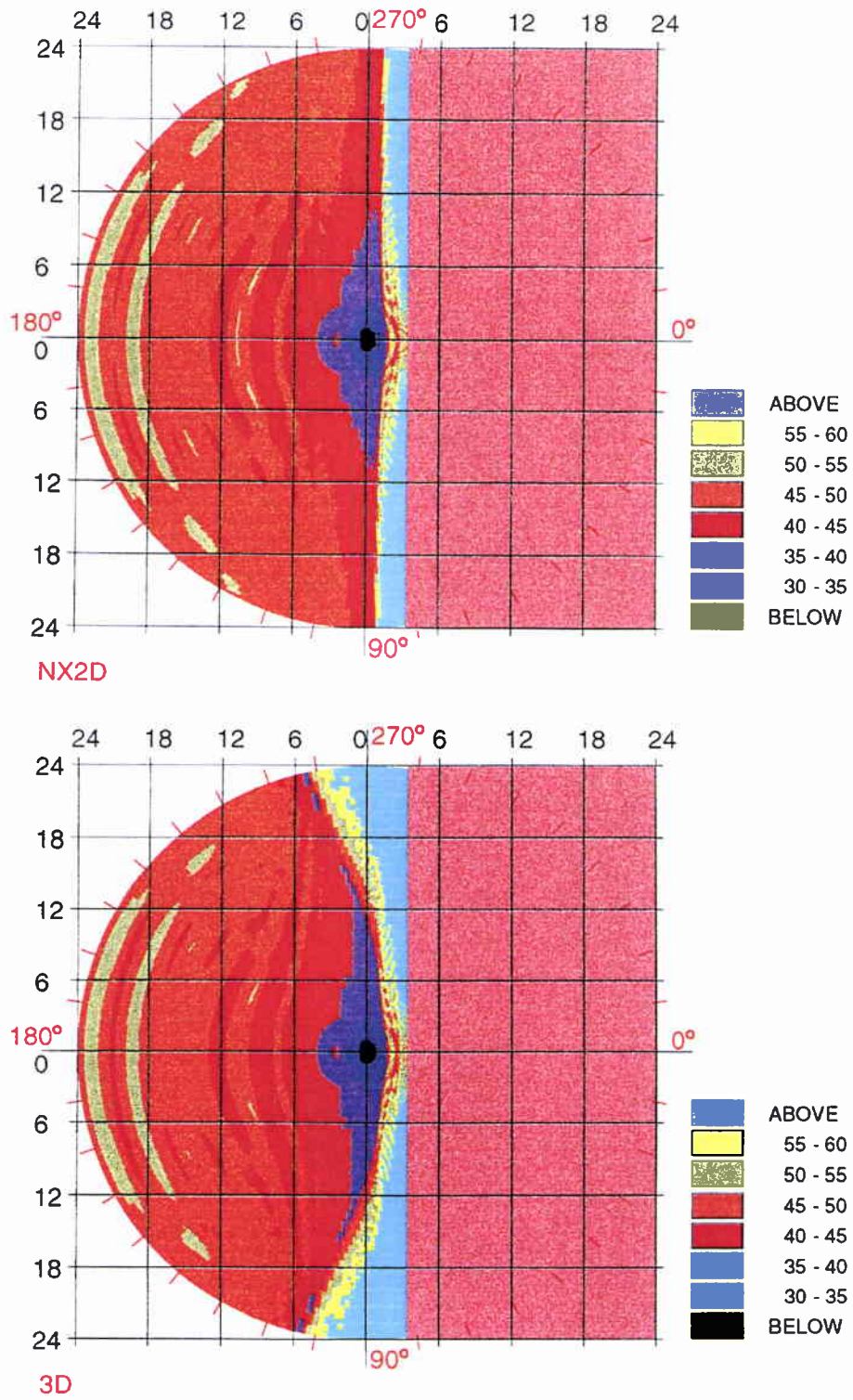


**Figure 3.7** Mode 3 - frequency 25 Hz, horizontal slices at constant depth  $z = 36$  m of the TL fields obtained using  $N \times 2D$  (upper figure) / three-dimensional (bottom figure) computations

### Convergence tests

One difficult and time-consuming issue in performing three-dimensional computations is to know whether or not the numerical solution is close enough to the exact solution of the continuous problem.

We denote by  $\Delta S$  the arclength increment expressed in meters and defined by  $\Delta S = 2\pi r \Delta\theta / 360$  where  $\Delta\theta$  is expressed in degrees.  $\Delta S$  is a function of  $r$  and  $\Delta\theta$ , i.e.,  $\Delta S = \Delta S(r, \Delta\theta)$ . The three-dimensional fields computed by TRIPARADIM (shown for restricted numbers of points in the TL horizontal slices) have been obtained using, in the mapped computation domain (image of the physical domain by the affine mapping defined by (A.1)),  $N = 130$  discrete points in depth (i.e.,  $\Delta y = 1/130$ , we recall that  $\Delta y$  is dimensionless),  $M = 11520$  discrete points in azimuth (i.e.,  $\Delta\theta \approx 0.031^\circ$ ) and  $\Delta r = 10$  m.

The mapped-domain constant increment  $\Delta y$  (see Eq. (A.14)) corresponds in the physical waveguide to  $8 \text{ m} \leq \Delta z(r, \theta) \leq 0.153 \text{ m}$  and for  $\theta = 90^\circ$  to  $\Delta z(r, \theta = 90^\circ) \approx 4 \text{ m}$ . By performing convergence tests, the size of  $\Delta r$  and  $\Delta z$  required for accurate three-dimensional computations can be easily determined using a non time-consuming  $N \times 2D$  model. The wavelength of the source is  $\lambda = 60$  m. The depth and range increment sizes have been chosen less than the wavelength, i.e.,  $\Delta r = \lambda/6$  and  $\Delta z(r, \theta = 90^\circ) \approx \lambda/15$ . No significant variation in the numerical solution has been observed for smaller increments in the depth and in the range directions. The azimuthal increment size, which ensures convergence, has also been found so that the arclength  $\Delta S$  corresponding to the maximum range  $R = 24$  km is less than the wavelength ( $\Delta S(R, 0.031^\circ = 90^\circ) \approx \lambda/4$ ).

The issue of selecting directly an appropriate  $\Delta\theta$  to ensure that convergence is reached is difficult due to the complicated three-dimensional effects and thus leads to a much more time-consuming analysis. *A priori*, we do not know whether horizontal refraction is neglectable or not. If the physical problem is weakly dependent on the azimuth, then a  $N \times 2D$  model will accurately model the wave field. In this case it is not necessary to model the azimuthal coupling of energy. But what do we understand by weakly dependent? In the present three-dimensional varying waveguide, the bottom slope is weak and nevertheless leads to large three-dimensional effects. A three-dimensional model is therefore needed.

We display in Figs. 3.8, 3.9, 3.10 TL vs. range curves corresponding, respectively, to mode 1, mode 2 and mode 3 obtained using different numbers of point  $M$  in azimuth, i.e., different increments  $\Delta\theta$ . In each figure, the bold solid line corresponds to a sufficiently accurate solution for  $\theta = 90^\circ$ . We also plot the corresponding  $N \times 2D$  reference solution ( $TL \propto 10 \log_{10} r$ ). The convergence is reached using  $M = 11520$  ( $\Delta\theta \approx 0.031^\circ$ ) for mode 1 and  $M = 5760$  ( $\Delta\theta \approx 0.062^\circ$ ) for both modes 2 and 3. We see the fringe pattern (*three-dimensional mode self-interference*) starting at approximately  $r = 18$  km for mode 1, and the shadow-zone region starting at 11 km for mode 3 and at 18 km for mode 2. We can also clearly observed the *three-dimensional mode self-interference* effects for modes 2 and 3 for ranges less than shadow-zone starting ranges, this effect being more pronounced for mode 2 (peak of intensity around  $r = 17$  km). Obviously, the smooth  $\propto 10 \log_{10} r$  behaviors of the  $N \times 2D$  solutions are drastically different from the three-dimensional solutions.

## SACLANTCEN SM-342

We notice that three-dimensional computation using  $M = 5760$  ( $\Delta\theta \approx 0.062^\circ$ ) is able to predict the *three-dimensional mode self-interference* effect of mode 1 and the solution using  $M = 2880$  ( $\Delta\theta = 0.125^\circ$ ) is also quite close to the convergence solution for mode 3 though differences are present in the shadow zone which starts approximately at  $r = 11$  km. The main three-dimensional effects for mode 1 and 3 are thus detected by three-dimensional computations using  $\Delta S \approx \lambda/2$ .

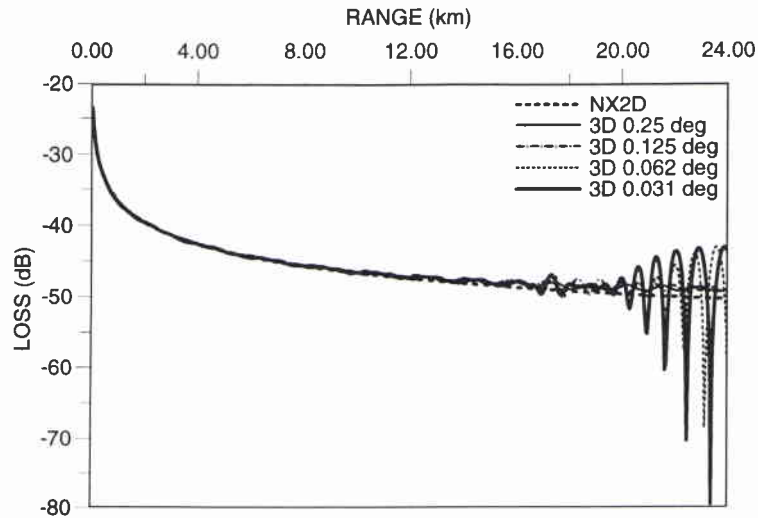


Figure 3.8 Convergence test for Mode 1 - frequency 25 Hz ( $\theta = 90^\circ$ ,  $z = 36$  m)

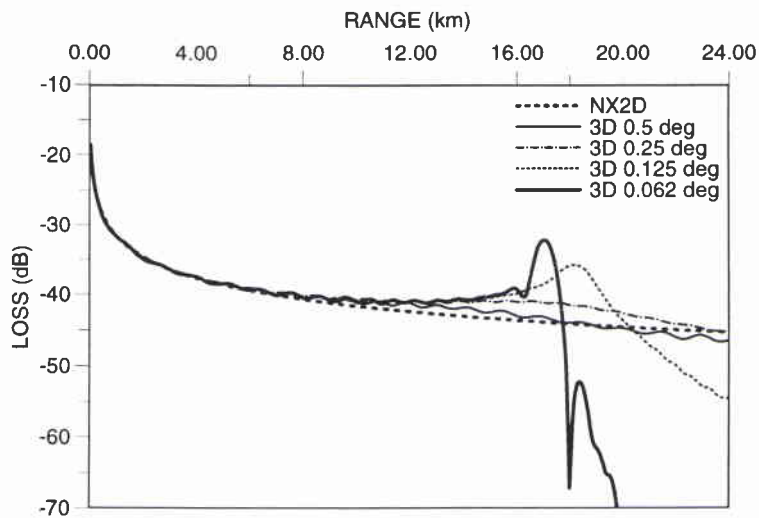
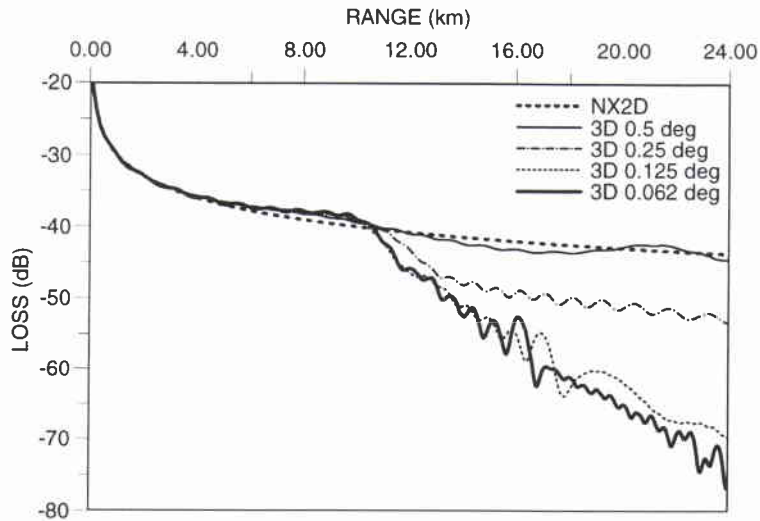


Figure 3.9 Convergence test for Mode 2 - frequency 25 Hz ( $\theta = 90^\circ$ ,  $z = 36$  m)



**Figure 3.10** Convergence test for Mode 3 - frequency 25 Hz ( $\theta = 90^\circ$ ,  $z = 36$  m)

Therefore, selecting  $\Delta\theta$  which corresponds to an arclength increment approximately equal to  $\lambda$  at the maximum computation range  $R$  appears to be a reasonable starting value for processing future convergence tests. If one attempts convergence tests with  $\Delta\theta$  corresponding to  $\Delta S(R, \Delta\theta) \gg \lambda$ , it may be erroneously concluded that three-dimensional effects are very small for  $0 \leq r \leq R$ .

### Comparison with FAWPE

We now compare the solution obtained with TRIPARADIM to the solution obtained with FAWPE. The range increment  $\Delta r$  is identical for the two models. The depth increment  $\Delta z$  used in FAWPE is given by  $\Delta z = 4$  m and is constant in all the waveguide. The depth increment is thus identical for both models for  $\theta = 90^\circ$ . FAWPE requires at least 2048 azimuthal FFT components to get an accurate solution (no significant and interesting improvement has been obtained using 4096 azimuthal FFT components).

For FAWPE, the artificial interface is placed at  $z_2 = 780$  m (identical to the actual artificial interface depth handled by TRIPARADIM at  $r = 0$ ) and the pressure-released bottom is placed at  $z_{\max} = 2048$  m which is nearly two-times the rigid bottom depth handled by TRIPARADIM at  $r = 0$  (there are less problems of memory storage with FAWPE). We emphasize the fact that these two boundaries are assumed to be constant in all the waveguide in FAWPE computations whereas they are non-constant in TRIPARADIM computations due to the hypothesis of homothetical layers (cf. Fig. 3.3).

We plot in Figs. 3.11, 3.12, 3.13 the solutions obtained with both models, corresponding respectively to mode 1, mode 2 and mode 3. We also plot the corresponding  $N \times 2D$  reference solution ( $TL \propto 10 \log_{10} r$ ). We observe that both models predict qualitatively the same three-dimensional effects for each mode. However, there are some quantitative differences. We observe a shift in the phasing for each mode. The amplitudes agree except for lower energies (shadow-zone regions for modes 2 and 3).

SACLANTCEN SM-342

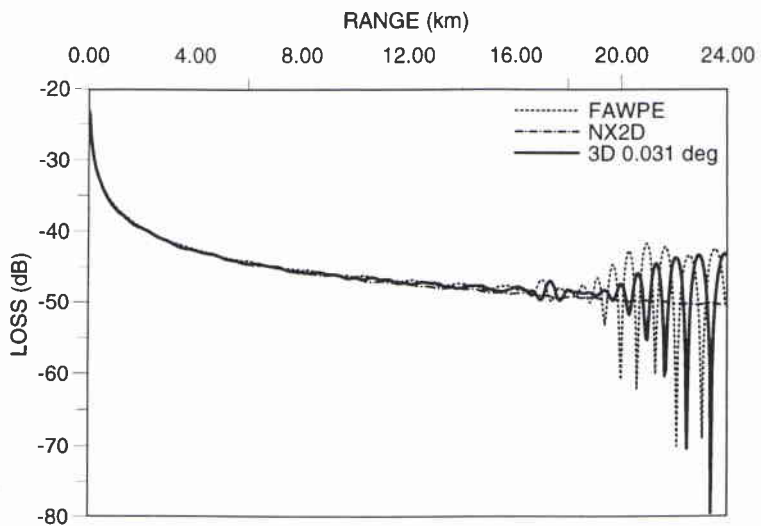


Figure 3.11 Comparison for Mode 1 - frequency 25 Hz ( $\theta = 90^\circ$ ,  $z = 36$  m)

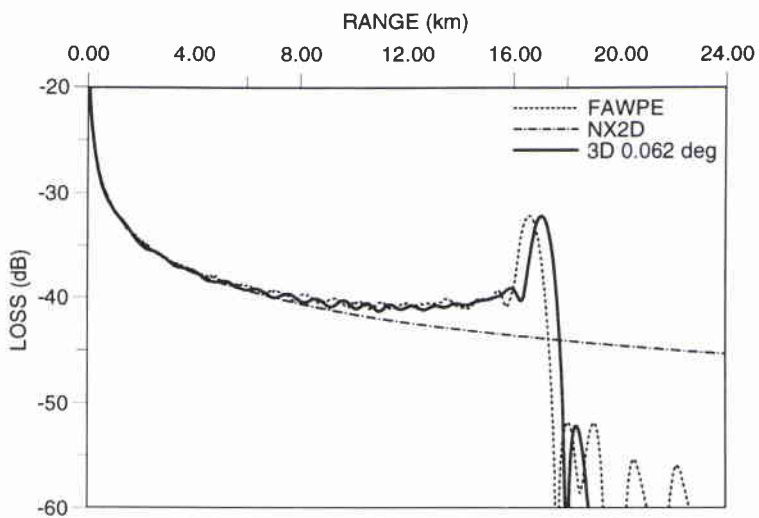
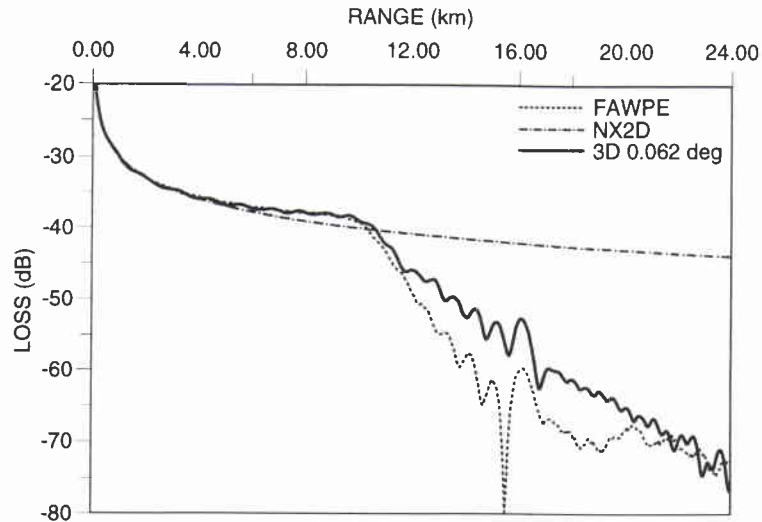


Figure 3.12 Comparison for Mode 2 - frequency 25 Hz ( $\theta = 90^\circ$ ,  $z = 36$  m)



**Figure 3.13** Comparison for Mode 3 - frequency 25 Hz ( $\theta = 90^\circ$ ,  $z = 36$  m)

We did not expect perfect agreement of the two solutions. The mathematical derivations are different though they are both based on a linear paraxial approximation. The treatment of the three-dimensional varying bottoms differs from FAWPE which assumes local horizontal bottoms (cf. subsection 2.3) to TRIPARADIM which models accurately the sloping bottoms via the use of an affine mapping (cf. subsection A.1) and adapts the leading-interface conditions to its paraxial modelling and is hence energy conserving (cf. subsection 2.2). Both models use different approximations of the original problem (based on the Helmholtz equation) but yield approximately the same results. FAWPE, which uses FFTs to model its azimuthal operator, requires fewer azimuthal points for a converged solution than does TRIPARADIM.

The disagreements present at the low-levels are not due to the differences in the modelling but seem to be due to different ways of treating the non-attenuating halfspace. As discussed in subsection 3.1, the use of the affine mapping in TRIPARADIM requires non-horizontal artificial absorbing layers. Due to the memory storage limitations, the actual artificial layer is not wide enough to properly attenuate sound propagating inside the bottom, causing reflections on the rigid bottom. This can explain the presence of spurious energy in shadow-zone region. As we will see in the next subsection, introducing attenuation in the bottom will improve the agreement for the lower energies.

### 3.4 Attenuating halfspace bottom

We consider the same three-dimensional wedge-shaped waveguide as in the previous subsection. We now assume the halfspace bottom to be attenuating, i.e.,  $\alpha_1 = 0.5$  dB/ $\lambda$ . No attenuation is assumed in the water column, i.e.,  $\alpha_0 = 0$  dB/ $\lambda$ . We consider different source frequencies (5 Hz, 15 Hz, 25 Hz).

SACLANTCEN SM-342

**Source frequency 5 Hz**

We first consider a point source emitting at a frequency of 5 Hz (i.e., wavelength  $\lambda = 300$  m), leading to only one propagating mode for  $\theta = 90^\circ$  (cf. Table 1). The grazing angle is given by  $\vartheta_1 \approx 25.91$  deg. The initial field is given at each discrete azimuth by Eq. (3.3). No normalization constant is used. The reference sound speed is selected accordingly, i.e.,  $c_{\text{ref}} = c_{r,1}$  where  $c_{r,1} \approx 1667.73$  m/s is the modal phase velocity. The computations have been done using  $z_2 = 2000$  m,  $z_{\text{max}} = 3173$  m at  $r = 0$  and using in the mapped computation domain  $N = 211$  discrete points in depth ( $\Delta y = 1/211$ ),  $M = 720$  discrete points in azimuth ( $\Delta\theta = 0.5^\circ$ ) and  $\Delta r = 30$  m. The mapped constant increment  $\Delta y$  corresponds in the physical waveguide at  $\theta = 90^\circ$  to  $\Delta z(r, \theta = 90^\circ) \approx 7.5$  m.

We show in lower plot of Fig. 3.14 a color-scaled TL plot (horizontal slice at constant depth  $z = 36$  m) of the three-dimensional field. We also display the corresponding  $N \times 2D$  field in the upper plot of Fig. 3.14.

We observe the strong three-dimensional horizontal refraction effects present at this very-low frequency, leading to a shadow-zone region. For azimuthal angles close to  $\theta = 0^\circ$  and  $\theta = 180^\circ$ , the  $N \times 2D$  and 3D solutions agree closely (this observation will be valid for all the frequencies).

We notice in Fig. 3.15 that using  $M = 720$  ( $\Delta\theta = 0.5^\circ$ ) discrete points in azimuth is sufficient to describe the shadow-zone region for  $\theta = 90^\circ$ . We notice that using less points in azimuth is also sufficient to predict the *three-dimensional mode shadowing* effect present at  $r \approx 5$  km. Using  $M = 180$  ( $\Delta\theta = 2^\circ$ ) leads to the arclength increment  $\Delta S(5 \text{ km}, 2^\circ) \approx \lambda/2$ , the solution is accurate until approximately  $r = 10$  km where it starts to deflect from the correct solution, the arclength increment being at this range greater than  $\lambda$ .

We show in Fig. 3.16 the good agreement of the two solutions obtained by TRIPARADIM and FAWPE (512 FFT azimuthal components are sufficient). Introducing attenuation in the halfspace bottom, we have eliminated the problem of spurious reflection on the rigid bottom. There is now good agreement for the lower energies.

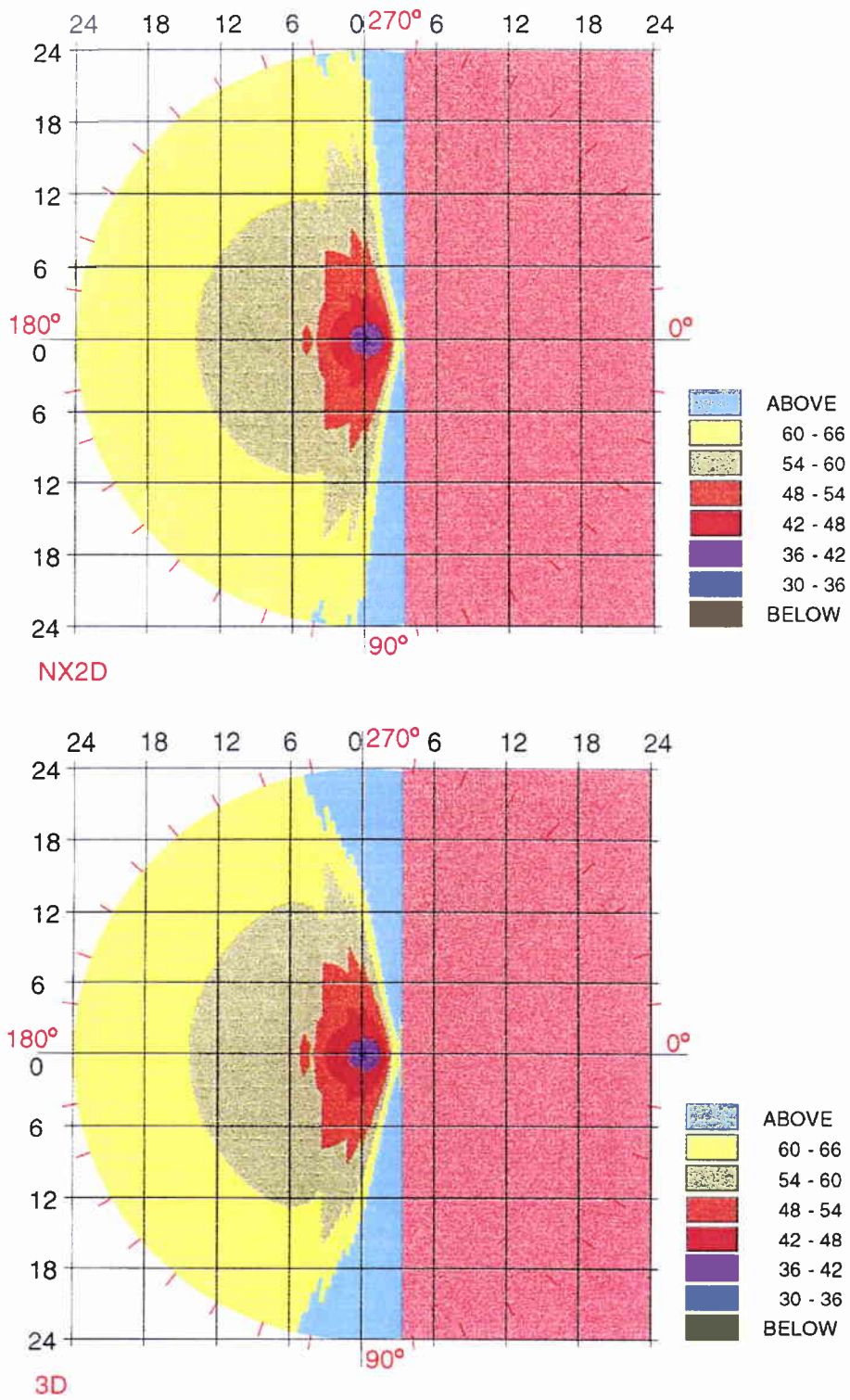


**Figure 3.14** Mode 1 - frequency 5 Hz, horizontal slices at constant depth  $z = 36$  m of the TL fields obtained using  $N \times 2D$  (upper figure) / three-dimensional (bottom figure) computa

SACLANTCEN SM-342

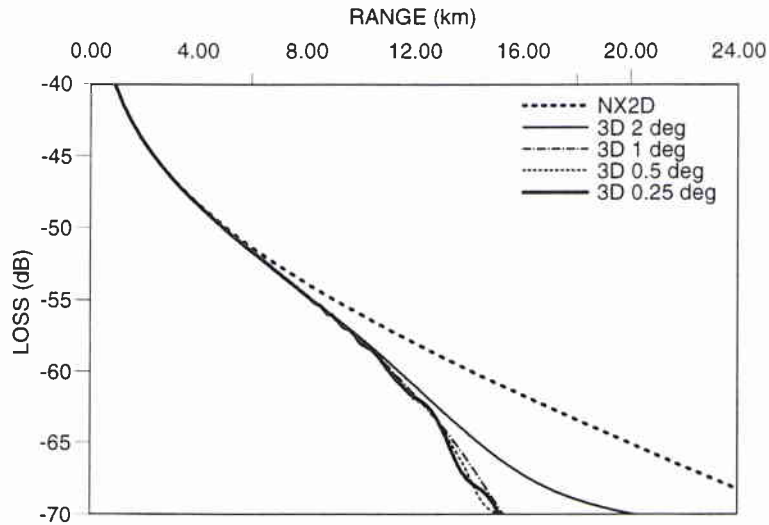


Figure 3.15 Convergence test for Mode 1 - frequency 5 Hz ( $\theta = 90^\circ$ ,  $z = 36$  m)

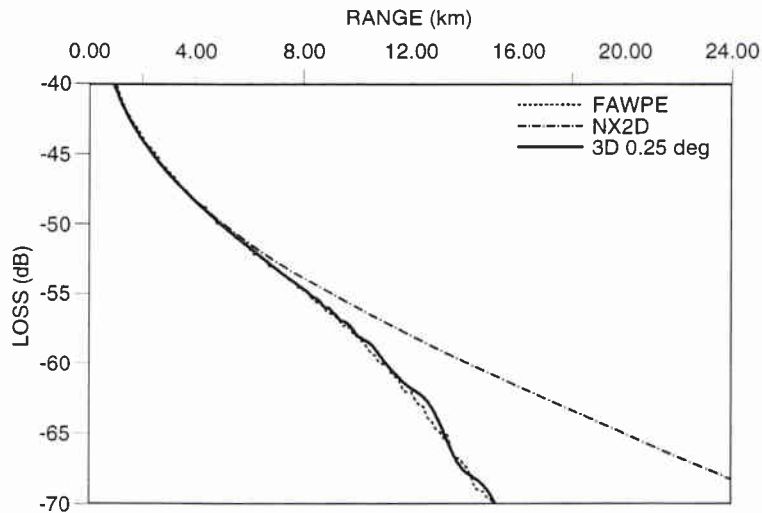
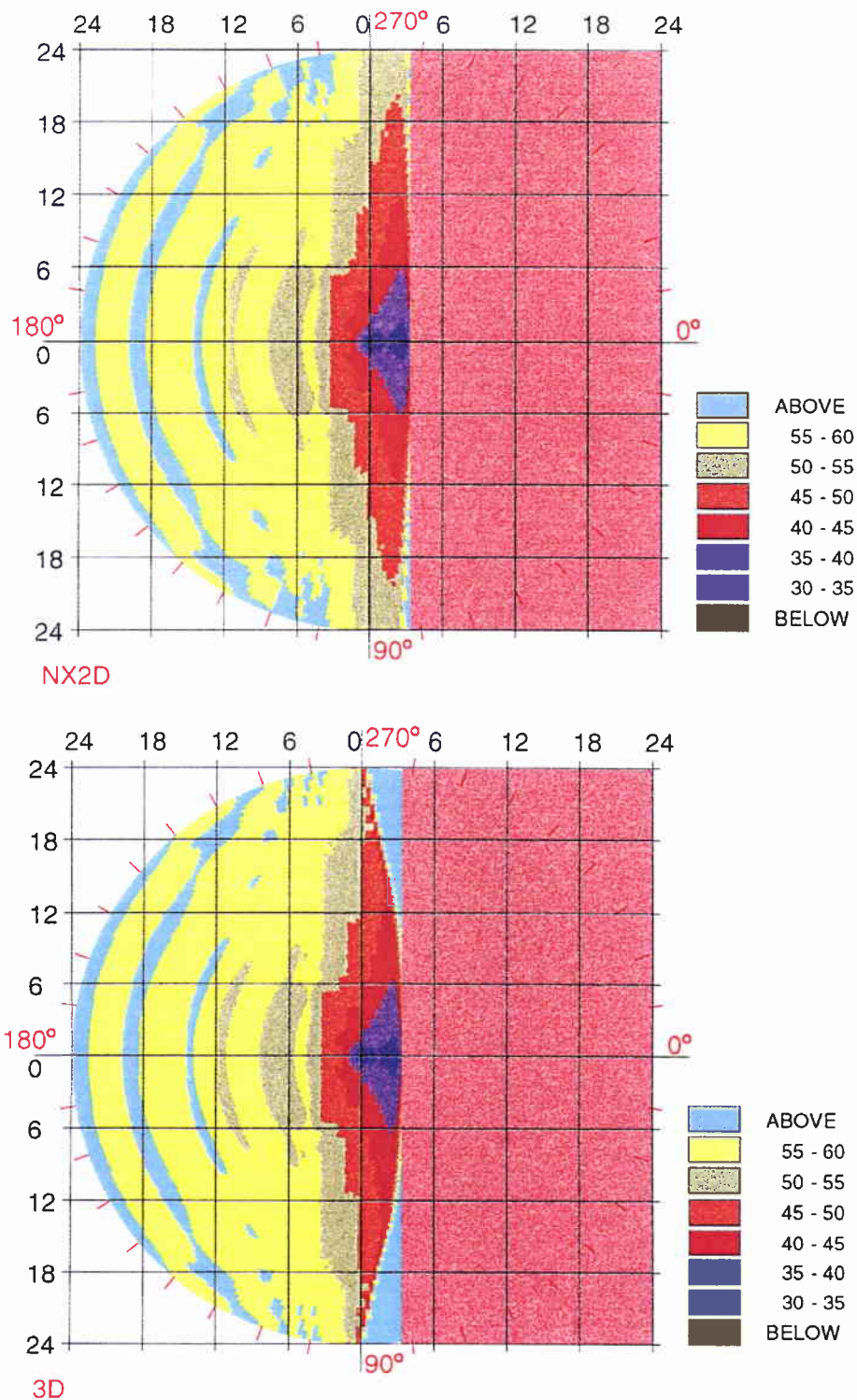


Figure 3.16 Comparison for Mode 1 - frequency 5 Hz ( $\theta = 90^\circ$ ,  $z = 36$  m)

### Source frequency 15 Hz

We now consider a point source emitting at frequency 15 Hz (i.e., wavelength  $\lambda = 100$  m), leading to two propagating modes for  $\theta = 90^\circ$  with grazing angles  $\vartheta_1 \approx 11.59^\circ$  (mode 1) and  $\vartheta_2 \approx 23.88^\circ$  (mode 2). We compute the three-dimensional propagation fields corresponding to each modal initialization given by Eq. (3.3). When initializing by mode 1 or 2 separately, the reference sound speed is chosen accordingly, i.e.,  $c_{\text{ref}} \approx 1531.24$  m/s for mode 1 and  $c_{\text{ref}} \approx 1640.51$  m/s for mode 2.



**Figure 3.17** Mode 1 - frequency 15 Hz, horizontal slices at constant depth  $z = 36$  m of the TL fields obtained using  $N \times 2D$  (upper figure) / three-dimensional (bottom figure) computations

SACLANTCEN SM-342

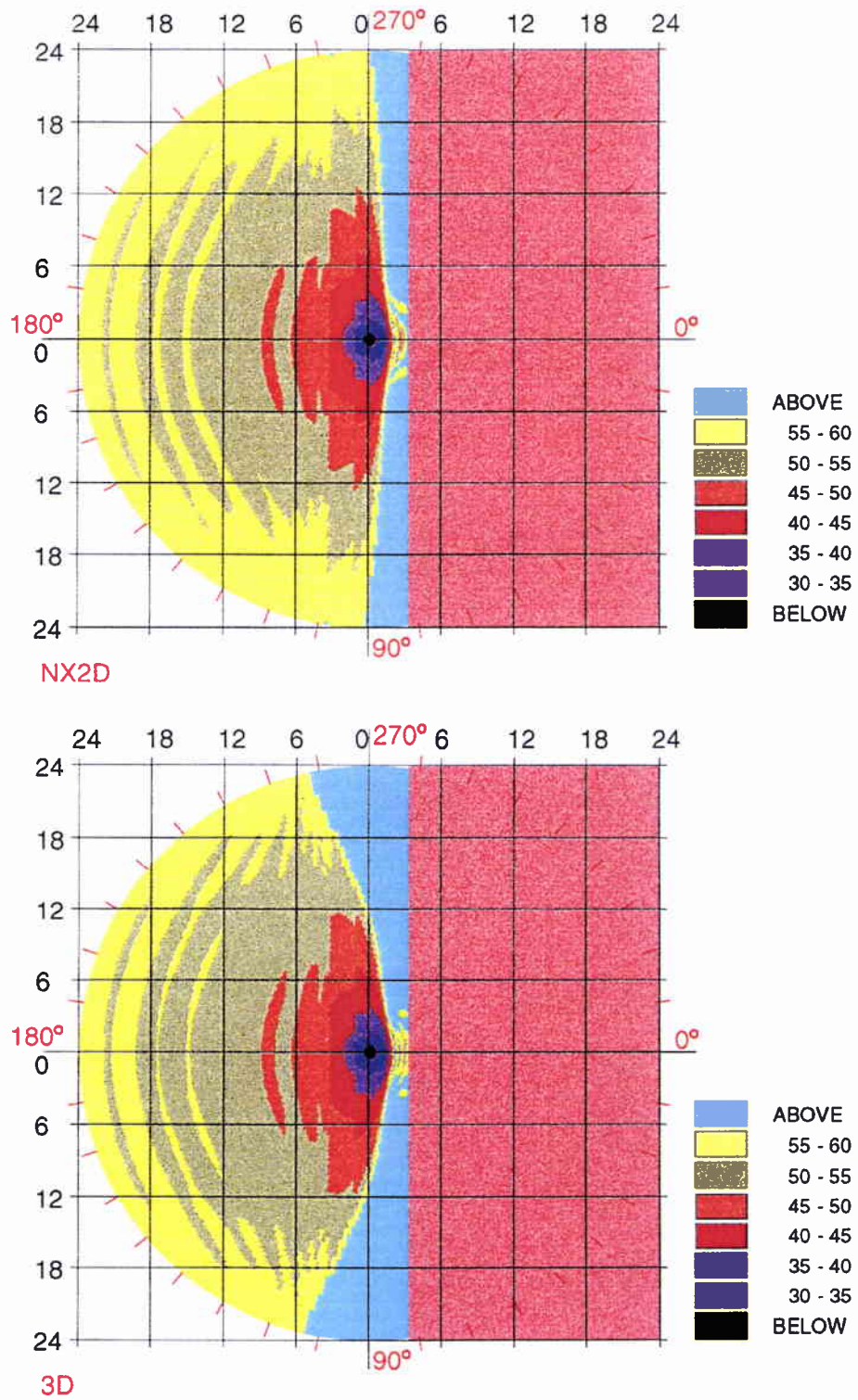


**Figure 3.18** Mode 2 - frequency 15 Hz, horizontal slices at constant depth  $z = 36$  m of the TL fields obtained using  $N \times 2D$  (upper figure) / three-dimensional (bottom figure) computations

For each modal initialization, the initial field is assumed to be omnidirectional. The computations have been done using  $z_2 = 1380$  m,  $z_{\max} = 1840$  m at  $r = 0$  and using in the mapped computation domain  $N = 122$  discrete points in depth ( $\Delta y = 1/122$ ),  $M = 2880$  discrete points in azimuth ( $\Delta\theta = 0.125^\circ$ ) and  $\Delta r = 15$  m. We have for  $\theta = 90^\circ$   $\Delta z(r, \theta = 90^\circ) \approx 7.5$  m.

We display in Figs. 3.17 and 3.18 (lower plots) color-scaled TL plots (horizontal slices at constant depth  $z = 36$  m) of the field corresponding, respectively, to mode 1 and mode 2. We also display the corresponding  $N \times 2D$  fields in the upper plots of Figs. 3.17 and 3.18. We observe the three-dimensional horizontal refraction effects for both mode 1 and mode 2. Because the grazing angle of mode 2 ( $\vartheta_2 \approx 23.88^\circ$ ) is steeper than that of mode 1 ( $\vartheta_1 \approx 11.59^\circ$ ), this effect is more pronounced for mode 2. We also observe the fringe pattern (*three-dimensional mode self-interference* effect) for mode 1.

We show in Figs. 3.19 and 3.20 the TL vs. range convergence curves for both modes. The *three-dimensional mode self-interference* effect of mode 1 appears for  $r > 20$  km and at least  $M = 2880$  ( $\Delta\theta = 0.125^\circ$ ) points are required to get an accurate three-dimensional solution. This corresponds to  $\Delta S(R, 0.125^\circ) \approx \lambda/2$ .

Three-dimensional computations using larger  $\Delta\theta$ , e.g.,  $\Delta\theta = 0.25^\circ$  ( $\Delta S(R, 0.25^\circ) \approx \lambda$ ), are unable to describe accurately this effect despite large differences with the smooth  $N \times 2D$  solution. For mode 2, the *three-dimensional mode shadowing* effect appear very slightly at approximately  $r = 7$  km. At this range less points in azimuth are needed. However, this three-dimensional effect becomes stronger with range, the correct shadow-zone region being quite well predicted using  $M = 1440$  ( $\Delta\theta = 0.25^\circ$ ) and more accurately described using  $M = 2880$  ( $\Delta\theta = 0.125^\circ$ ).

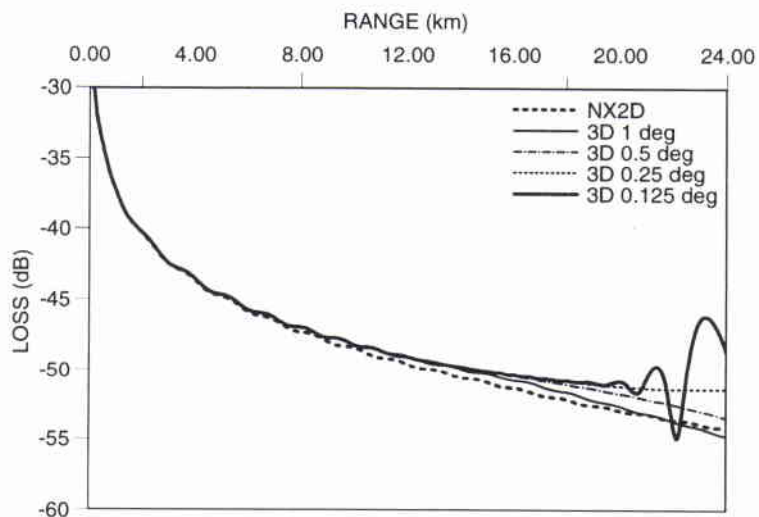


**Figure 3.19** Convergence test for Mode 1 - frequency 15 Hz ( $\theta = 90$  deg,  $z = 36$  m)

SACLANTCEN SM-342

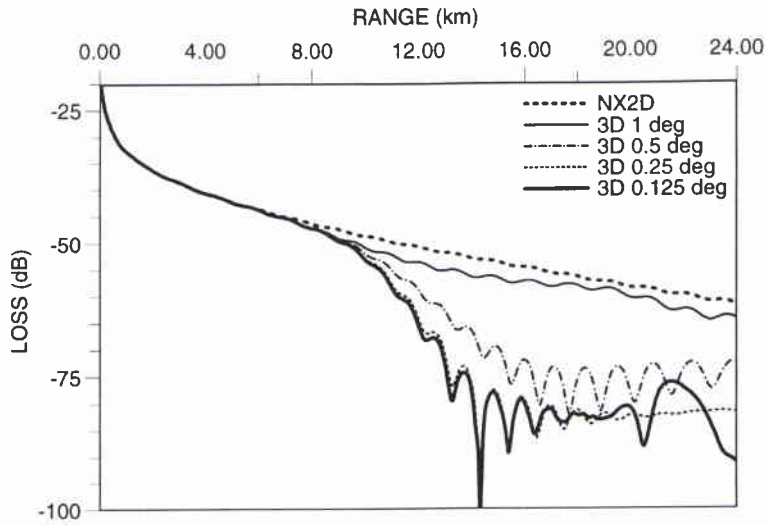


**Figure 3.20** Convergence test for Mode 2 - frequency 15 Hz ( $\theta = 90$  deg,  $z = 36$  m)

We show in Figs. 3.21 and 3.22 the solutions obtained with FAWPE corresponding, respectively, to mode 1 and mode 2. We observe a quite good agreement (even for low-level amplitudes) in Fig. 3.22, no phase shift being present.

We observe in Fig. 3.21 a disagreement in the phasing. We already noticed such a shift in the phasing for mode 1 corresponding to frequency 25 Hz (cf. subsection 3.3). Nevertheless, both models describe qualitatively the same three-dimensional effects.

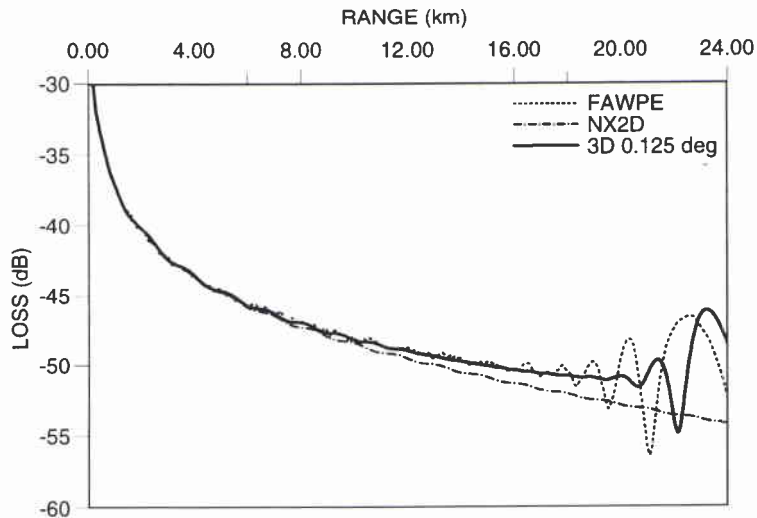


**Figure 3.21** Comparison for Mode 1 - frequency 15 Hz ( $\theta = 90^\circ$ ,  $z = 36$  m)

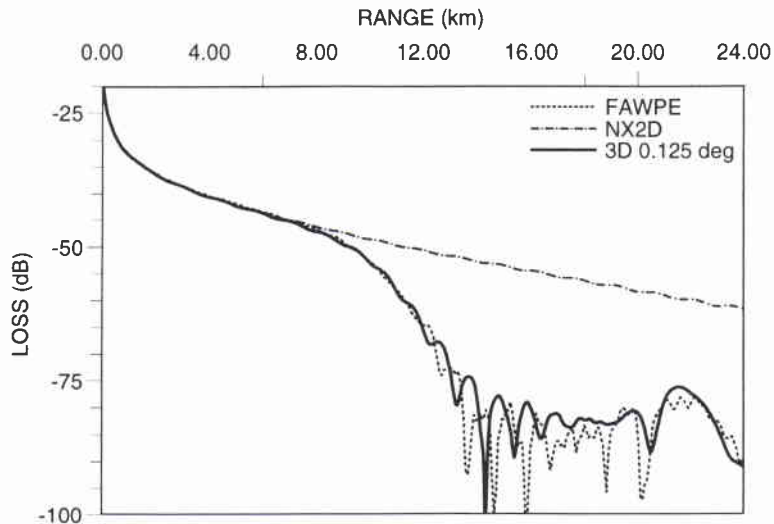


**Figure 3.22** Comparison for Mode 2 - frequency 15 Hz ( $\theta = 90^\circ$ ,  $z = 36$  m)

We now initialize the field considering a CW point source ( $f = 15$  Hz,  $z_s = 80$  m) and retaining only the 2 propagating modes. The initial field is given by Eq. (3.5) for  $m_p = 2$ , the modes are normalized using Eq. (3.6). In this case, the reference sound speed is selected equal to the water column sound speed, i.e.,  $c_{ref} = 1500$  m/s.

We show in Figs. 3.23 the TL horizontal slices ( $z = 36$  m) corresponding, respectively, to N $\times$ 2D (upper plot) and 3D (lower plot) solutions. We show in Fig. 3.24 the corresponding TL vertical slices ( $\theta = 90^\circ$ ) and in Fig. 3.25 below the TL vs. range curves ( $\theta = 90^\circ$ ,  $z = 36$  m). Due to the convergence analysis made for modes 1 and 2, we have used  $\Delta\theta = 0.125^\circ$  in the three-dimensional computations.

We observe noticeable differences in both fields. We observe in the upper plot of Fig. 3.24 for  $0 \leq r \leq R$  the interference pattern due to two propagating modes predicted by N $\times$ 2D model. As can be seen in the lower plot of Fig. 3.24 and in Fig. 3.25, the propagation field predicted by three-dimensional computation is different, especially for  $r \geq 7$  km where the *three-dimensional mode shadowing* effect of mode 2 approximately starts. For  $r \geq 7$  km, the influence of mode 2 in the interference pattern progressively disappears, leading to only one propagating mode for  $r$  greater than 14 km, including the *three-dimensional mode self-interference* effect of mode 1 for  $20 \text{ km} \leq r \leq R$ .

SACLANTCEN SM-342

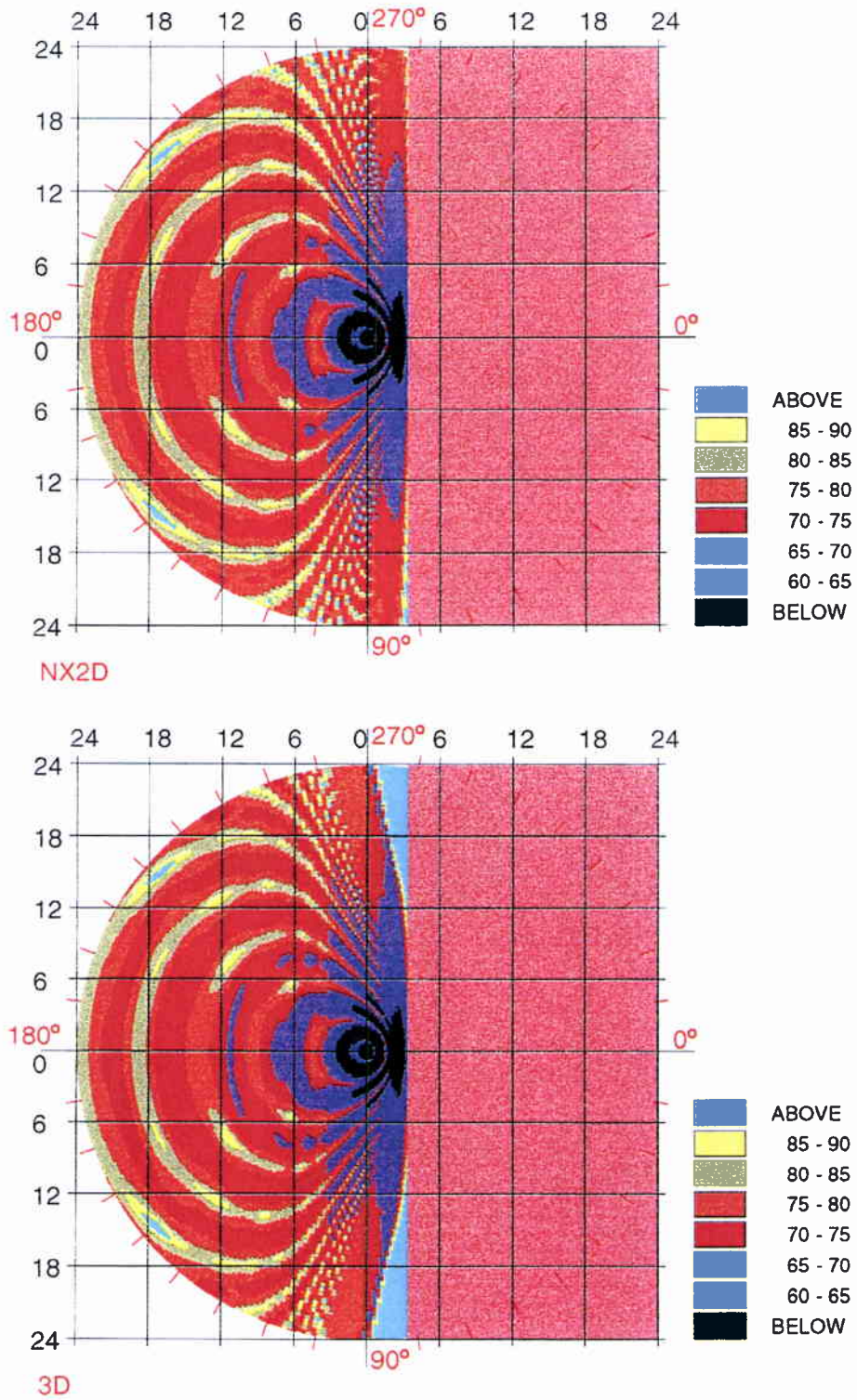


**Figure 3.23** CW point source (15 Hz), horizontal slices at constant depth  $z = 36$  m of the TL fields obtained using  $N \times 2D$  (upper figure) / three-dimensional (bottom figure) computations

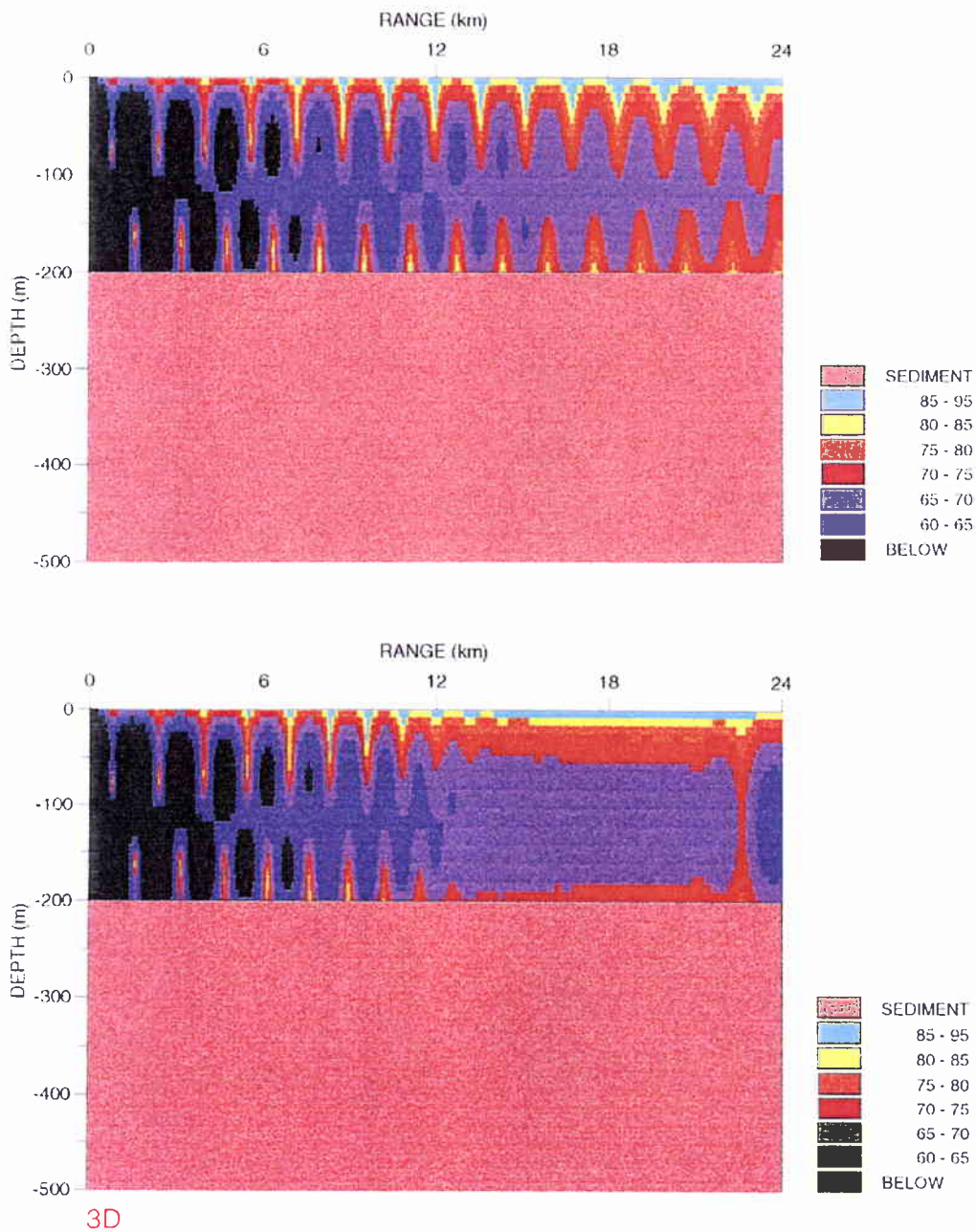


**Figure 3.24** CW point source (15 Hz), vertical slices at constant azimuth  $\theta = 90^\circ$  of the TL fields obtained using  $N \times 2D$  (upper figure) / three-dimensional (bottom figure) computations

SACLANTCEN SM-342

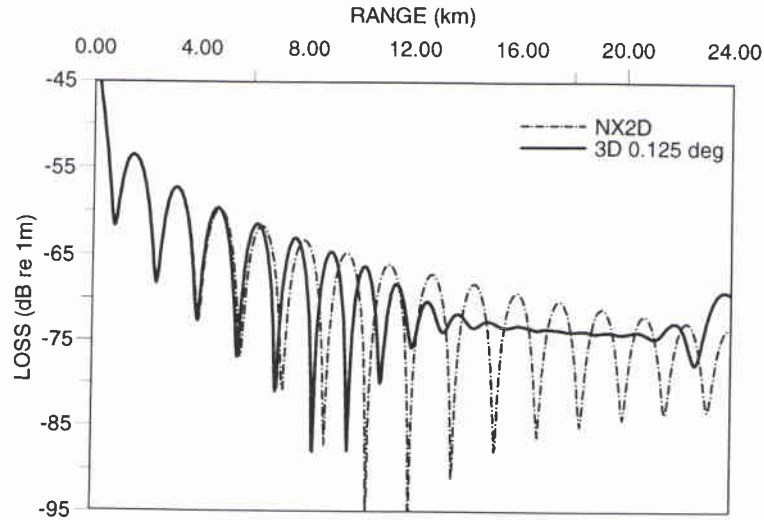


Figure 3.25 Comparison for CW point source - frequency 15 Hz ( $\theta = 90^\circ$ ,  $z = 36$  m)

### Source frequency 25 Hz

We consider a point source emitting at frequency 25 Hz (i.e., wavelength  $\lambda = 60$  m) leading to three propagating modes for  $\theta = 90^\circ$  (cf. Table 1) of vertical grazing angles  $\vartheta_1 \approx 7.49^\circ$  (mode 1),  $\vartheta_2 \approx 15.20^\circ$  (mode 2) and  $\vartheta_3 \approx 23.23^\circ$  (mode 3). This frequency has already been considered and analyzed in subsection 3.3 for a non-attenuating halfspace bottom. We compute the three-dimensional fields corresponding to each modal initialization given by Eq. (3.3),  $1 \leq m \leq 3$ , using the same inputs as described in subsection 3.3. The only differences in the inputs is the attenuation coefficient in the halfspace bottom, now equal to  $0.5$  dB/ $\lambda$ . For each initialization, the initial field is assumed to be omnidirectional.

We display in Figs. 3.26, 3.27 and 3.28 (lower plots) color-scaled TL plots (horizontal slices at constant depth  $z = 36$  m) of the three-dimensional field corresponding, respectively, to modes 1, 2 and 3. We also display the corresponding  $N \times 2D$  fields in the upper plots of Figs. 3.26, 3.27 and 3.28. We can formulate the same observations as we did in subsection 3.3 for all the three propagation fields corresponding to modes 1, 2 and 3.

We show in Figs. 3.29, 3.30, 3.31 ( $\theta = 90$  deg,  $z = 36$  m) the solutions obtained with the two models TRIPARADIM and FAWPE. We notice that the shifts in the phasing previously observed for the non-attenuating halfspace bottom are still present for each mode. We also notice the good agreement in the levels for the shadow-zone region (low-level) compared to the agreement in Fig. 3.20, which suggests that the previous differences were due to insufficient attenuation in the halfspace bottom. The shift in the phasing being still present, we conclude this disagreement is definitely due to the differences of the two models.

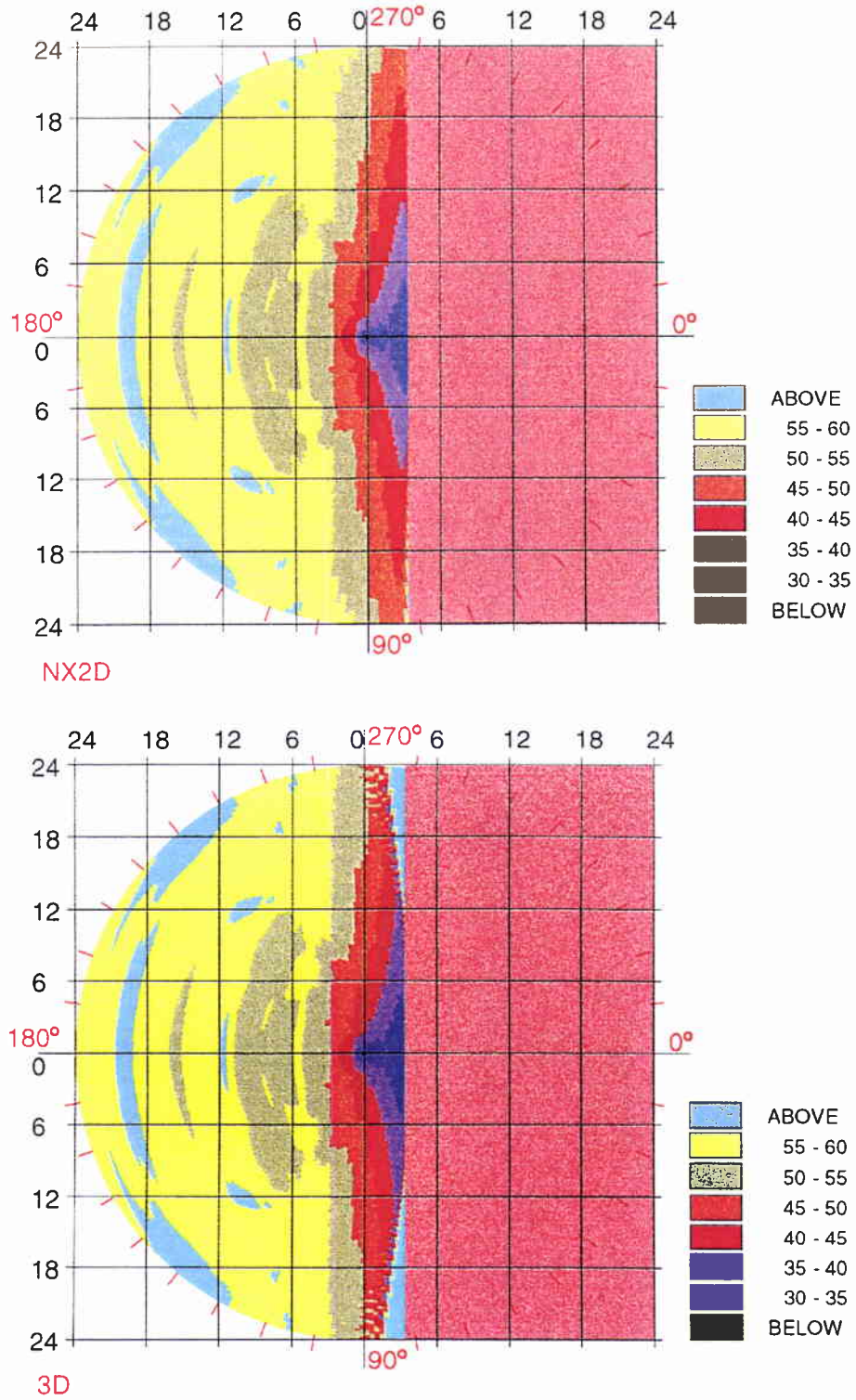


**Figure 3.26** Mode 1 - frequency 25 Hz, horizontal slices at constant depth  $z = 36$  m of the TL fields obtained using  $N \times 2D$  (upper figure) / three-dimensional (bottom figure) computations

SACLANTCEN SM-342

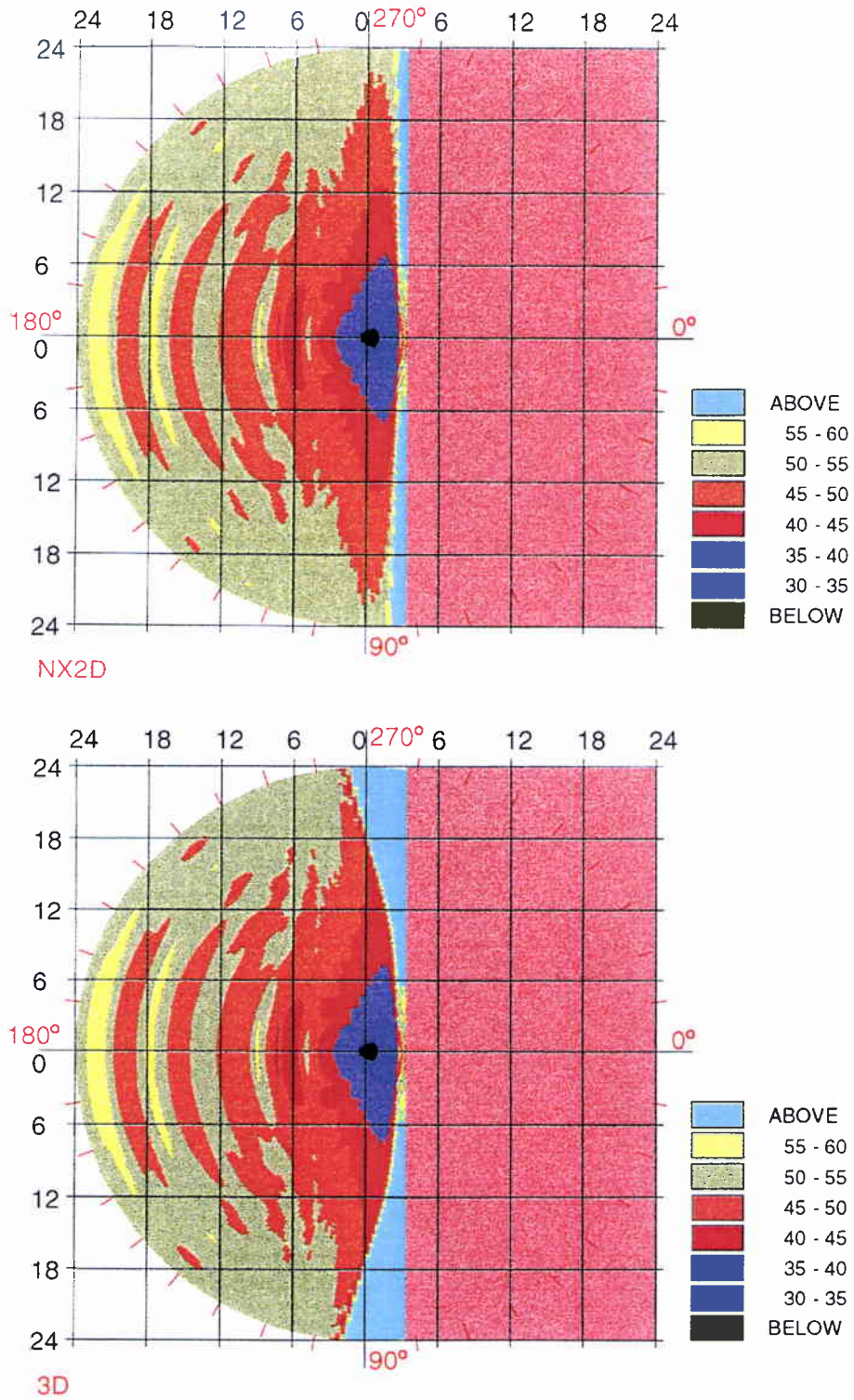


**Figure 3.27** Mode 2 - frequency 25 Hz, horizontal slices at constant depth  $z = 36$  m of the TL fields obtained using  $N \times 2D$  (upper figure) / three-dimensional (bottom figure) computations

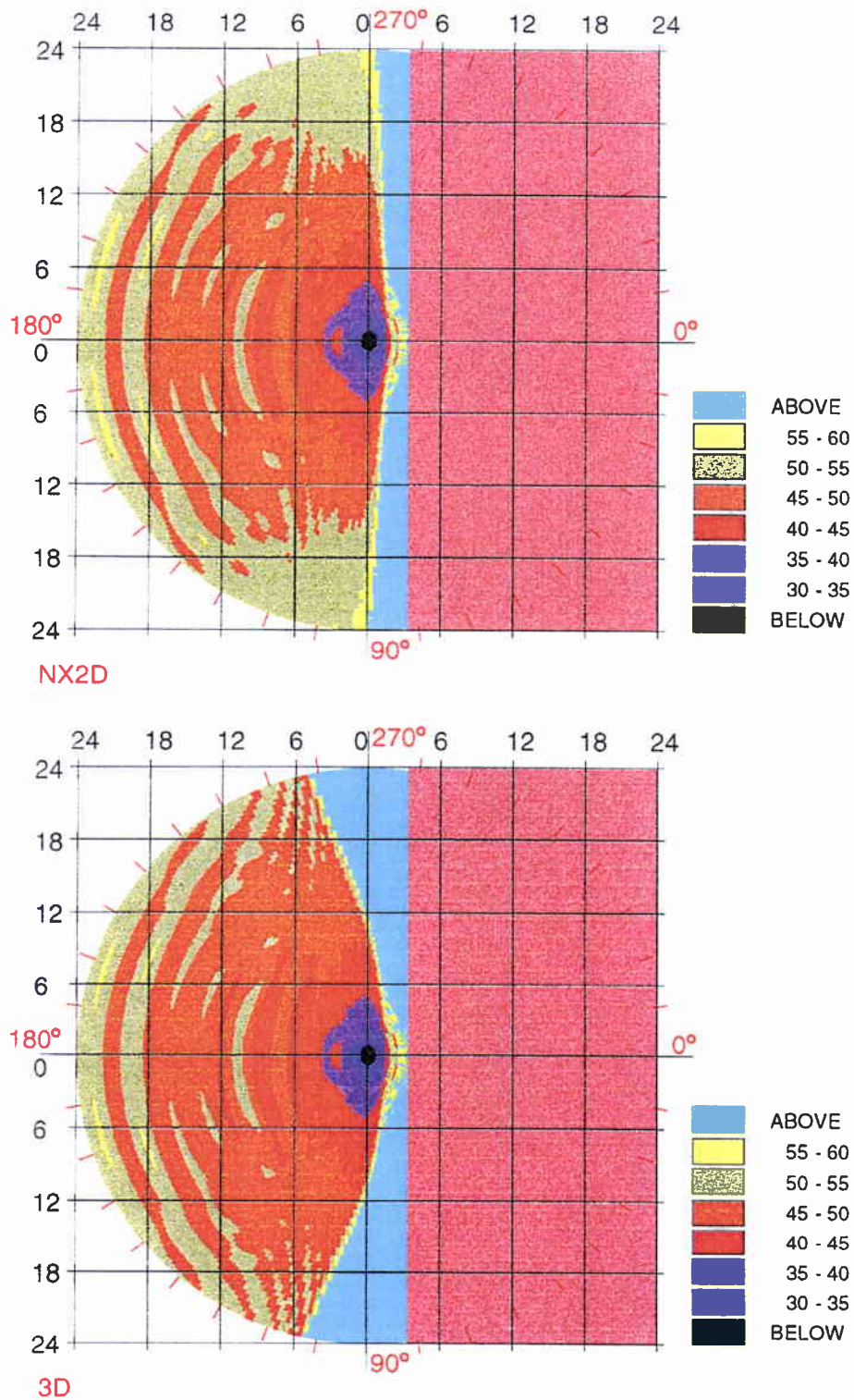


**Figure 3.28** Mode 3 - frequency 25 Hz, horizontal slices at constant depth  $z = 36$  m of the TL fields obtained using  $N \times 2D$  (upper figure) / three-dimensional (bottom figure) computations

SACLANTCEN SM-342

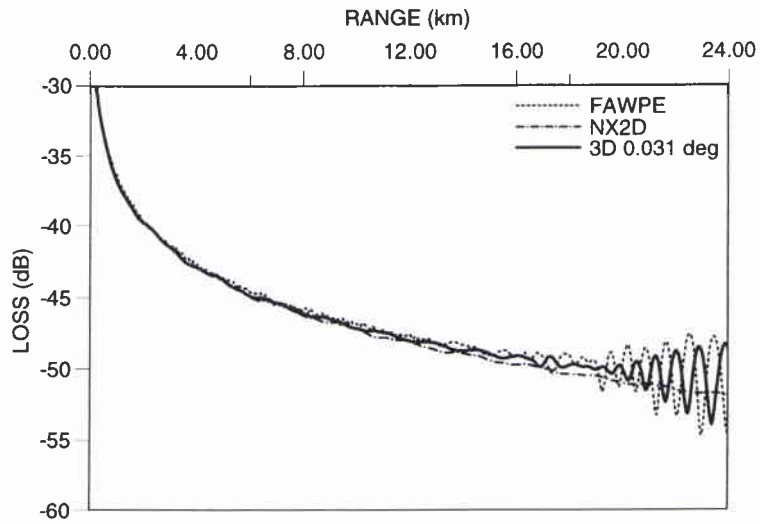


Figure 3.29 Comparison test for Mode 1 - frequency 25 Hz ( $\theta = 90^\circ$ ,  $z = 36$  m)

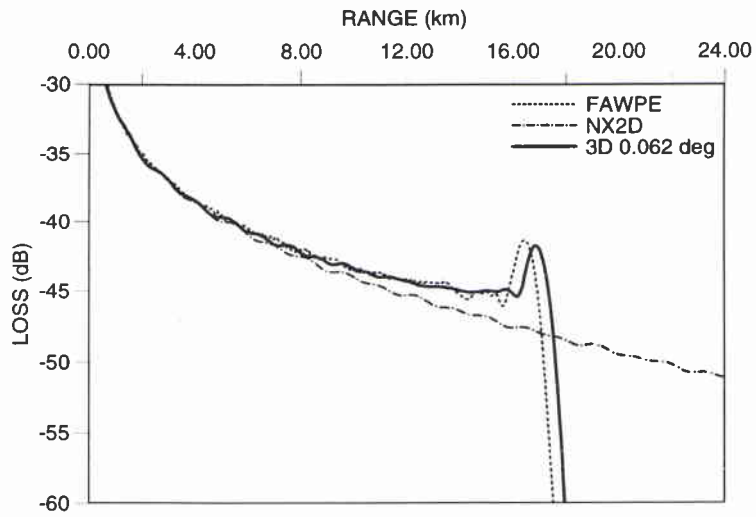
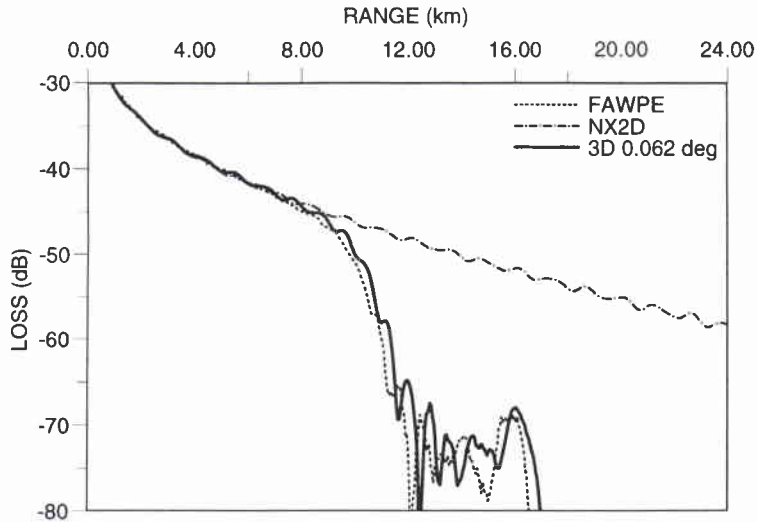


Figure 3.30 Comparison test for Mode 2 - frequency 25 Hz ( $\theta = 90^\circ$ ,  $z = 36$  m)



**Figure 3.31** Comparison test for Mode 3 - frequency 25 Hz ( $\theta = 90^\circ$ ,  $z = 36$  m)

We now initialize the field by a CW point source ( $f = 25$  Hz,  $z_s = 90$  m). Only the 3 propagating modes are selected. The initial field is given by Eq. (3.5) for  $m_p = 3$  (normalized modes). The reference sound speed is  $c_{ref} = 1500$  m/s.

We display in Fig. 3.32 the  $N \times 2D$  (upper plot) and 3D (lower plot) TL (in dB ref. 1m) horizontal slices ( $z = 36$  m), in Figs. 3.33 the corresponding TL vertical slices ( $\theta = 90^\circ$ ) and in Fig. 3.34 below the TL vs. range curves ( $\theta = 90^\circ$ ,  $z = 36$  m). We observe in the upper plot of Fig. 3.33 and Fig. 3.34 for  $0 \leq r \leq R$  the interference pattern due to the three propagating modes predicted by the  $N \times 2D$  model. As can be seen in Figs. 3.32, 3.33 and 3.34, the three-dimensional field is different. For  $r$  approximately less than 11 km, three modes are present, then, due to the *three-dimensional mode shadowing* effect of mode 3, only two modes are present for  $r$  greater than 11 km and until  $r \approx 18$  km where the *three-dimensional mode shadowing* effect of mode 2 becomes important. For  $r \geq 18$  km, only mode 1 is propagating, including its *three-dimensional mode self-interference effect* for  $r \geq 20$  km (fringe pattern). We also notice the differences in the  $N \times 2D$  and three-dimensional curves for  $r$  less than 11 km. Though three modes are present in this interval for both models,  $N \times 2D$  and three-dimensional modal propagation fields are different (cf. Figs. 3.29, 3.30, 3.31), the  $N \times 2D$  and three-dimensional interference patterns are hence also different.

We compare in Fig. 3.35 the solutions obtained with TRIPARADIM to the solutions obtained with FAWPE. We observe the same shifts in the phasing between the two solutions. Apart this shift, both solutions agree quite well.

SACLANTCEN SM-342

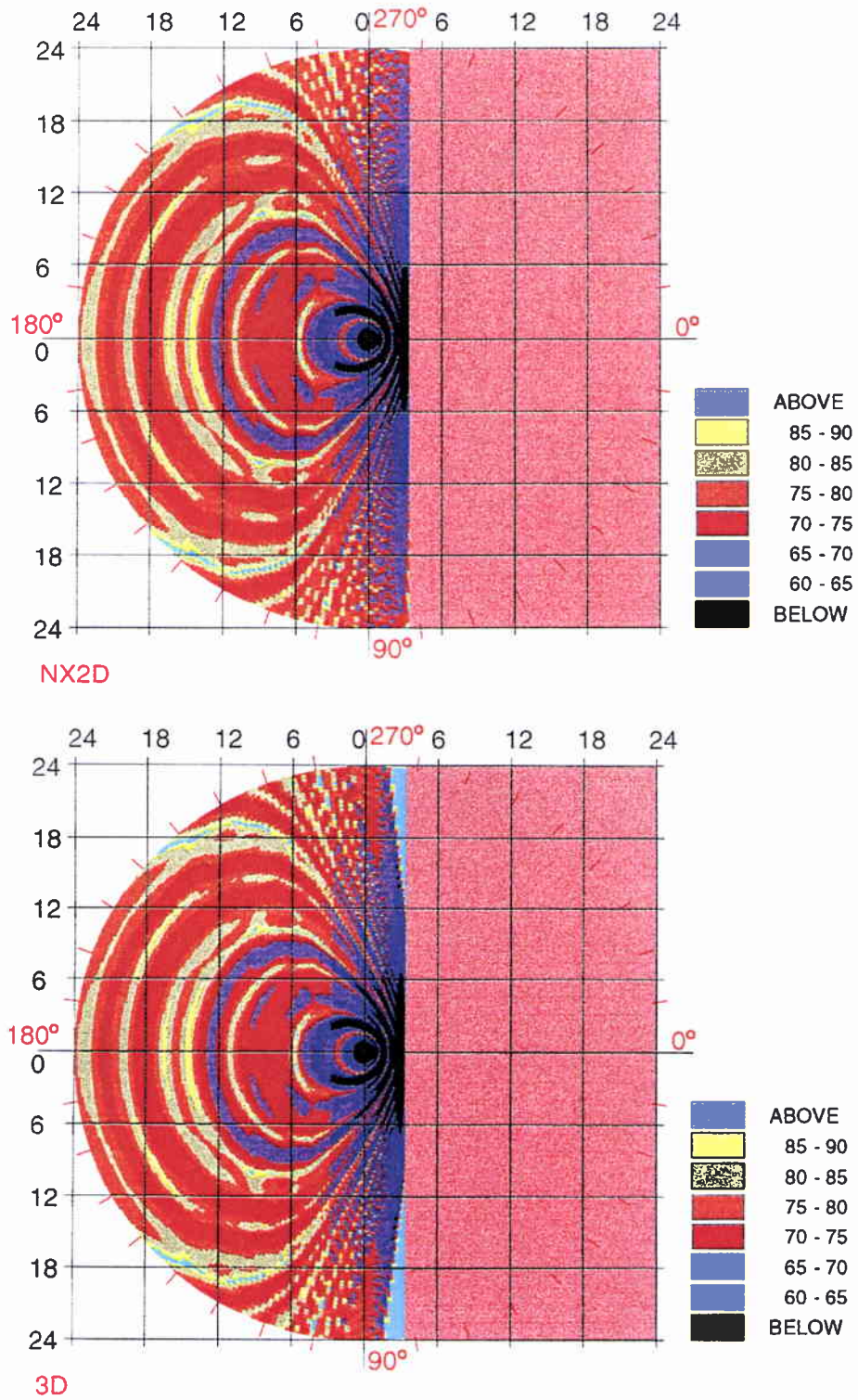


**Figure 3.32** CW point source (25 Hz), horizontal slices at constant depth  $z = 36$  m of the TL fields obtained using  $N \times 2D$  (upper figure) / three-dimensional (bottom figure) computations

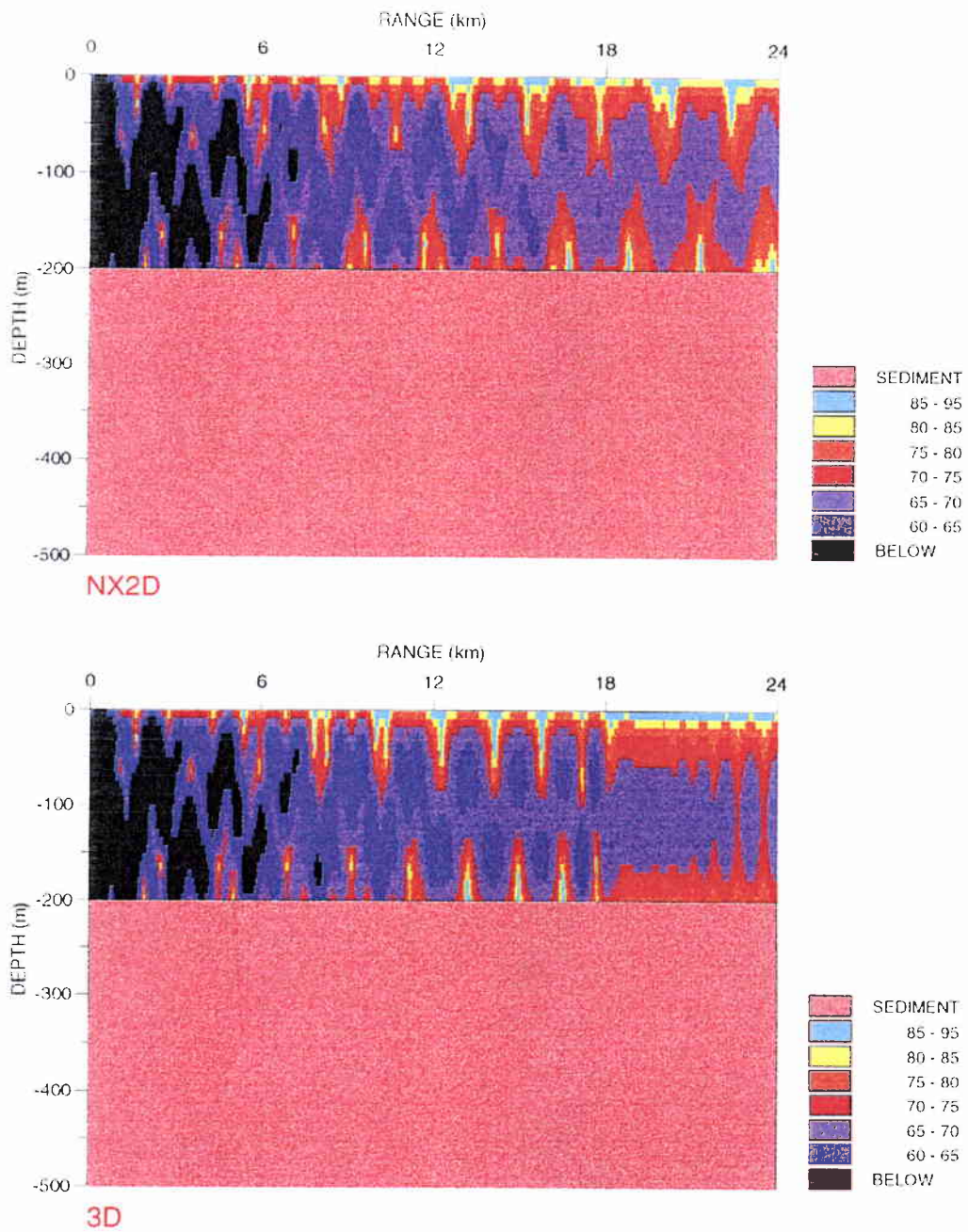


**Figure 3.33** CW point source (25 Hz), vertical slices at constant azimuth  $\theta = 90^\circ$  of the TL fields obtained using  $N \times 2D$  (upper figure) / three-dimensional (bottom figure) computations

SACLANTCEN SM-342

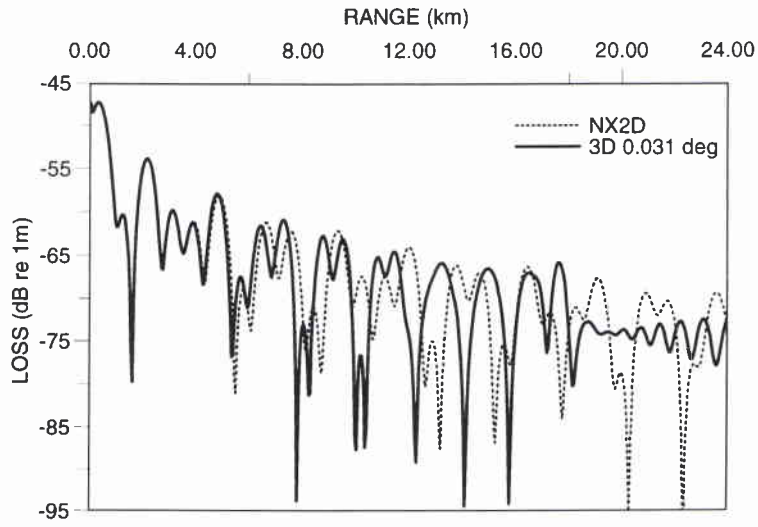


Figure 3.34 CW point source - frequency 25 Hz ( $\theta = 90^\circ$ ,  $z = 36$  m)

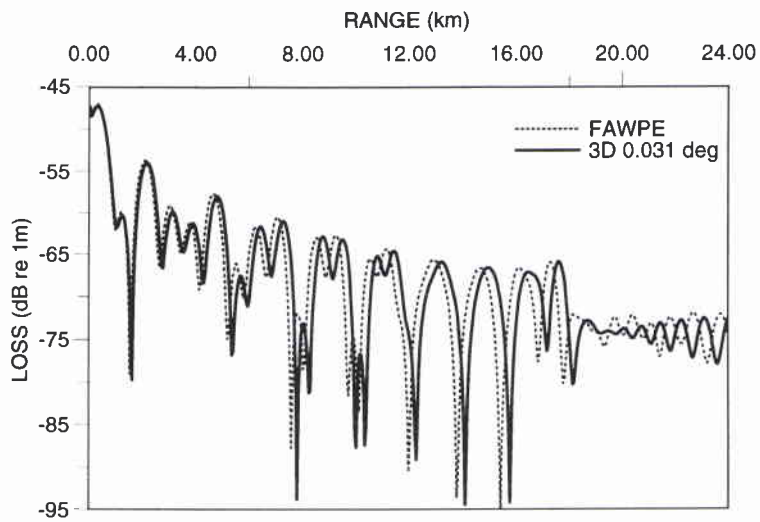


Figure 3.35 Comparison for CW point source - frequency 25 Hz ( $\theta = 90^\circ$ ,  $z = 36$  m)

## 4

## Numerical simulations of a three-dimensional rough boundary waveguide

### 4.1 Description of the problem

We now consider the penetrable rough boundary problem, originally proposed by Collins and Chin-Bing [5], consisting of an isovelocity water layer ( $\rho_0 = 1 \text{ g/cm}^3$ ,  $c_0 = 1500 \text{ m/s}$ ) overlying an attenuating homogeneous halfspace bottom ( $\rho_1 = 1.5 \text{ g/cm}^3$ ,  $c_1 = 1700 \text{ m/s}$ ,  $\alpha_1 = 0.5 \text{ dB}/\lambda$ ). The critical grazing angle is thus given by  $\vartheta_c = 28^\circ$ . The water column is assumed to be non attenuating and no shear energy is assumed in the sediment layer. The three-dimensional water/bottom surface parametrization writes

$$z_1(r, \theta) = 50(3 - \sin(2\pi r \cos \theta / \lambda_b)) \quad (4.1)$$

where  $\lambda_b = 6000 \text{ m}$ . The waveguide assumes symmetry in its geometry about the  $X_1$  axis (cf. Fig. 4.1). Eq. (4.1) simulates a corrugated bottom. A CW point source of frequency  $25 \text{ Hz}$  is placed at cartesian position vector  $X_s = (0, 0, 25 \text{ m})$  which corresponds in cylindrical coordinates to range  $r = 0$  and depth  $z = 25 \text{ m}$ .

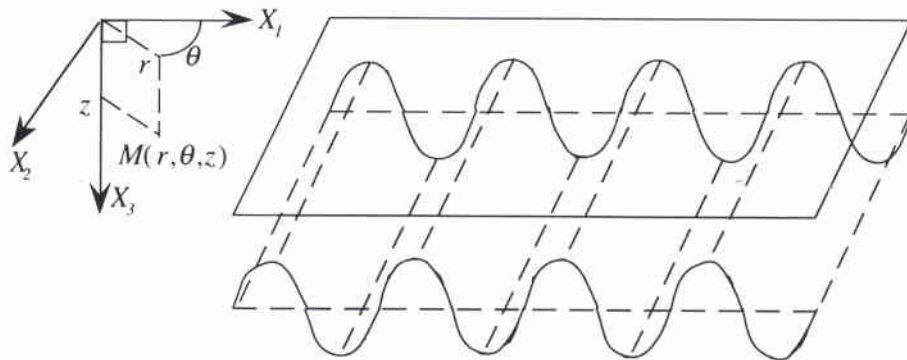


**Figure 4.1** Three-dimensional waveguide geometry of the rough boundary problem

For the particular azimuthal angles  $\theta = 0^\circ$  and  $\theta = 180^\circ$  (i.e., along the positive and negative  $X_1$  axis), the water/bottom interface is a sinusoid of periodicity  $\lambda_b$ : the minimum and maximum water depths being, respectively,  $100 \text{ m}$  and  $200 \text{ m}$  (cf. Fig. 4.2). Upslope and downslope propagations are handled for each azimuthal angle (for  $\theta = 90^\circ$  and  $\theta = 270^\circ$  the bottom is flat). For  $\theta$  varying from  $-90^\circ$  to  $90^\circ$ , an



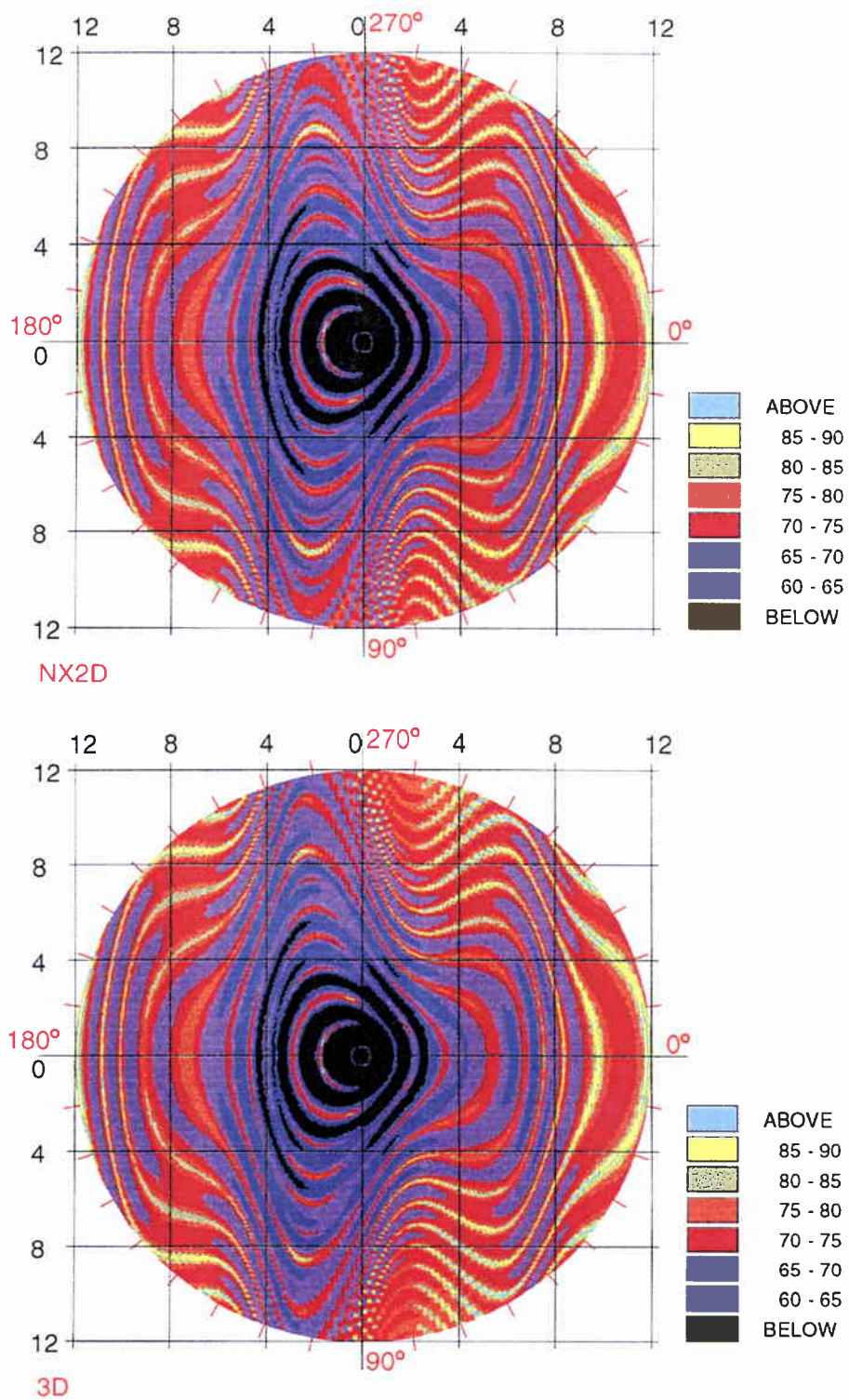


**Figure 4.3** CW point source, horizontal slices at constant depth  $z = 30$  m of the TL fields obtained using  $N \times 2D$  (upper figure) / three-dimensional (bottom figure) computations

SACLANTCEN SM-342

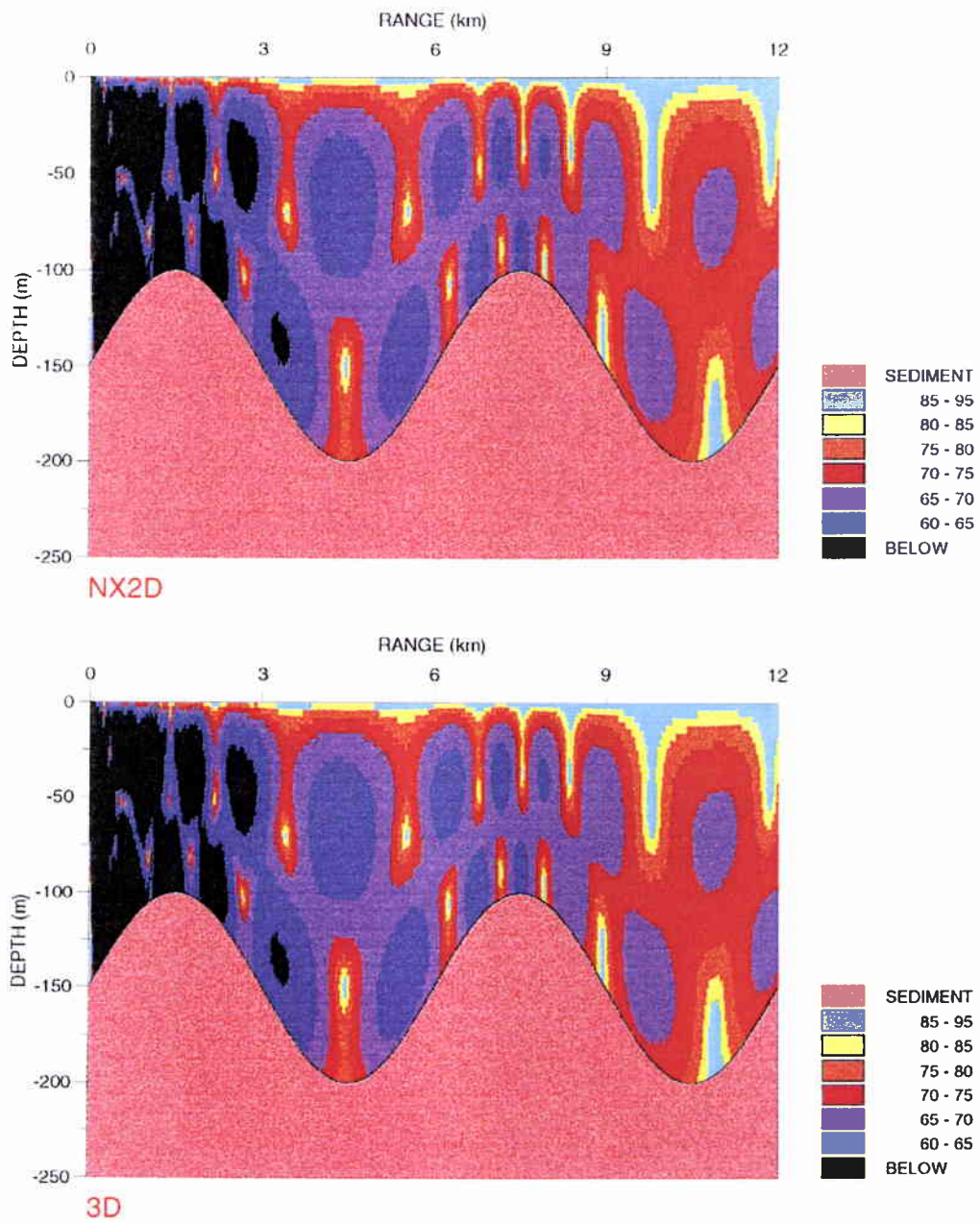


**Figure 4.4** CW point source, vertical slices at constant azimuth  $\theta = 0^\circ$  of the TL fields obtained using  $N \times 2D$  (upper figure) / three-dimensional (bottom figure) computation

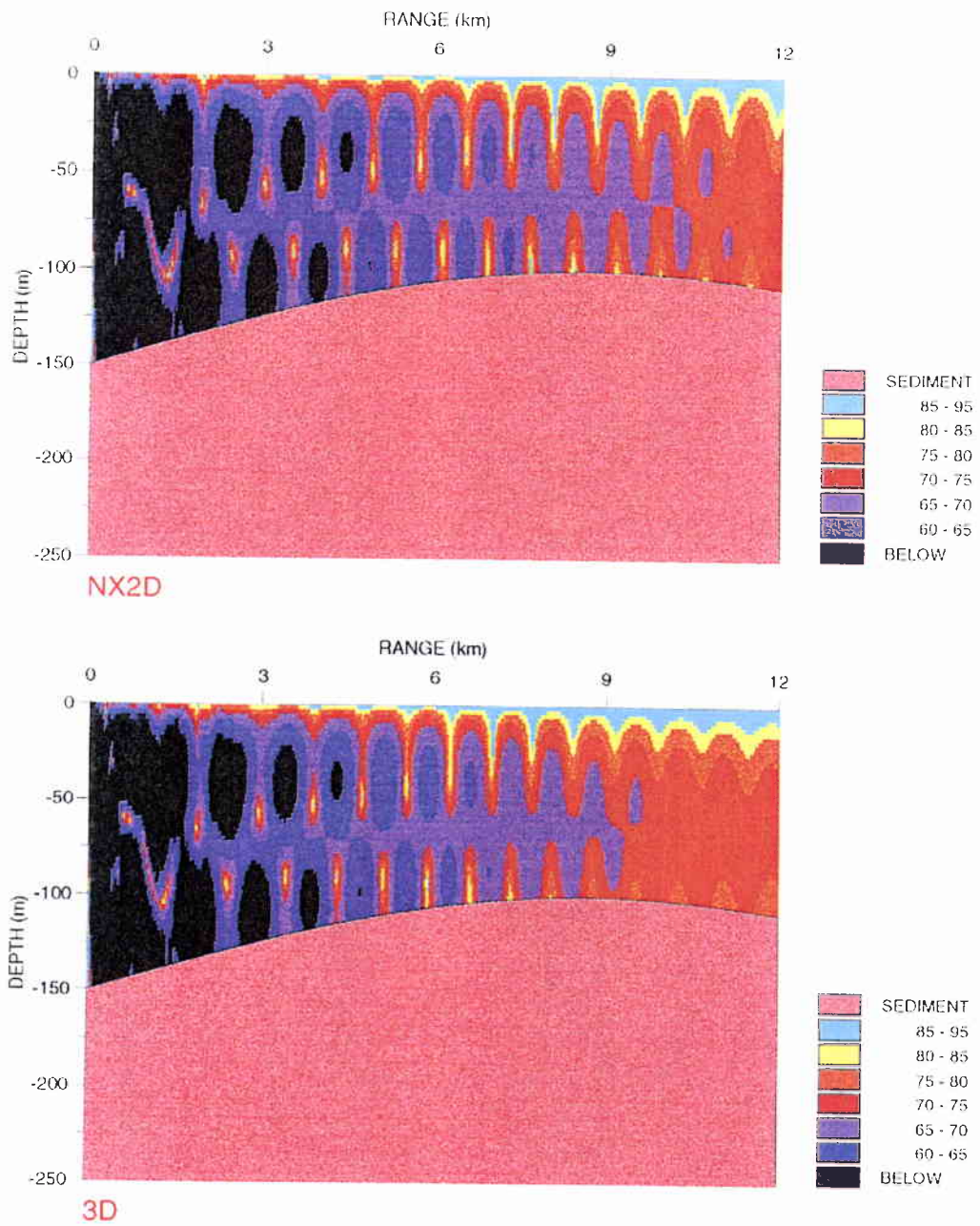


**Figure 4.5** CW point source, vertical slices at constant azimuth  $\theta = 80^\circ$  of the TL fields obtained using  $N \times 2D$  (upper figure) / three-dimensional (bottom figure) computation

SACLANTCEN SM-342

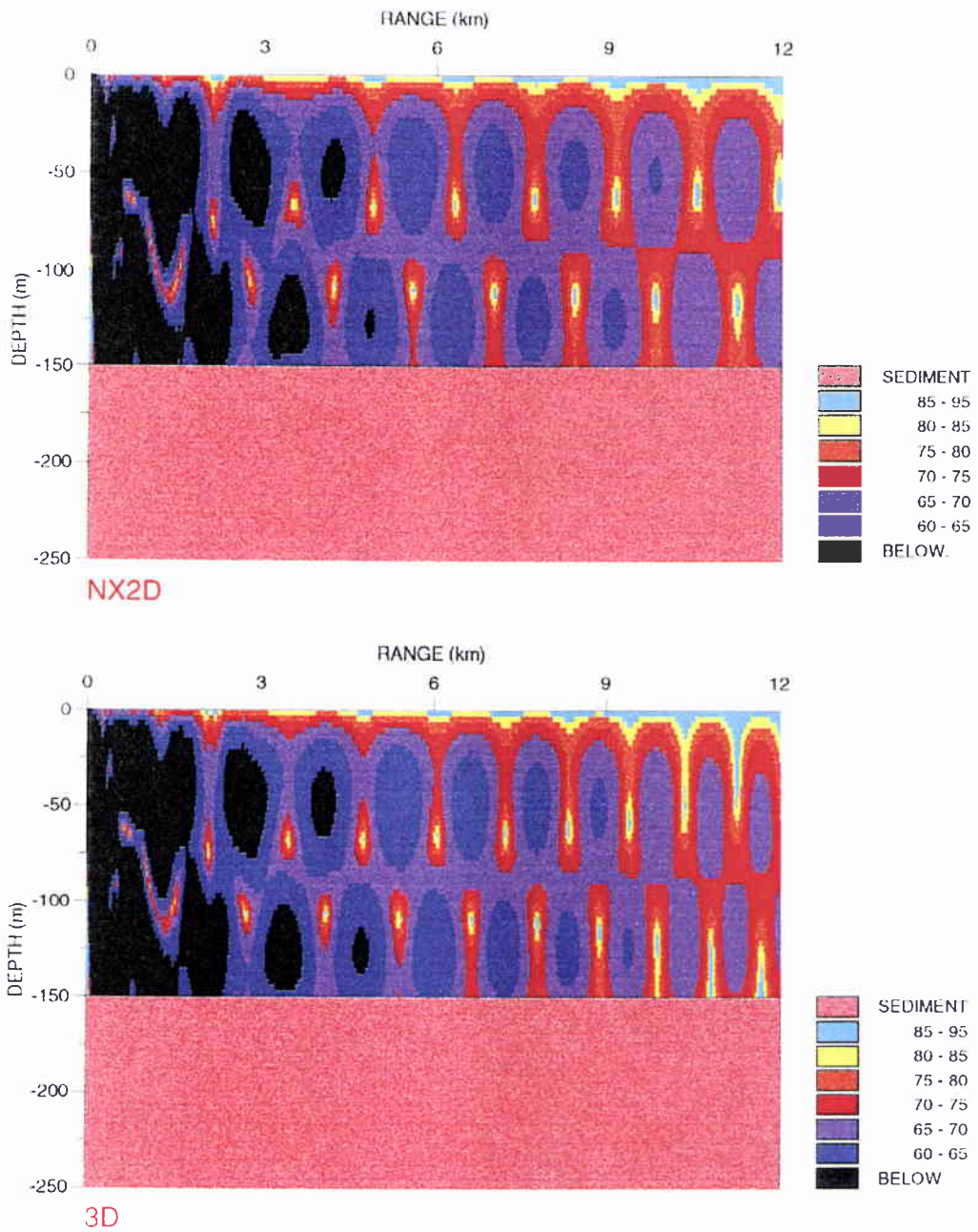


**Figure 4.6** CW point source, vertical slices at constant azimuth  $\theta = 90^\circ$  of the TL fields obtained using  $N \times 2D$  (upper figure) / three-dimensional (bottom figure) computation

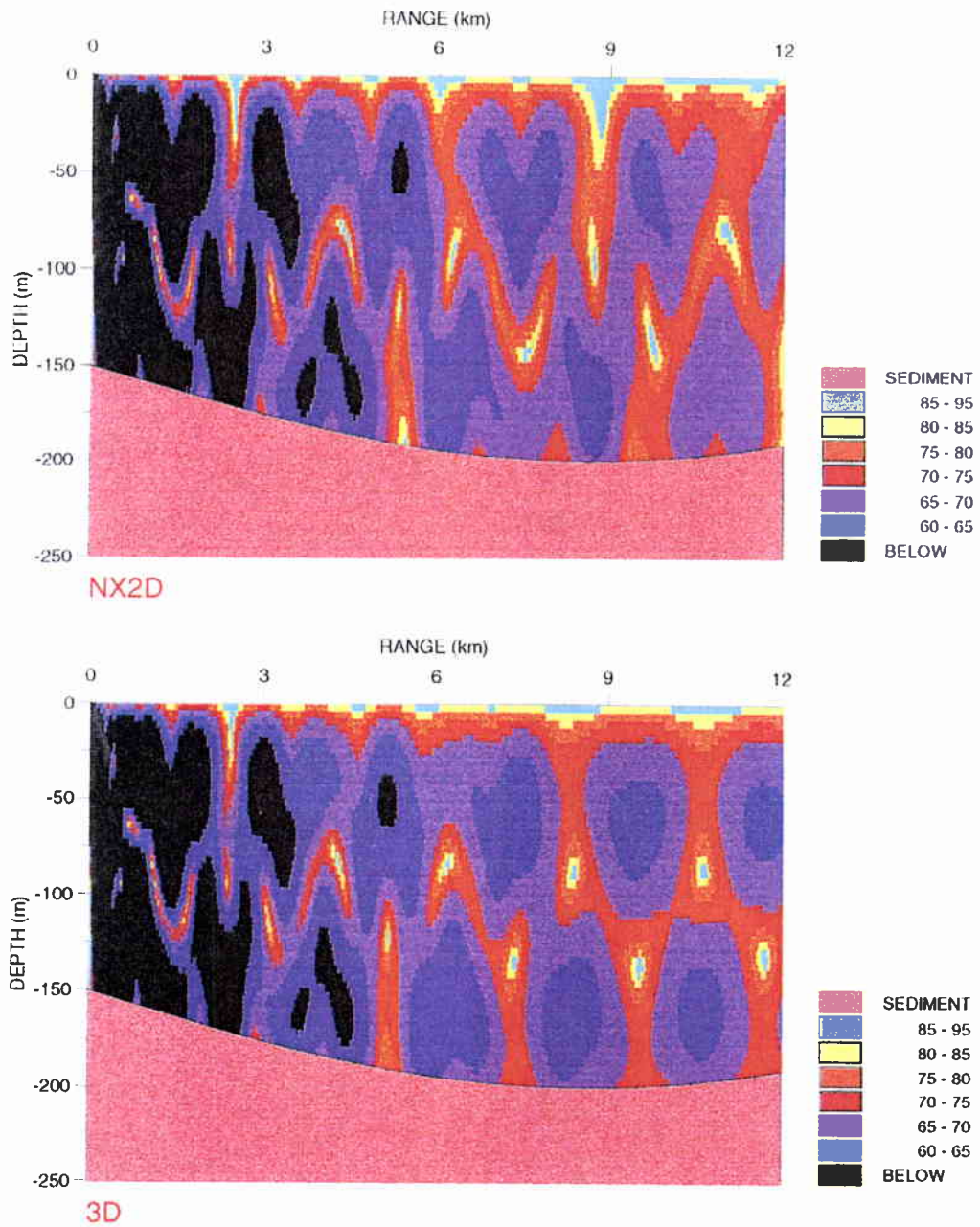


**Figure 4.7** CW point source, vertical slices at constant azimuth  $\theta = 100^\circ$  of the TL fields obtained using  $N \times 2D$  (upper figure) / three-dimensional (bottom figure) computation

SACLANTCEN SM-342

at both azimuthal angles  $\theta = 0^\circ$  and  $\theta = 180^\circ$ . The cylindrical symmetry of the geometry is thus locally valid for these particular azimuthal angles, thus leading to very good agreement between the  $N \times 2D$  and 3D solutions. We notice large differences between the  $N \times 2D$  and 3D fields for other azimuthal angles  $\theta = 80^\circ$ ,  $\theta = 90^\circ$  and  $\theta = 100^\circ$ . The reason is that energy gets trapped in the deep part of the corrugated bottom and channeled in the  $X_2$  direction, leading to significant horizontal refraction of the propagating sound.

The water depth  $z_1$  given by Eq. (4.1) and being constant in the  $X_2$  direction is equal to 150 m in the vertical plane corresponding to  $\theta = 90^\circ$ , the CW point source emission leading to two propagating modes in that vertical plane (cf. upper plot of Fig. 4.6). The interference pattern due to these two propagating modes changes due to the horizontal refraction of each mode. We notice also in  $N \times 2D$  field shown on Fig. 4.7 (upper plot) the presence of three propagating modes for the 200m-depth waveguide at range  $r \approx 9$  km and at  $\theta = 100^\circ$ : only two modes are present at the same range and azimuthal angle in the 3D field.

### Convergence tests

The three-dimensional field has been obtained using in the mapped computation domain  $N = 260$  discrete points in depth ( $\Delta y = 1/260$ ),  $M = 2880$  discrete points in azimuth ( $\Delta \theta = 0.125^\circ$ ) and  $\Delta r = 10$  m. The increment  $\Delta y$  corresponds in the physical waveguide to  $4 \text{ m} \leq \Delta z(r, \theta) \leq 1 \text{ m}$  and for  $\theta = 90^\circ$  to  $\Delta z(r, \theta = 90^\circ) \approx 2 \text{ m}$ . We show in the following figures the solutions obtained with three-dimensional computations for different numbers of discrete points in azimuth and for different azimuthal angles:  $\theta = 80^\circ$  (Fig. 4.8),  $\theta = 90^\circ$  (Fig. 4.9),  $\theta = 100^\circ$  (Fig. 4.10). All the three plots correspond to receiver depth  $z = 30 \text{ m}$ .

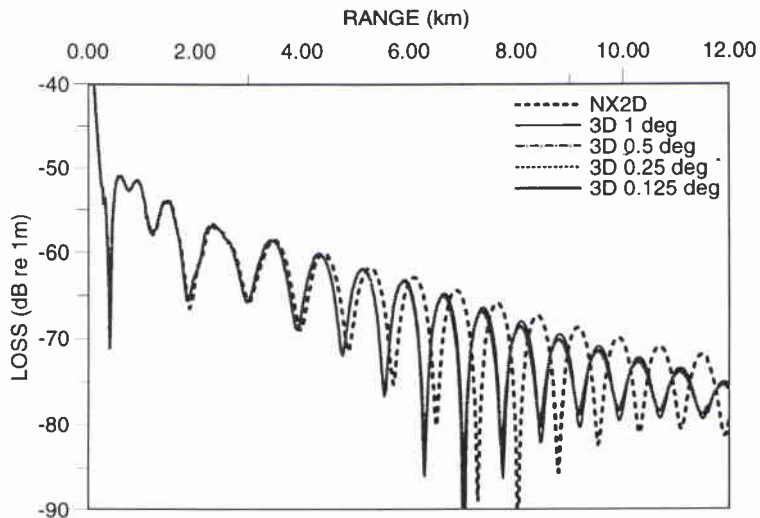
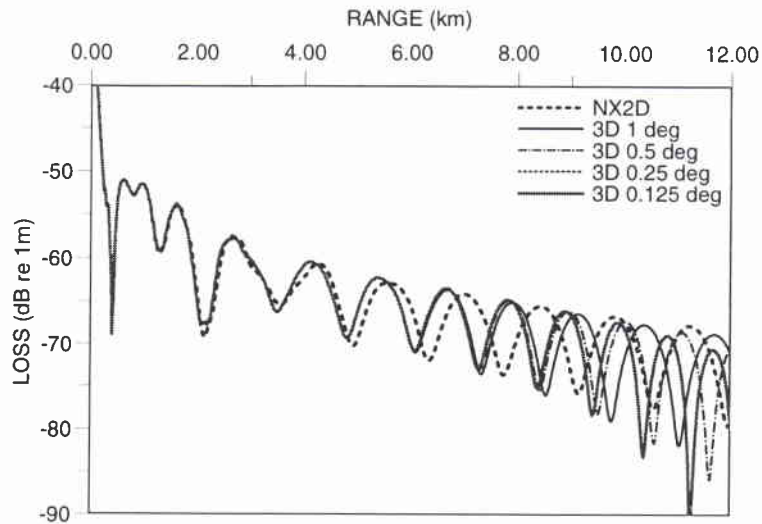
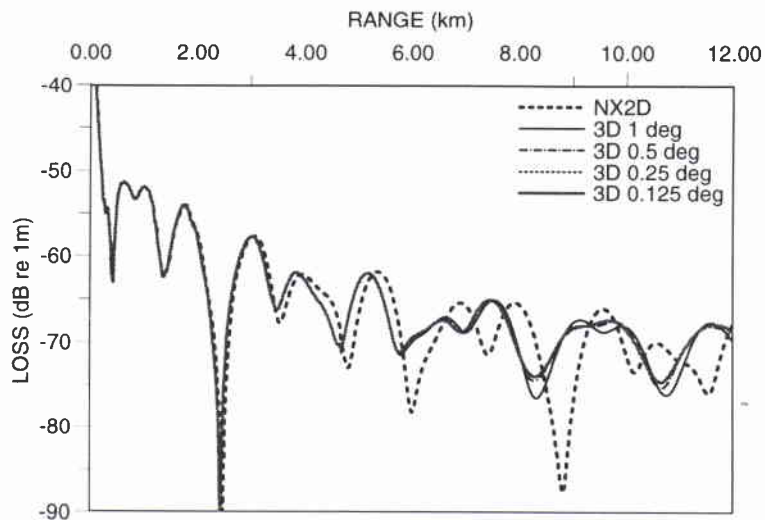


Figure 4.8 Convergence test ( $\theta = 80^\circ$ ,  $z = 30 \text{ m}$ )



**Figure 4.9** Convergence test ( $\theta = 90^\circ$ ,  $z = 30\text{ m}$ )



**Figure 4.10** Convergence test ( $\theta = 100^\circ$ ,  $z = 30\text{ m}$ )

The azimuthal increment  $\Delta\theta = 0.125^\circ$  ( $M = 2880$ ) used in the three-dimensional computation corresponds at maximum range  $R = 12\text{ km}$  to  $\Delta S(R, \Delta\theta = 0.125^\circ) \approx \lambda/2$ . Convergence is reached for this azimuthal increment. We observe in Figs. 4.8, 4.9, 4.10 that the solution obtained using  $\Delta\theta = 0.25^\circ$  ( $M = 1440$ ) is very close to the converged solution and thus sufficient to describe the three-dimensional effects in the vertical planes corresponding to  $\theta = 80^\circ$ ,  $\theta = 90^\circ$  and  $\theta = 100^\circ$ . Selecting larger azimuthal increments in the three-dimensional

SACLANTCEN SM-342

computation leads to accurate solutions in some particular azimuthal angles (cf. Figs. 4.8 and 4.10) but is inaccurate for other azimuthal angles (cf. Fig. 4.9).

### Investigation of various bottom periodicities

We now consider the bottom geometry given by Eq. (4.1) for various  $\lambda_b$ :  $\lambda_b = 5000$  m,  $\lambda_b = 4500$  m and  $\lambda_b = 4000$  m. We denote by  $\alpha$  the maximum slope angle in the  $X_1$  direction. Decreasing  $\lambda_b$  corresponds to increasing the slope angle  $\alpha$ . Thus we expect to have increasing three-dimensional horizontal refraction of the propagating energy when decreasing  $\lambda_b$  in the rough boundary. We focus on the specific azimuthal angle  $\theta = 90^\circ$  for which the bathymetry assumes no slope.

We show in Fig. 4.11 three-dimensional computations (bold solid lines) obtained for  $\lambda_b = 6000$  m ( $\alpha \approx 2.99^\circ$ ),  $\lambda_b = 5000$  m ( $\alpha \approx 3.59^\circ$ ),  $\lambda_b = 4500$  m ( $\alpha \approx 3.99^\circ$ ) and  $\lambda_b = 4000$  m ( $\alpha = 4.49^\circ$ ). We also display in each plot the corresponding  $N \times 2D$  solutions. We observe that  $N \times 2D$  solutions are identical for each case regardless of the (crossing) slope in the bottom geometry. We observe also increasing three-dimensional effects in both phasing and amplitude for increasing (crossing) slopes.

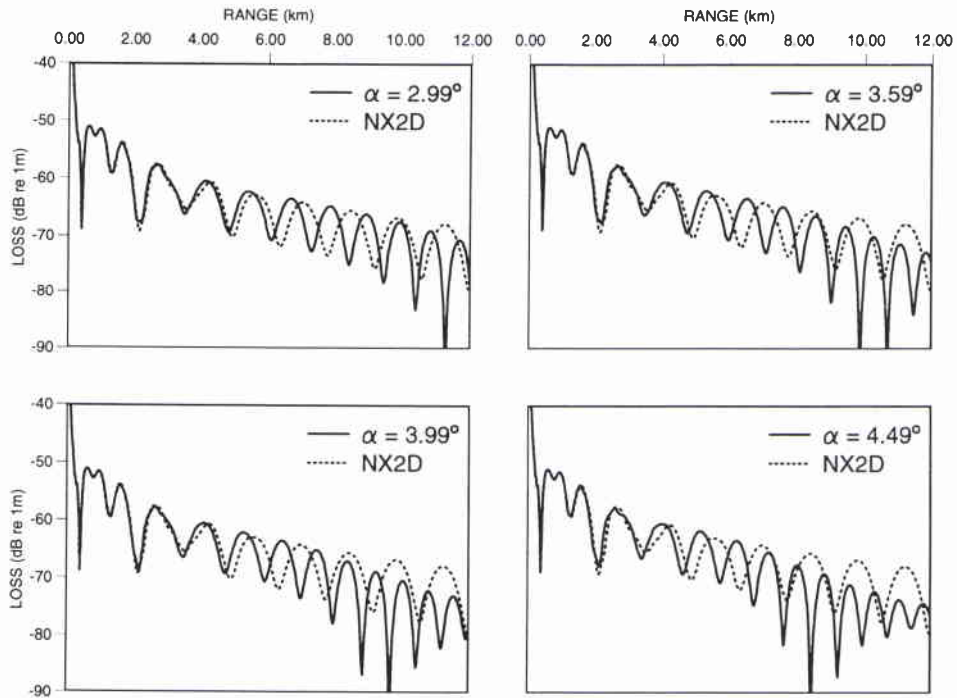


**Figure 4.11** Investigation of various bottom periodicities ( $\theta = 90^\circ$ ,  $z = 30$  m). The parameter  $\alpha$  designs the bottom slope in the  $X_1$  direction. In the four subplots,  $N \times 2D$  (dotted line) and three-dimensional (bold solid line) are displayed.

### Comparison with FAWPE

We now compare the solution obtained with TRIPARADIM to the solution obtained with FAWPE. The range increment  $\Delta r$  is identical for the two models. The depth increment  $\Delta z$  used in FAWPE is given by  $\Delta z = 2$  m and is constant in all the waveguide. The depth increment is thus identical for both models for  $\theta = 90^\circ$ . FAWPE requires 1024 azimuthal FFT components to get an accurate solution.

We show in the following figures the solutions obtained with the two models and for different azimuthal angles:  $\theta = 80^\circ$  (Fig. 4.12),  $\theta = 90^\circ$  (Fig. 4.13),  $\theta = 100^\circ$  (Fig. 4.14). Apart the slight shift in the phasing observed in Figs. 4.13 and 4.14, the two solutions agree closely.

If one compares the curves obtained for the  $\lambda_b = 6000$  m case with the curves obtained by Collins and Chin-Bing [5], it can be seen that although the curves are similar there are noticeable differences. We attribute this to the fact that the two three-dimensional PE codes of this memorandum utilize a narrow-angle approximation and source for these examples (we have run FAWPE in the narrow-angle mode for comparison with TRIPARADIM) while three-dimensional PE used a wide-angle approximation.

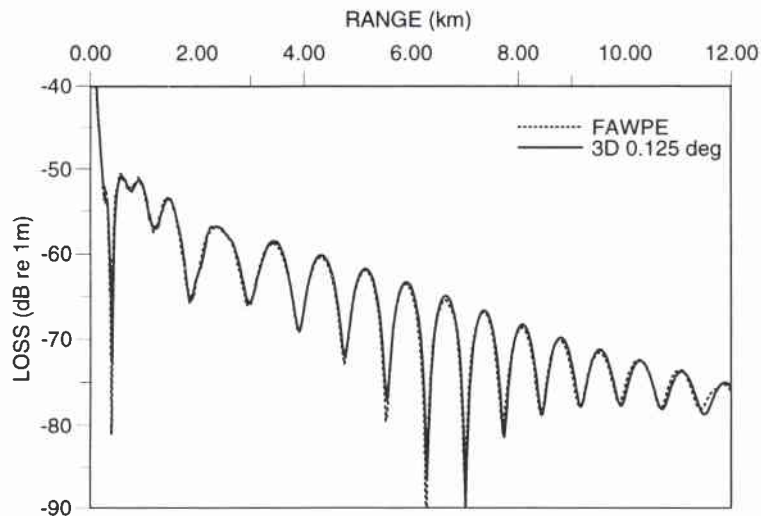


**Figure 4.12** Comparison test ( $\theta = 80^\circ$ ,  $z = 30$  m)

SACLANTCEN SM-342

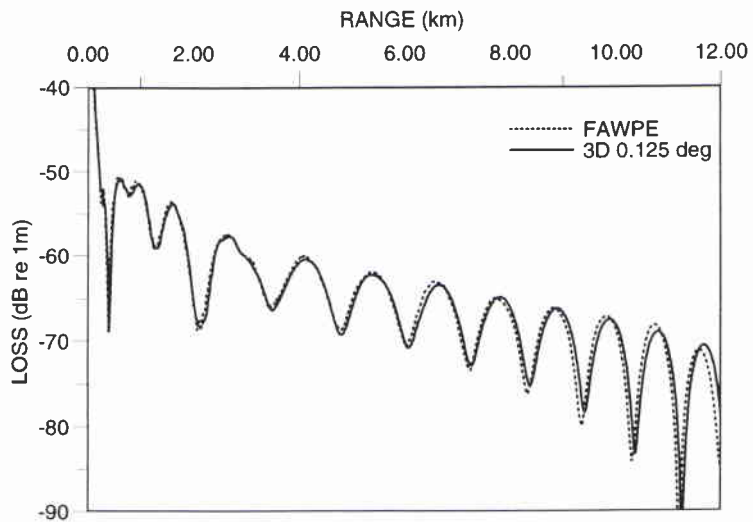


Figure 4.13 Comparison test ( $\theta = 90^\circ, z = 30\text{ m}$ )

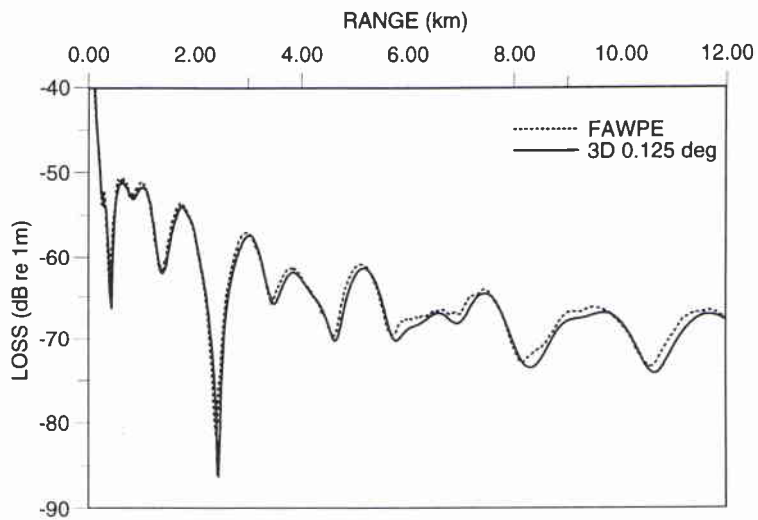


Figure 4.1 Comparison test ( $\theta = 100^\circ, z = 30\text{ m}$ )

# 5

## Summary

---

In this report, we have investigated the performance of two very different three-dimensional PE codes on two main types of benchmark cases; the ASA benchmark wedge [17], for different frequencies and source excitations, and the corrugated bottom of Collins and Chin-Bing [5]. We found that the two methods showed good agreement with each other. In the case of the corrugated bottom, the two codes of this report which used a narrow-angle approximation gave results which differed somewhat from those of Collins and Chin-Bing [5] who used a wide-angle approximation.

The examples considered, showed that for regions of the waveguide, full three-dimensional effects are significant. In terms of modal energy, regions of modal shadow zones and modal self-interference were evident. These effects occurred for 5, 15, and 25 Hz. For the wedge examples, if we considered the modes with a similar corresponding ray angle (mode 1 for 5 Hz, mode 2 for 15 Hz, and mode 3 for 25 Hz) for the three frequencies, we find that their three-dimensional behaviour is similar.

In the case of the corrugated bottom, there are also significant three-dimensional effects and it is possible for modal energy to become “trapped” in the channels of this waveguide.

It is reassuring that two very different implementations of three-dimensional PE codes give similar results for a variety of sample codes. We hope that in the future more researchers will compare the results of their three-dimensional PE codes for benchmark cases. The waveguides of this report could be used as such benchmark cases.

## References

- [1] Sturm, F., Pélissier, M.C., Fattaccioli, D. 3D Sound Propagation Modelling with TRIPARADIM. In Proceedings of the 3rd European Conference on Underwater Acoustics, Heraklion, Crete, Greece (24-28 June 1996).
- [2] Sturm, F., Pélissier, M.C., Fattaccioli, D. Development of an acoustic field predictor in a three dimensional oceanic environment, in *Proceedings of Full Field Inversion Methods In Ocean And Seismic Acoustics*, A Nato Conference, Lercini ITALY (27 June - 1 July 1994).
- [3] Fawcett, J.A. Modeling three-dimensional propagation in an oceanic wedge using parabolic equation methods, *Journal of the Acoustical Society of America*, **93**, 1993:2627-2632.
- [4] Baer, R.N. Propagation through a three-dimensional eddy including effects on an array, *Journal of the Acoustical Society of America*, **69**, 1981:70-75.
- [5] Collins, M.D., Chin-Bing, S.A. A three-dimensional parabolic equation model that includes the effects of rough boundaries, *Journal of the Acoustical Society of America*, **87**, 1990:1104-1109.
- [6] Siegmann, W.L. Kriegsmann, G.A., Lee, D. A wide-angle three-dimensional parabolic wave equation, *Journal of the Acoustical Society of America*, **78**, 1985:659-664.
- [7] Lee, D., Botseas, G., Siegmann, W.L. Examination of three-dimensional effects using a propagation model with azimuth-coupling capability (FOR3D), *Journal of the Acoustical Society of America*, **91**, 1992:3192-3202.
- [8] Bergmann, P.G. The wave equation in a medium with a variable index of refraction, *Journal of the Acoustical Society of America*, **17**, 1946:329-333.
- [9] Brock, H.K. The AESD Parabolic Equation Model, Rep. TN-12, Naval Ocean Research and Development Activity, Stennis Space Center, MS (1978)
- [10] Abrahamsson, L., Kreiss, H.O. Boundary conditions for the parabolic equation in a range dependent duct, *Journal of the Acoustical Society of America*, **87**, 1990:2438-2441.
- [11] Bamberger, A., Engquist, B., Halpern, L., Joly, P. Higher order parabolic wave equation approximations in heterogeneous media, *SIAM Journal of Applied Mathematics*, **48**, 1988:129-154.
- [12] Collins, M.D. Application and time-domain solution of higher-order parabolic equation in underwater acoustics, *Journal of the Acoustical Society of America*, **86**, 1989:1097-1102.
- [14] Claerbout, J.F. Fundamentals of geophysical data processing, McGraw-Hill, New-York (1976)
- [15] Jensen, F.B., Ferla, M.C. Numerical solutions of range-dependent benchmark problems in ocean acoustics, *Journal of the Acoustical Society of America*, **87**, 1990:1499-1513.
- [16] Jensen, F.B., Ferla, M.C. SNAP: the SACLANTCEN normal-mode acoustic propagation model, Rep. SM-121, SACLANT Undersea Research Centre, La spezia, Italy (1979)
- [17] Jensen, F.B., Kuperman, W.A. Sound propagation in a wedge-shaped ocean with penetrable bottom, *Journal of the Acoustical Society of America*, **67**, 1980:1564-1566.
- [18] Varga, R.S., Matrix iterative analysis, Prentice-Hall, Englewood Cliffs, NJ, (1962).
- [19] Bayliss, A., Goldstein, C.I., Turkel, E. The numerical solution of the Helmholtz equation for wave propagation problems in underwater acoustics. *Computational Mathematics with Applications*, **11**, 1985:655-665.

## Annex A

### Accurate treatment of three-dimensional sloping bottoms with TRIPARADIM

---

#### A.1 Using of an affine mapping

We intend to solve the initial and boundary value problem presented in Section 2.2 involving Eq. (2.8) and appropriate initial and boundary conditions, in a general three-dimensional environment. We thus don't want to impose any cylindrical symmetry on the sloping bottom (which is the case for bidimensional models) or any stair-step approximation (which is assumed by all the three-dimensional PE models derived at this time). One way of handling this difficulty is to transform the physical domain into a simpler one using an affine mapping [1], [11]. Setting

$$y = z/s(r, \theta) \quad (\text{A.1})$$

for  $r_0 \leq r \leq R$  and  $0 \leq \theta < 2\pi$ , where  $s(r, \theta) := z_{\max}(r, \theta)$ , we send the variable interval  $[0, z_{\max}(r, \theta)]$  onto the reference interval  $[0, 1]$ . Hence, the new domain to which we will refer in this memorandum as the mapped computation domain, is defined by the variables  $r, \theta, y$ . The horizontal range  $r$  varies from  $r_0$  to  $R$ , the azimuth angle  $\theta$  from 0 to  $2\pi$  and the dimensionless new 'depth'  $y$  from 0 to 1. In the physical domain, we consider homothetical sedimental layers  $\Sigma_q$ ,  $1 \leq q \leq Q$ , *i.e.*, under the assumption that  $0 < S_1 < \dots < S_Q < 1$ , the interfaces parametrizations write

$$z - S_q s(r, \theta) = 0, \quad 1 \leq q \leq Q. \quad (\text{A.2})$$

We therefore obtain the following interface parametrizations in the mapped domain

$$y - S_q = 0, \quad 1 \leq q \leq Q. \quad (\text{A.3})$$

The mapped computation domain is bounded in 'depth' by two horizontal surfaces at  $y=0$  and  $y=1$ , the sedimental interfaces corresponding to the horizontal surfaces at  $y = S_q$ ,  $1 \leq q \leq Q$  (cf. Fig. A.1). Introducing the new unknown  $u$

$$u(r, \theta, y) = v(r, \theta, s(r, \theta)y) \quad (\text{A.4})$$

Eq. (2.8) writes in the new coordinates as

$$\frac{\partial u}{\partial r} = \frac{i\rho}{2k_{ref}} \left( \frac{1}{s^2} \frac{\partial}{\partial y} \left( \frac{1}{\rho} \frac{\partial u}{\partial y} \right) + \frac{1}{r^2} L_{\theta} \left( \frac{1}{\rho} L_{\theta} u \right) \right) + \frac{ik_{ref}}{2} (\tilde{n}_\alpha^2 - 1)u + \left( \frac{y}{s} \frac{\partial s}{\partial r} \right) \frac{\partial u}{\partial y} \quad (\text{A.5})$$

where  $\tilde{n}_\alpha(r, \theta, y) = n_\alpha(r, \theta, s(r, \theta)y)$  and where the operator  $L_{\theta}$  is defined by

SACLANTCEN SM-342

$$L_{\theta_s} u = \frac{\partial u}{\partial \theta} - \left( \frac{y}{s} \frac{\partial s}{\partial \theta} \right) \frac{\partial u}{\partial y}$$

The characteristics of the bottom geometries are now consequently included in the variable coefficients of Eq. (A.5) which therefore contains new derivative terms. The new unknown  $u$  is assumed to satisfy in the mapped computation domain the following conditions :  $u=0$  at  $y=0$ , a  $2\pi$ -periodicity condition  $u(r,0,y)=u(r,2\pi,y)$ , an initial condition  $u(r_0, \theta, y) = v^0(\theta, s(r, \theta)y)$  at  $r=r_0$ , a parabolized bottom condition

$$\frac{1}{s} \frac{\partial u}{\partial y} - i k_{ref} \frac{\partial s}{\partial r} u - \frac{1}{r^2} \frac{\partial s}{\partial \theta} L_{\theta_s} u = 0 \quad (\text{A.6})$$

at  $y=1$ ,  $u_{q-1}(r, \theta, S_q) = u_q(r, \theta, S_q)$ ,  $1 \leq q \leq Q$ , and the parabolized conditions

$$\frac{1}{\rho_{q-1}} \frac{\partial u_{q-1}}{\partial \tilde{T}_q}(r, \theta, S_q) = \frac{1}{\rho_q} \frac{\partial u_q}{\partial \tilde{T}_q}(r, \theta, S_q) \quad (\text{A.7})$$

at  $y=S_q$ ,  $1 \leq q \leq Q$ , where operators  $\partial/\partial \tilde{T}_q$ ,  $1 \leq q \leq Q$ , are defined by

$$\frac{\partial}{\partial \tilde{T}_q} := \frac{1}{s} \frac{\partial}{\partial y} - i k_{ref} S_q \frac{\partial s}{\partial r} \mathbf{I} - \frac{S_q}{r^2} \frac{\partial s}{\partial \theta} L_{\theta_s}$$

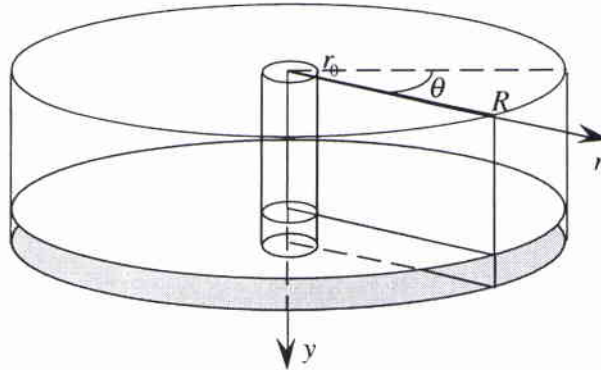


**Figure A.1** Three-dimensional cylinder geometry of the mapped computation waveguide for  $r_0 \leq r \leq R$ ,  $0 \leq \theta < 2\pi$ ,  $0 \leq y \leq 1$ . This new domain is the image of the physical domain shown in Fig. 2.1 by the affine mapping defined by Eq. (A.1). The horizontal mapped rigid bottom parametrization is given by  $y=1$ . The physical sedimental interface (sea-floor) is assumed to be homothetical, i.e., its parametrization is given by  $z=S_q s(r, \theta)$  with  $0 < S_q < 1$  and is thus transformed into a flat horizontal mapped sedimental interface of parametrization  $y=S_q$ .

### A.2 Numerical discretization

Implicit finite difference methods for the discretization of the initial and boundary value problem presented in the previous subsection are derived in [1] and [11]. We now discretize the continuous problem in the depth and azimuthal variables using finite element technique ( $C^1$ -polynomial standard Galerkin/finite element method) coupled with a conservative Crank-Nicolson type range-stepping procedure.

### Variational formulation

We first derive the variational formulation of the continuous problem. For the sake of simplicity, we introduce the new unknown  $w$  defined by

$$w(r, \theta, y) = \sqrt{s} u(r, \theta, y) \quad (\text{A.8})$$

Then, multiplying Eq. (A.5) by  $\sqrt{s} \bar{\varphi} / \rho$  where  $\varphi \in V$  are arbitrary appropriate complex-valued functions defined on  $\Omega = [0, 2\pi] \times [0, 1]$  (the functional space  $V$  is defined by  $V = \{\varphi \in H^1(\Omega) \text{ and } \varphi|_{y=0} = 0\}$  where  $H^1(\Omega)$  denotes the classical sobolev-space), integrating by parts using Eqs. (A.6) and (A.7), we obtain the following variational formulation

$$\frac{d}{dr}(w(r), \varphi)_\rho + i \alpha(r; w(r), \varphi) = 0, \quad \forall \varphi \in V \quad (\text{A.9})$$

$$w(r_0) = w^0$$

where  $w^0 \in V$  is defined by  $w^0(\theta, y) = \sqrt{s(r_0, \theta)} v^0(\theta, s(r_0, \theta), y)$  and where  $(\dots)_\rho$  designates the weighted complex-valued inner product defined by

$$(w, \varphi)_\rho := \int_{\Omega} w \bar{\varphi} \frac{d\Omega}{\rho}$$

(we denote by  $\|\cdot\|_\rho$  the corresponding norm, *i.e.*,  $\|\cdot\|_\rho = \sqrt{(\dots)_\rho}$ ) and where  $\alpha(r; \dots)$ ,  $r_0 \leq r \leq R$ , designates the complex-valued sesquilinear forms defined by

$$\alpha(r; w, \varphi) = \alpha_{N \times 2D}(r; w, \varphi) + \alpha_\theta(r; w, \varphi) \quad (\text{A.10})$$

with

$$\begin{aligned} \alpha_{N \times 2D}(r; w, \varphi) = & \frac{1}{2k_{ref}} \int_{\Omega} \frac{1}{s^2} \frac{\partial w}{\partial y} \frac{\partial \bar{\varphi}}{\partial y} \frac{d\Omega}{\rho} - \int_{\Omega} \frac{k_{ref}}{2} (\tilde{n}_\alpha^2 - 1) w \bar{\varphi} \frac{d\Omega}{\rho} \\ & + \frac{i}{2} \int_{\Omega} \frac{y}{s} \frac{\partial s}{\partial r} \left( \frac{\partial w}{\partial y} \bar{\varphi} - w \frac{\partial \bar{\varphi}}{\partial y} \right) \frac{d\Omega}{\rho} \end{aligned} \quad (\text{A.11})$$

$$\alpha_\theta(r; w, \varphi) = \frac{1}{2k_{ref}} \int_{\Omega} \frac{1}{r^2} \mathbf{L}_\theta w \mathbf{L}_\theta \bar{\varphi} \frac{d\Omega}{\rho} \quad (\text{A.12})$$

SACLANTCEN SM-342

where the operator  $\mathbf{L}_\theta$  is defined by

$$\mathbf{L}_\theta \varphi = \sqrt{s} L_\theta (\varphi / \sqrt{s})$$

All the coupling terms in the azimuthal direction are included in the forms  $\alpha_\theta(r; \dots)$ ,  $r_0 \leq r \leq R$ , given by Eq. (A.12). The forms  $\alpha(r; \dots)$  given by Eq. (A.10) are written in a convenient manner. It allows us to distinguish between the part relative to the  $N \times 2D$  model (*i.e.*, the forms  $\alpha_{N \times 2D}(r; \dots)$ ,  $r_0 \leq r \leq R$ ), and the part proper to the three-dimensional model (*i.e.*, the forms  $\alpha_\theta(r; \dots)$ ,  $r_0 \leq r \leq R$ ). Selecting  $\varphi = w(r)$  in the variational formulation, Eq. (A.9), we may show the  $\|\cdot\|_\rho$ -stability condition which writes

$$\frac{d}{dr} \int_\Omega |w(r, \theta, y)|^2 \frac{d\Omega}{\rho} \leq 0, \quad r_0 \leq r \leq R \quad (\text{A.13})$$

Eq. (A.13) holds as an equality (*i.e.*, the problem is  $\|\cdot\|_\rho$ -conserving) if the attenuation term is null. Using Eqs. (A.4), (A.8), it is easy to see that Eq. (A.13) corresponds in the mapped domain to the stability condition, Eq. (2.12), in the physical domain.

### Fully discrete scheme

For integers  $N$  and  $M$ , we let  $\{y_0, y_1, \dots, y_N\}$  be a uniform partition of  $[0, 1]$ , *i.e.*,  $y_j = j\Delta y$ , where  $\Delta y = 1/N$ , and  $\{\theta_0, \theta_1, \dots, \theta_M\}$  be a uniform partition of  $[0, 2\pi]$ , *i.e.*,  $\theta_i = i\Delta\theta$ , where  $\Delta\theta = 2\pi/M$ , such that  $\theta_0 = 0$ ,  $\theta_M = 2\pi$ ,  $y_0 = 0$ ,  $y_N = 1$ . We let  $h = \max\{\Delta\theta, \Delta y\}$ . We denote by  $\Delta z$  the corresponding depth increment in the physical domain, defined by

$$\Delta z(r, \theta) = s(r, \theta)\Delta y \quad (\text{A.14})$$

The (dimensionless) ‘depth’ increment  $\Delta y$  is constant in the mapped computation domain whereas the corresponding affine-equivalent depth increment  $\Delta z$  depends on the variables  $r$  and  $\theta$  in the physical domain. We denote by  $\tilde{M}_{i,j} = (\theta_i, y_j)$  a node of the grid of the mapped computation domain. We assume for  $q \in \{1, \dots, Q\}$   $y_{m_q} = S_q$  for some  $1 < m_q < N$ . The nodes  $\tilde{M}_{i,j}$ ,  $0 \leq i \leq M$ , for  $j = 0$ ,  $j = m_q$ ,  $1 \leq q \leq Q$ , and  $j = N$  correspond, respectively, to the mapped ocean surface  $\{y = 0\}$ , to the mapped sedimental interfaces  $\{y = S_q\}$ ,  $1 \leq q \leq Q$ , (cf. Fig. A.2) and to the mapped rigid bottom  $\{y = 1\}$ . We let  $\tilde{K}_{i,j} = ]\theta_{i-1}, \theta_i[ \times ]y_{j-1}, y_j[$ ,  $1 \leq i \leq M$ ,  $1 \leq j \leq N$ . The geometry of  $\tilde{K}_{i,j}$  of each mesh in the mapped computation domain is rectangular. For  $r_0 \leq r \leq R$ , we denote by  $K_{i,j}^{(r)}$ ,  $1 \leq i \leq M$ ,  $1 \leq j \leq N$ , the corresponding mesh in the physical waveguide, defined by  $K_{i,j}^{(r)} = \{(\theta, z) / 0 < \theta < 2\pi, (j-1)\Delta z(r, \theta) < z < j\Delta z(r, \theta)\}$ . For  $r_0 \leq r \leq R$ , the geometry of  $K_{i,j}^{(r)}$ ,  $1 \leq i \leq M$ ,  $1 \leq j \leq N$ , being dependent of the varying geometry of the physical waveguide (cf. Fig. A.3) have curved boundaries.

It is to be noted that the different interfaces  $\Sigma_q$ ,  $1 \leq q \leq Q$ , present in the physical domain consist of edges of elements  $K_{i,j}^{(r)}$  provided the sedimental interfaces  $\{z = z_q(r, \theta)\}$ ,  $1 \leq q \leq Q$ , are homothetical, i.e.,  $z_q(r, \theta) = S_q s(r, \theta)$  (cf. Fig. A.4).

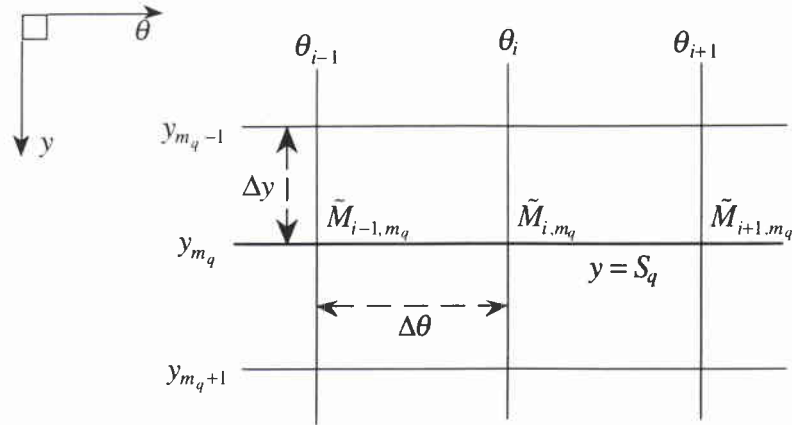


**Figure A.2** Treatment of the mapped sedimental interfaces  $\{y = S_q\}$ ,  $1 \leq q \leq Q$ . The discrete points  $\tilde{M}_{i,m_q}$ ,  $0 \leq i \leq M$ , are located on the interface.

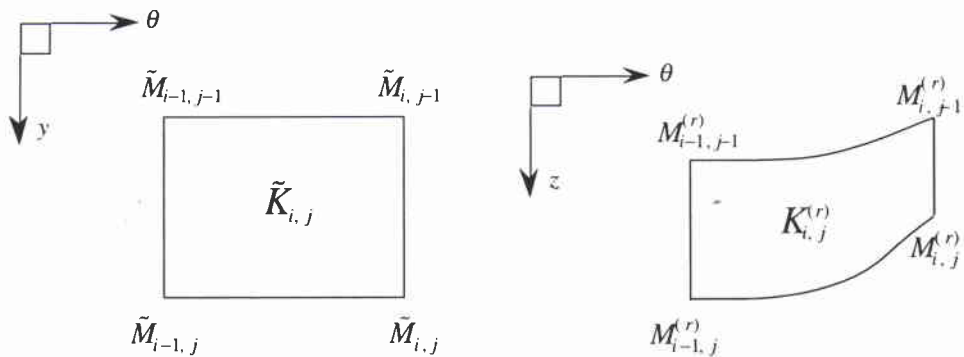


**Figure A.3** Rectangular mesh  $\tilde{K}_{i,j}$  of the triangulation defined on the mapped computation domain (on the left) and curved mesh  $K_{i,j}^{(r)}$  of the corresponding affine-equivalent triangulation (for  $r_0 \leq r \leq R$ ) of the physical domain (on the right).

SACLANTCEN SM-342

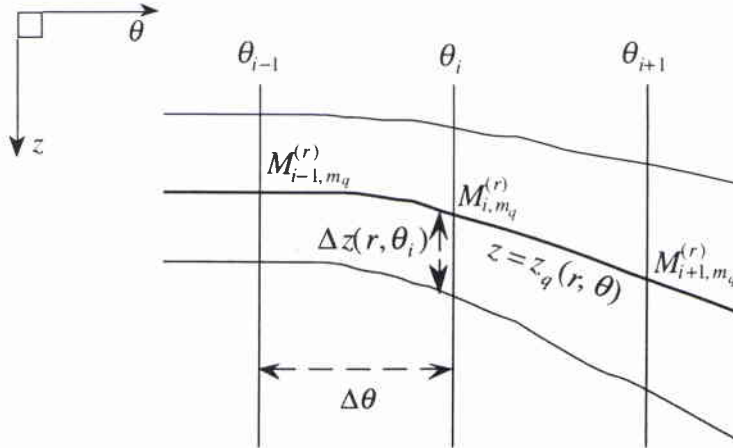


**Figure A.4** Treatment of the homothetical physical sedimental interfaces  $\{z = S_q s(r, \theta)\}$ ,  $1 \leq q \leq Q$ . For  $r_0 \leq r \leq R$  the nodes  $M_{i, m_q}^{(r)}$ ,  $0 \leq i \leq M$ , which are affine-equivalent of  $\bar{M}_{i, m_q}$ ,  $0 \leq i \leq M$ , are located on the interface.

We have  $\bar{\Omega} = \bigcup_{i=1}^I \bar{K}_k$  and  $\bar{K}_k \cap \bar{K}_{k'} = \emptyset$ ,  $1 \leq k < k' \leq I$ , where  $I = M \times N$  and where we have used the notations  $\bar{K}_{i, j}$  or  $\bar{K}_k$  if  $k = i + M(j-1)$  for  $1 \leq i \leq M$  and  $1 \leq j \leq N$ . We denote by  $\mathbf{Q}_1$  the space of complex-valued polynomials of degree at most 1. We define the finite dimensional space of functions which are continuous on  $\bar{\Omega}$ , piecewise  $\mathbf{Q}_1$ -polynomial relative to each mesh  $\bar{K}_k \subset \bar{\Omega}$ ,  $1 \leq k \leq I$ , and satisfy the homogeneous Dirichlet condition at  $y=0$ , i.e.

$$V_h = \left\{ \chi / \chi \in C^0(\bar{\Omega}) \text{ complex-valued, } \forall k \in \{1, \dots, I\} \chi|_{\bar{K}_k} \in \mathbf{Q}_1, \chi|_{\{y=0\}} = 0 \right\}$$

which is a subspace of  $V$  of dimension  $I = M \times N$ . Given  $\Delta r > 0$ , such that  $R = N_r \Delta r + r_0$ , we let  $r_n = n \Delta r + r_0$ ,  $0 \leq n \leq N_r$ , and  $r_{n+1/2} = r_n + \Delta r/2$ ,  $0 \leq n \leq N_r - 1$ . We consider the following finite element (in depth and azimuth) and Crank-Nicolson (in range) discrete scheme : Find  $\tilde{w}_h^n \in V_h$ ,  $0 \leq n \leq N_r$ , such that

$$(\partial_r \tilde{w}_h^{n+1/2}, \varphi_h)_{\rho, h} + i \alpha_h(r_{n+1/2}; \tilde{w}_h^{n+1/2}, \varphi_h) = 0, \quad \forall \varphi_h \in V_h \quad (\text{A.15})$$

$$\tilde{w}_h^0 = w^0$$

where we have used the notation  $\partial_r \tilde{w}_h^{n+1/2} = (\tilde{w}_h^{n+1} - \tilde{w}_h^n) / \Delta r$  and  $\tilde{w}_h^{n+1/2} = (\tilde{w}_h^{n+1} + \tilde{w}_h^n) / 2$ . The sesquilinear forms  $(\cdot, \cdot)_{\rho, h}$  and  $\alpha_h(r; \cdot, \cdot)$  correspond, respectively, to  $(\cdot, \cdot)_\rho$  and  $\alpha(r; \cdot, \cdot)$  where the integrals are approximated using the following quadrature formula

$$\int_{\bar{K}_{i, j}} \varphi d\Omega \approx \frac{\Delta \theta \Delta y}{4} (\varphi(\bar{M}_{i-1, j-1}) + \varphi(\bar{M}_{i-1, j}) + \varphi(\bar{M}_{i, j-1}) + \varphi(\bar{M}_{i, j})) \quad (\text{A.16})$$

where the nodes of the quadrature scheme are simply the four vertices  $\bar{M}_{i,j}$ ,  $\bar{M}_{i-1,j}$ ,  $\bar{M}_{i,j-1}$ ,  $\bar{M}_{i-1,j-1}$  of the rectangular mesh  $\bar{K}_{i,j}$ . Selecting  $\varphi_h = (\tilde{w}_h^{n+1} + \tilde{w}_h^n)/2$  in Eq. (A.15), we may show that

$$\|\tilde{w}_h^{n+1}\|_{\rho,h} \leq \|\tilde{w}_h^n\|_{\rho,h}, \quad 0 \leq n \leq N_r - 1 \quad (\text{A.17})$$

which implies that the fully discrete scheme, Eq. (A.15) (finite element in depth and azimuth / Crank-Nicolson in range) is unconditionnally stable in the discrete  $\|\cdot\|_{\rho,h}$ -norm. Eq. (A.17) holds as an equality, *i.e.*, the scheme is  $\|\cdot\|_{\rho,h}$ -conservative, if the attenuation term is null. Our fully discrete model still preserves the energy-conservation characteristic of the ‘continuous’ model (cf. Eq. (A.13)). Using a finite difference discretization technique would not lead to the stability condition of Eq. (A.17) and hence the corresponding discrete model would not be energy-conserving anymore.

A basis of  $V_h$  with elements of small support is constructed considering functions  $\varphi_k$ ,  $1 \leq k \leq I$ , defined by :  $\varphi_k(\bar{M}_{k'}) = 0$  if  $k \neq k'$  and  $\varphi_k(\bar{M}_k) = 1$ . For each  $n$ ,  $0 \leq n \leq N_r - 1$ , Eq. (A.15) represents a linear system of equation of size  $I \times I$  for the coefficients  $\tilde{w}_k^n$ ,  $1 \leq k \leq I$ , of  $\tilde{w}_h^n$  with respect to the previous basis, *i.e.*,  $\tilde{w}_h^n = \sum_{k=1}^I \tilde{w}_k^n \varphi_k$ , which writes in the following matrix form

$$\left( I + i \frac{\Delta r}{2} \mathbf{A}^{n+1/2} \right) \bar{W}^{n+1} = \left( I - i \frac{\Delta r}{2} \mathbf{A}^{n+1/2} \right) \bar{W}^n \quad (\text{A.18})$$

where  $\bar{W}^n = (\tilde{w}_1^n, \dots, \tilde{w}_I^n)^T$ ,  $0 \leq n \leq N_r$ , with  $k = i + M(j-1)$ , are vectors of size  $I = M \times N$ , and  $\mathbf{A}^{n+1/2}$ ,  $0 \leq n \leq N_r$ , are matrices of size  $I \times I$  defined by

$$(\mathbf{A}^{n+1/2})_{k',k} = \alpha_h(r_{n+1/2}; \varphi_k, \varphi_{k'}) / (\varphi_k, \varphi_{k'})_{\rho,h}$$

and where  $\bar{W}^0 = W^0$ . The matrix present in left-hand side of Eq. (A.18) is large, sparse and has a block-tridiagonal structure, each block of order  $M$  being almost tridiagonal (presence of terms in the upper right and lower left corners to account for the periodicity condition in the azimuthal direction). The  $N \times 2D$  discrete model writes in the following matrix form

$$\left( I + i \frac{\Delta r}{2} \mathbf{A}_{N \times 2D}^{n+1/2} \right) \bar{W}_{N \times 2D}^n = \left( I - i \frac{\Delta r}{2} \mathbf{A}_{N \times 2D}^{n+1/2} \right) \bar{W}_{N \times 2D}^n \quad (\text{A.19})$$

where  $\bar{W}_{N \times 2D}^n = (\tilde{w}_1^n, \dots, \tilde{w}_I^n)^T$ ,  $0 \leq n \leq N_r$ , with  $k = j + N(i-1)$ , are vectors of size  $I = M \times N$ , and the matrices  $\mathbf{A}_{N \times 2D}^{n+1/2}$ ,  $0 \leq n \leq N_r$ , are defined by

$$(\mathbf{A}_{N \times 2D}^{n+1/2})_{k',k} = \alpha_{N \times 2D,h}(r_{n+1/2}; \varphi_k, \varphi_{k'}) / (\varphi_k, \varphi_{k'})_{\rho,h}$$

The sesquilinear forms  $\alpha_{N \times 2D,h}(r; \dots)$  correspond to  $\alpha_{N \times 2D}(r; \dots)$  using the quadrature formula of Eq. (A.16). The matrix present in left-hand side of Eq. (A.19) has now a

SACLANTCEN SM-342

block-diagonal structure, each block of order  $N$  being tridiagonal. For each  $n$ ,  $0 \leq n \leq N_r - 1$ , Eq. (A.19) can be solved using a fast and robust Gaussian elimination method.

Solving Eq. (A.18) using Gaussian elimination requires an excessive amount of storage (storage must be allocated for the bandwidth equal to  $2M+3$  in each row of the matrix) which limits the number of mesh points that can be used. Thus, in order to effectively utilize the sparseness of the matrix present in the left hand side of Eq. (A.18), it is important to develop an iterative technique. However Eq. (A.18) is difficult to invert by standard iterative methods [18].

We choose to solve for each  $n$ ,  $0 \leq n \leq N_r - 1$ , the linear system of Eq. (A.18) using a non-stationary iterative algorithm equivalent to the preconditioned conjugate gradient iteration method for normal equations [19]. The amount of storage required now depends linearly on the number of grid points. In addition, few vectors need to be stored. Hence the storage is much less than that required by any version of Gaussian elimination. The efficiency of the solver highly depends of the preconditioning procedure. We choose to precondition Eq. (A.18) using the matrix derived from the  $N \times 2D$  discrete model given in the left hand side of Eq. (A.19). Practical numerical results demonstrate that the acceleration due to the preconditioning is so great compared to the non-preconditioned iteration method that the additional operations inherent to the preconditioning procedure are negligible.

*Document Data Sheet***NATO UNCLASSIFIED**

<i>Security Classification</i> UNCLASSIFIED		<i>Project No.</i> 042-4
<i>Document Serial No.</i> SM-342	<i>Date of Issue</i> March 1998	<i>Total Pages</i> 71 pp.
<i>Author(s)</i> Sturm, F.B., Fawcett, J.A.		
<i>Title</i> Numerical simulation of the effects of bathymetry on underwater sound propagation using three-dimensional parabolic models.		
<i>Abstract</i>  Two different three-dimensional parabolic equation (PE) methods are presented. These methods are used to show the importance of three-dimensional effects for some examples and different frequencies and the results from the two methods are compared with each other in order to show that the two very different PE approaches give similar results. The methods of this report provide an accurate and relatively efficient means of computing three-dimensional propagation loss which will form the basis of future improvements.		
<i>Keywords</i> Parabolic equation – propagation		
<i>Issuing Organization</i> North Atlantic Treaty Organization SACLANT Undersea Research Centre Viale San Bartolomeo 400, 19138 La Spezia, Italy  [From N. America: SACLANTCEN (New York) APO AE 09613]		Tel: +39 0187 527 361 Fax: +39 0187 524 600  E-mail: library@saclantc.nato.int

**NATO UNCLASSIFIED**

**Initial Distribution for Unclassified SM-342**

***Scientific Committee of National Representatives***

SCNR Belgium	1
SCNR Canada	1
SCNR Denmark	1
SCNR Germany	1
SCNR Greece	1
SCNR Italy	1
SCNR Netherlands	1
SCNR Norway	1
SCNR Portugal	1
SCNR Spain	1
SCNR Turkey	1
SCNR UK	1
SCNR USA	2
French Delegate	1
SECGEN Rep. SCNR	1
NAMILCOM Rep. SCNR	1

***National Liaison Officers***

NLO Canada	1
NLO Denmark	1
NLO Germany	1
NLO Italy	1
NLO Netherlands	1
NLO Spain	1
NLO UK	3
NLO USA	4
Sub-total	30
SACLANTCEN library	21
<b>Total</b>	<b>51</b>